

Carnegie Mellon University

CARNEGIE INSTITUTE OF TECHNOLOGY

THESIS

SUBMITTED IN PARTIAL FULFILLMENT OF THE REQUIREMENTS

FOR THE DEGREE OF **Doctor of Philosophy**

TITLE

Thermal transport in organic-inorganic heterojunctions: Experimental measurements and computational predictions

Presented by **SHUBHADITYA MAJUMDAR**

ACCEPTED BY THE DEPARTMENT OF

MECHANICAL ENGINEERING

ADVISOR, MAJOR PROFESSOR

DATE

DEPRATMENT HEAD

DATE

APPROVED BY THE COLLEGE COUNCIL

DEAN

DATE

**Thermal transport in organic-inorganic heterojunctions:
Experimental measurements and computational predictions**

Submitted in partial fulfillment of the requirements for

the degree of

Doctor of Philosophy

in

Mechanical Engineering

Shubhaditya Majumdar

B.Tech., Mechanical Engineering, Indian Institute of Technology, Kharagpur,
India

M.S., Mechanical Engineering, Carnegie Mellon University, USA

Carnegie Mellon University
Pittsburgh, PA

May, 2016

Copyright © 2016 Shubhaditya Majumdar

Abstract

The objective of this work is to investigate thermal transport physics in organic-inorganic heterojunctions employing experimental and computational techniques. A self-assembled monolayer (SAM) junction, a two-dimensional array of ordered molecules sandwiched between two metal leads, is used as the primary investigative system. The SAM structure provides a convenient platform to isolate the junction transport properties that are otherwise difficult to characterize when using three-dimensional organic-inorganic hybrid materials with embedded interfaces.

A combination of deposition and lift-off techniques are used to fabricate the SAM junctions and frequency domain thermoreflectance (FDTR) is employed to measure the junction thermal conductance. Molecular dynamics (MD) simulations are used to further probe the vibrational properties and intermolecular cooperative behavior of the junction components and identify their effects on the thermal transport trends. A statistical rough surface contact model is also developed to estimate the percentage contact area between two rough surfaces interacting through covalent bonds. The quality of contact at interfaces is crucial for the accurate interpretation of experimentally measured transport properties of such molecular junctions.

I present the first-ever measurements of the thermal conductance of SAM junctions formed between metal leads with systematically mismatched phonon spectra. The experimental observation that junction thermal conductance (per molecule) decreases as the mismatch between the lead vibrational spectra increases, paired with results from MD simulations, suggest that phonons scatter elastically at the metal-SAM interfaces. Furthermore, a known discrepancy between measurements and MD predictions of SAM thermal conductance is resolved by using

the contact mechanics model to predict the extent of areal contact in the metal-SAM-metal experimental junctions.

Further investigations of the nature of scattering at the metal-SAM interfaces using MD simulations reveal limitations in this computational scheme to study mismatched SAM junctions. These are related to the classical nature of the MD simulations that allow vibrational coupling to occur at the metal-SAM-metal junction that is not present in the experimental system. I present methods to circumvent this limitation and validate the predicted thermal transport trends with analytical models.

The statistical contact model is derived to predict areal contact between two rough surfaces interacting through covalent bonds and is validated using thermal conductance measurements of SAM junctions. The model is also capable of handling the contact between a two-dimensional surface and substrate, which is relevant for studying the contact of supported two-dimensional materials. I also present a methodology to extend this model to handle layered substrates (i.e. a substrate with layers of distinct atomic species), which are present in nanostructured devices.

The effect of the cooperative behavior between molecules on thermal transport across molecular junctions is investigated using a binary SAM system. This system enables one to tailor the local molecular environment within the junction. A non-linear change in thermal conductance as a function of molecular composition of the SAM is observed indicating that the molecules are not independent heat channels. The thermal transport through the molecules that are weakly coupled to the leads is enhanced when strongly coupled molecules are placed in their vicinity. The per molecule thermal conductance increases with increasing average separation

between the molecules, suggesting the challenge in predicting single molecule properties from parallel structures and vice-versa.

The findings in this thesis can potentially be used to tailor transport properties of hybrid materials for devices such as thermoelectrics, light-emitting diodes, photovoltaics and electronic devices. Thermal management in such devices, which is crucial especially when they are extremely thin, can also be improved using design principles that enhance thermal transport across the organic-inorganic heterojunctions.

Acknowledgements

I would like to first thank my parents for molding me into the person I am today. They always motivated me to try and excel in any interest I had. They are my biggest inspirations and I will always look to them for guidance for the rest of my life. Moving between various cities during my childhood, I can imagine it must have been hard to adjust to all the new places especially with a young, adolescent (and maybe slightly spoilt) boy. I will always be grateful for all the sacrifices you made for me in your life.

Thank you Profs. Jonathan Malen and Alan McGaughey for accepting me into the co-advised graduate student role (which was still new at the time). You guided me professionally and at a personal level and helped me excel as a problem solver, researcher and person. It was the best experience I could have had and I cannot imagine better mentors to complete my graduate studies with. I would like to thank the members of the Malen and McGaughey labs: Keith, Justin, Wee-Liat, Scott, Zoey, Jason, Lili, Ankit, Kevin, Simon, Ivy, Francisco, and the rest of the current members. We had great discussions about work and pretty much everything else, having a lot of fun in general. A special shout out to Pengfei, Baoan, and Jaowie – my first year office mates and friends throughout the Ph.D. journey. I would also like to thank my thesis committee members – Profs. Pramod Reddy and Michael Bockstaller for the guidance that helped me in my research and successfully collaborate with your groups.

Outside the lab, I was part of an amazing MechE social group which evolved over the last five years but whose memories I will always cherish: Salem, Ramon, Mari, Daniel, Hassan, Rachel, Adam, Lauren, Kyle, Chris, Sid, Pratiti, Mike and so many others. A bunch of you were on the two-time championship winning MechE softball team (Lumber Co.); my summer evenings will feel empty for quite some time after graduation without our games.

The other Pittsburgh family I will sorely miss is the IGSA music team (The Peace Band): Ashiqur, Siddharth Singh, Dipan, Purvasha, Neel, Arnab, Anvesh, Sayali, Siddharth Raghu, Prem, Srikant and everyone else (the list is really too long). I will always miss the jam sessions, late night practices, and the awesome hangouts we had. And I'd like to extend this to everyone I've met through IGSA, many of whom have become a part of my regular social activities.

I would like to specially thank Subhro (my housemate in Pittsburgh), Arka, and Pratiti for putting up with my shenanigans, giving me food and being amazing friends and support. I wish to thank Namrata for such a special year that I hope will continue into many more.

Any acknowledgment would be incomplete without mentioning my best friends from undergrad: Girish, Peeyush, Mikesh, Rishav, Abhilash, Abhishek, Ram, Chirag, Achilles, and Anutosh. Our friendship is for life no matter how geographically separated we get. What amazing times we had in KGP and I hope to have many more of them in the upcoming years!

I would like to acknowledge the Bushnell family for supporting my Ph.D. with the Bushnell fellowship in 2016, NSF, DOE, and AFRSO for grants that supported a bulk of my work, and the Carnegie Mellon Graduate Student Assembly for conference travel awards.

Table of Contents

Abstract	i
Acknowledgements	iv
List of figures	viii
List of tables	xvi
1. Chapter 1	1
1.1. Introduction	1
1.2. Material systems	2
1.2.1. Self-assembled monolayers	2
1.3. Contact and adhesion between two rough surfaces	5
1.4. Objective	7
1.4.1. Methods	7
1.4.1.1. Experimental	7
1.4.1.2. Computational	9
1.5. Overview and Scope	10
2. Chapter 2: Experimental investigation of thermal conductance in organic junctions with metal leads	14
2.1. Introduction	14
2.2. Sample preparation and characterization	16
2.2.1. Templated metal synthesis	16
2.2.2. Transfer printing procedure	18
2.2.3. XPS measurement	19
2.2.4. Ellipsometry measurement	21
2.2.5. Debye temperatures of leads	22
2.3. Frequency domain thermorefectance	23
2.3.1. Experimental setup	23
2.3.2. Uncertainty analysis	24
2.4. Molecular footprint	25
2.5. FDTR results	26
2.6. Contact area correction	30
3. Chapter 3: Computational techniques to probe thermal transport scattering mechanisms in organic junctions with metal leads	34
3.1. Molecular dynamics simulation	34
3.1.1. Structure relaxation and non-equilibrium simulations	34
3.1.2. Calculating the junction and interface thermal conductances	36
3.1.3. Cross-sectional area and length convergence	38
3.2. Vibrational mismatch effects using MD simulations	40
3.3. Effects of the classical nature of MD	43
3.4. Modified diffuse mismatch model	44
4. Chapter 4: Morse potential-based model for contacting composite rough surfaces – Application to self-assembled monolayer junctions	47
4.1. Introduction	47
4.2. Theory	48

4.2.1.	Derivation of surface pressure using the Morse potential	48
4.2.2.	Single asperity deformation.....	56
4.2.3.	Morse potential-based adhesion model based on asperity deformation	59
4.2.4.	Extension to two-body contact problem.....	61
4.2.5.	Composite asperity model for modeling layered structures	63
4.2.6.	Characterization of an experimental surface	64
4.3.	Results	66
4.3.1.	Parameters of AFM measurements	66
4.3.2.	Comparison of Morse and LJ adhesive pressures	67
4.3.3.	Application to thin films: Self-assembled monolayer on gold.....	68
5.	Chapter 5: Cooperative behavior between molecules and its effect on junction thermal conductance.....	76
5.1.	Introduction	76
5.2.	Sample preparation and FDTR setup	78
5.3.	FDTR results.....	81
5.4.	Contact area correction	84
5.5.	Simulation results	85
6.	Chapter 6: Other projects	93
6.1.	Thermal transport enhancement of nanocomposites using polymer brushes	93
6.2.	Molecular dynamics simulation of nanocrystal arrays for thermal transport investigations.....	95
6.3.	Broadband frequency domain thermoflectance for phonon spectroscopy	97
7.	Chapter 7: Summary and outlook.....	100
7.1.	Experimental measurement of self-assembled monolayer (SAM) junction thermal conductance.....	100
7.2.	Computational modeling thermal transport in SAM junctions.....	101
7.3.	Rough surface contact model for covalent interfaces	101
7.4.	Collective behavior of molecules affecting thermal transport in SAMs	102
7.5.	Future outlook	103
7.5.1.	Energy transport in electrically conducting SAM junctions	103
7.5.2.	Temperature dependent thermal measurements of SAM junctions	104
7.5.3.	Nanocomposites with high-k nanoparticles and polymer brushes	104
7.5.4.	Specialized methyl-gold interatomic potential from first principles.....	105
8.	Appendix	106
8.1.	Generalized expressions to calculate r_e and A_2	106
8.2.	Expression for critical interference and plasticity index	108
8.3.	Plastic deformation regimes for composite asperities	109
8.4.	Adhesive pressure and energy between a surface and a substrate for an LJ potential.....	109
8.5.	Contact stress and contact area	110
8.6.	Sensitivity analysis of the Morse contact model	110
8.7.	Uncertainty analysis of area-corrected thermal conductance.....	112
9.	Bibliography	113

List of figures

Figure 1.1. Self-assembled monolayer grown on an inorganic substrate (left) creating a single organic-inorganic interface. When a second inorganic layer is placed on top of the SAM, a junction is created comprising two interfaces.2

Figure 2.1. (a) Schematic diagram of the transfer printing process to create a SAM junction. A 95 ± 5 nm Au layer is transfer printed onto a SAM grown on a $475\text{-}530 \pm 20\text{-}30$ nm (see Table 2.4) templated metal substrate. (b) Straight chain alkane-based molecules used to create the SAMs in this study (1,10-decanedithiol, 1-dodecanethiol, and 1-tetradecanethiol).15

Figure 2.2. (a) Si templates attached to a gold substrate (sputtered onto an Si wafer) using EPOTEK 377 epoxy, after curing. (b) Si template being stripped off using a razor blade.....17

Figure 2.3. Dilute solutions of SAMs ($\sim 0.1\text{-}1$ mM) in ethanol having template metal leads immersed in them.17

Figure 2.4. XPS measurement showing binding energy spectra O 1s electrons for samples having 1-dodecanethiol grown on Au, Ag, Pt and Pd leads. No peaks (near 532 eV) can be seen indicating absence of oxide layer. Plot for O 1s on Pd is not shown as the Pd $3p_{3/2}$ peak also lies within this energy range.20

Figure 2.5. (a) XPS measurement showing binding energy peaks for S 2p electrons indicating formation of the SAM. (b) XPS measurement showing binding energy peaks for C 1s electrons.

Measurements for samples with SAM have larger peaks indicating large presence of C atoms (due to presence of SAM layer).21

Figure 2.6. (a) FDTR phase responses for junctions with 1,10-decanedithiol, 1-dodecanedithiol, and no molecules are clearly distinguishable. Solid lines represent the best-fit solutions of the heat diffusion equation for a semi-infinite layered system heated by a Gaussian-shaped periodic heat flux at the surface. (b) Variation of junction thermal conductance G with the Debye temperature of the templated metal substrate on which the SAM is grown. The raw experimental data (left panel, unfilled data points) are scaled by the molecular footprint (right panel, filled data points) to isolate the effect of the leads vibrational spectra on G . Also plotted is the MD prediction of G for a Au-(1,10-decanedithiol)-Au junction (unfilled star) and percentage area corrected experimental thermal conductance (filled black circle), which has been displaced slightly to the left for clarity. All experiments were performed at an ambient temperature of 296 K.28

Figure 2.7. (a) AFM image of a templated Au lead (RMS roughness 4 ± 1 Å). (b) Schematic diagram of two rough surfaces represented as spherical asperities (475 nm Au + SAM) in contact with a flat, undeformable surface (95 nm Au). (c) A single asperity is a layered, composite structure consisting of an outer shell of the SAM molecules [S (red) and C (black) atoms] enclosing an inner Au core. Interactions between all atoms and the upper Au surface are considered when calculating the percentage contact area.31

Figure 3.1. Relaxed structure of 1,10-decanedithiol on Au lead at a temperature of 300 K from an *NVT* ensemble using MD simulation.34

Figure 3.2. Relaxed structure of 1,10-decanedithiol junction comprising two Au leads at 300 K from an <i>NVT</i> ensemble using MD.....	35
Figure 3.3. Temperature profile in the MD simulation cell.	38
Figure 3.4. (a) Convergence analysis with cross-sectional area of Au leads. (b) Convergence analysis with length of Au leads.	39
Figure 3.5. Effect of system mean temperature on the junction thermal conductance.	40
Figure 3.6. (a) DOS of the metal leads with atomic masses m_{Au} (red) and $0.5m_{\text{Au}}$ (blue), and 1,10-decanedithiol having carbon and sulphur atoms with atomic masses (m_{C} , m_{S}) (green), ($400m_{\text{C}}$, $400m_{\text{S}}$) (purple) and ($1000m_{\text{C}}$, $1000m_{\text{S}}$) (orange). (b) MD-predicted variation of the thermal conductance of the individual interfaces (blue square and red triangles) and the entire junction (green circles) with the Debye temperature ratio of the metal leads. (c) Variation of junction thermal conductance, normalized by the value of the matched lead case, with the Debye temperature ratio of the metal leads. The MD predictions (orange triangles, purple squares, and green circles) are compared to the experimental results (blue filled circle) and DMM calculations (dashed line).	41
Figure 4.1. (a) Comparison of Morse and LJ potentials for the same energy well depth and equilibrium separation for a thiol-gold interaction. ⁹⁸ (b) Schematic diagrams representing interactions between two point particles, one point particle and a flat, semi-infinite substrate, and two flat, semi-infinite substrates.	49

Figure 4.2. (a) Schematic diagram of the structure for single-point energy calculations between a two-dimensional surface of atom type 1 (yellow) placed at different heights above a substrate of atom type 2 (pink). (b) Interaction energy, non-dimensionalized by $\Delta\gamma_{\text{LJ}}$, using both Morse (red squares) and LJ (blue circles) potentials for a thiol-gold interaction (parameters in Table 4.1) plotted as a function of separation distance D between the surface and substrate. The magnitude of the interaction energy at its minimum value (where $D = r_e$) is equal to $\Delta\gamma$55

Figure 4.3. (a) Schematic diagram of a hemispherical asperity in contact with a flat surface and undergoing deformation. The flat surface is assumed to be rigid. (b) Schematic diagram of a hemispherical asperity at a height D_a above a flat surface.57

Figure 4.4. Conversion of two real surfaces to a statistical representation. The real surfaces are mapped to a flat surface in contact with a rough surface comprised of hemispherical asperities of radii R , which follow a statistical distribution [Eq. (25)], allowing for the height of each asperity to vary about the mean line.61

Figure 4.5. (a) Comparison of the non-dimensional adhesive pressure calculated using the Morse potential-based (solid blue line) and LJ potential-based (solid red line, similar to the KE model⁸¹) contact models, and the non-dimensional contact stress, plotted as a function of non-dimensional mean separation (d^*) between a rough thiol surface and a smooth gold substrate. Inset: Percentage contact area A^* plotted as a function of d^* . (b) Hemispherical asperity composed of a thin film (1,10-decanedithiol SAM) on a gold substrate. There is an outer layer of thiols, followed by a shell of carbon atoms (thickness of $t_2 - t_1$) and an inner region of gold atoms (radius of $R - t_3$). There is an additional single thiol layer at the inner gold surface. (c) Adhesive

pressure versus mean separation of asperities for different material components of the asperity – thiol (blue line), carbon (red line), and gold layers (green line) with the planar gold substrate. The contact reaction pressure (dashed line) for the asperity is also plotted and is not affected by the structure of the asperity. 70

Figure 5.1. (a) Schematic representations of a full dithiol, a full monothiol and a binary SAM (50% di and 50% monothiol) grown on Au leads. The terminal groups have been magnified to emphasize their type. (b) Advancing contact angle measurements of $C_{10}S_2:C_6S$, $C_{10}S_2:C_{11}S$, and $C_{10}S_2:C_{14}S$ mixed SAMs plotted as a function of R_{soln} . The lines represent Eq. 1 fitted to the three mixed SAM compositions. (c) FDTR phase lag data as a function of the modulation frequency are fit with an analytical solution to the heat diffusion equation for three $C_{10}S_2:C_{11}S$ SAM configurations. 80

Figure 5.2. (Upper panel) $\chi_{1s,soln}$ for $C_{10}S_2:C_6S$, $C_{10}S_2:C_{11}S$, and $C_{10}S_2:C_{14}S$ plotted as a function of $\chi_{1s,SAM}$. The dashed line denotes the case when there is no difference between the concentration of monothiols in the solution and the SAM. (Lower panel) G for $C_{10}S_2:C_6S$, $C_{10}S_2:C_{11}S$, and $C_{10}S_2:C_{14}S$ plotted as a function of $\chi_{1s,SAM}$. All experiments were performed at an ambient room temperature of 296 K. 82

Figure 5.3. Comparison between FDTR measurements, MD predictions, and percentage contact area-corrected MD predictions of the junction thermal conductance of the $C_{10}S_2:C_{11}S$ system as a function of $\chi_{1s,SAM}$ 85

Figure 5.4. Variation of G for the $C_{10}S_2:C_{11}S$ mixed SAM, the partially packed $C_{10}S_2$ SAM, and the partially packed $C_{11}S$ SAM plotted as a function of the fraction of $C_{11}S$ in the mixed system or voids in the partial SAM system. The dashed lines represent the variation of G if the molecules behaved as parallel conductances. Comparison between the MD simulation results of the $C_{10}S_2:C_{11}S$ mixed SAM configuration and the case where the partially packed $C_{10}S_2$ SAM is added to the parallel conductance assumption for the $C_{11}S$ SAM (yellow dashed line in the main plot) to predict an upper limit to the effective thermal conductance for the mixed SAM case based on parallel conductances between the $C_{10}S_2$ and $C_{11}S$ molecules. 86

Figure 5.5. (a) Root mean-squared (RMS) displacement of the terminal methyl group plotted as a function of the fraction of $\chi_{1s,SAM}$ in a $C_{10}S_2:C_{11}S$ SAM or $\chi_{voids-partial}$ in a $C_{11}S$ partial SAM. (b) Variation of the average terminal methyl-Au separation (plotted with respect to the left vertical axis) and G from MD simulations for the $C_{10}S_2:C_{11}S$ SAM (plotted with respect to the right vertical axis) as a function of $N_{atoms,1s}/N_{atoms,2s}$, for $\chi_{1s,SAM} = 0.5$. The dashed horizontal line represents the cutoff (9 Å) for the LJ potential describing the methyl-Au bond. 90

Figure 6.1. Thermal conductivity of PMMA-based composite materials. Symbols represent SiO_2 -SAN24/PMMA (filled red squares) and SiO_2 -SAN14/PMMA (open red squares), SiO_2 -MMA28/PMMA (blue triangle) and SiO_2 -MMA200/PMMA (open blue diamond), respectively. Lines represent effective medium predictions based on the Nan effective medium model assuming infinite interface thermal conductance ($G = \infty$, black dashed line) and $G = 420 \text{ MW m}^{-2} \text{ K}^{-1}$ (black solid line) as well as PMMA (blue dashed line) and PSAN (red dashed line.). [C. Mahoney *et al. Polymer* (2016)] 94

Figure 6.2. EMA investigation for diameter series. (a) Interface thermal conductance as a function of nanoparticle diameter where $h_{SAM/gold}$ is the predicted SAM thermal conductance and $c = 0.76$ nm is obtained from the footprint scaling law. The red shaded region depicts the uncertainty in the $h_{SAM/gold}$. The value of $h_{SAM/gold}$ is plotted as a blue dotted line with its associated uncertainty (blue shaded area). Inset: interfacial thermal conductance shows no temperature dependence between 200 and 400 K, indicating a dominance of elastic scattering between the core and ligands. (b) MD diameter series is well-described by EMA-h accounting for interfacial thermal conductance between the core and ligand. The red shaded region marks the uncertainty range associated with the EMA-h model due to the uncertainties in its inputs. [W.-L. Ong *et al. J. Phys. Chem. C*, 118, 7288 (2014)].....96

Figure 6.3. k_{accum} for c-Si at $T = 311$ K as a function of L_p . The data is normalized to $k_{bulk, Si} = 143$ W/mK and compare favorably to results in literature, both experimental²¹³ and numerical.²⁰² [K.T. Regner *et al. Rev. Sci. Instrum.* 84, 064901 (2013)].....99

Figure 8.1. Variation of r_o/r_{NN} plotted as a function of ar_{NN} for specific values of r_o/r_{NN} from single-point energy calculations (open circles) and numerical fits (dashed lines)..... 107

Figure 8.2. Variation of $\Delta\gamma_M/\Delta\gamma_{LJ}$ plotted as a function of ar_{NN} for specific values of r_o/r_{NN} from single-point energy calculations (open circles) and numerical fits (dashed lines)..... 108

Figure 8.3. Sensitivity analysis showing variation of percentage contact area predicted using the Morse potential-based contact model with respect to relative change of the independent

parameters ξ , $d\xi/dx$, and $d^2\xi/dx^2$. The nominal values for all parameters are taken from Table 4.1.

..... 111

List of tables

Table 2.1. Refractive indices for all metal leads and SAM thicknesses. Measured using ellipsometry.....	22
Table 2.2. Debye temperatures of the metal leads.	22
Table 2.3. Parameters used in solution of heat diffusion equation for FDTR measurements. The SAM thermal conductance (G) is the only fitting parameter.	23
Table 2.4. Thermal conductivities of metal films.	24
Table 2.5. Molecular footprints of 1,10-decanedithiol on a metal leads.....	26
Table 4.1. Atomic interaction and surface topography parameters.....	49
Table 4.2. Coefficients in the expressions for pressure [Eq. (4.9)], energy per unit area [Eq. (4.10)], and work of adhesion [Eq. (4.11)] derived for the interaction between two substrates (ss), and a surface with a substrate ($surf-s$) described by a Morse potential.....	52
Table 4.3. Range of contact regimes.	58
Table 4.4. Coefficients in the expressions for contact [Eq. (4.21)] and non-contact [Eq. (4.23)] adhesive pressures derived for the interaction between two substrates (ss) and a surface with	

substrate (*surf-s*) described by a Morse potential. The coefficients B_2 and B_3 are listed in Table II.

.....61

Table 4.5. Parameters of RMS surface roughness (σ_h), radius of asperity (R), and areal asperity density (η) for all AFM measurements of a template Au surface.....67

Table 5.1. Comparison of junction thermal conductances predicted from MD simulations for three mixed SAM configurations using standard LJ interactions and 90% weaker LJ interactions.

.....89

1. Chapter 1

1.1. Introduction

Hybrid materials exploit intimate structured connections between organic and inorganic components to create unique energy and charge transport landscapes, showing promise for applications in electronics,¹⁻⁶ light-emitting diodes,^{7,8} solar cells,⁹⁻¹¹ and thermoelectrics.¹²⁻¹⁹ The major thrust for the research of such materials is to exploit their unique transport properties and manufacturability as an alternative to traditional semiconductor materials. For example, organic electronic devices can be integrated into wearable products and organic LEDs can be grown on a large surface such as a building wall and their brightness/wavelength can be tuned by adjusting the chemical compositions of the organic active layer.

The lifetime and efficiency of such micro- or nano-scale devices is, however, affected by their operating temperature so it is critical to know their thermal properties.^{20,21} For hybrid materials, thermal conductance at the internal organic-inorganic interfaces plays a key role.²²⁻²⁴ Interface thermal conductance (G) is defined by $q'' = G\Delta T$ where q'' is the heat flux incident on an interface and ΔT is resulting temperature difference across the interface. Detailed characterization of the thermal properties of the junctions, their tunability, and variations in their physical properties (e.g. percentage contact between components across an interface) with fabrication techniques need to be established for successful development of future technologies involving hybrid materials.

The major material system we focus on in this study, and the existing theory of characterizing the contact between two such material systems having rough surfaces are described below:

1.2. Material systems

1.2.1. Self-assembled monolayers

A self-assembled monolayer (SAMs) is two-dimensional array of molecules having a well-defined periodic arrangement, self-assembled or adsorbed onto an inorganic substrate through physical and/or chemical processes. The substrates can range from semiconductors like silicon²⁵ or gallium arsenide²⁶ to metals such as gold²⁷ and platinum.²⁸ A junction is formed when a second substrate is placed on top of the SAM, thus forming two organic-inorganic interfaces, as shown in Figure 1.1.

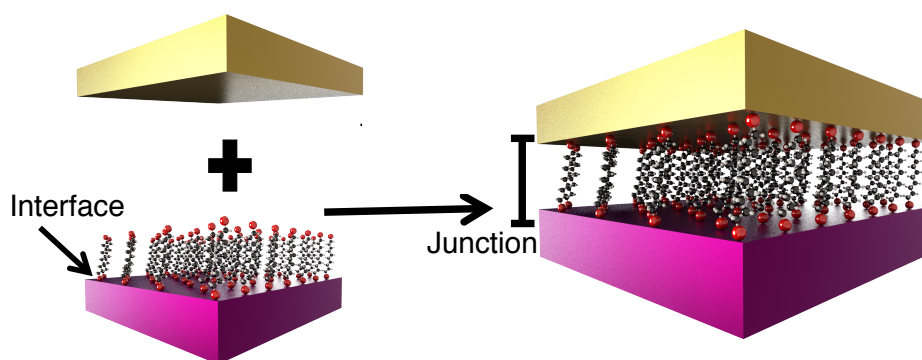


Figure 1.1. Self-assembled monolayer grown on an inorganic substrate (left) creating a single organic-inorganic interface. When a second inorganic layer is placed on top of the SAM, a junction is created comprising two interfaces.

The vast majority of initial research on SAMs focused on the growth of molecules having different end-groups that could bond to the substrate surface and also on the various kinds of substrates that could support the formation of SAMs. The earliest successful SAMs were formed using organo-sulphur compounds (molecules with terminal thiol groups) such as alkanethiols, dialkyl sulphides, and dialkyl disulphides on gold and silver substrates.^{27,29–33} The free end of the molecule had a variety of terminal groups such as amine, alcohol, or carboxylic acid. Ongoing research has helped expand the possible combinations of end-group and substrate to a much larger range.

This study will focus on alkanethiol SAMs grown on metal substrates, especially gold substrates. Historically, it has been found that Au forms good SAM structures. These structures have been extensively characterized in terms of molecule packing structure, tilt angle, wetting and defect behavior.^{27,30,32–35} We thus use the Au-thiol system as a reference and base all our findings and trends of thermal transport behavior on this system.

The most common method to synthesize SAMs onto metal surfaces is through adsorption from solution (another method is direct absorption from gas phase in ultra-high vacuum³⁵). A dilute solution of the SAM is prepared in either ethanol or toluene ($\sim 1 - 10$ mM) and the metal substrate is immersed in this solution for a period of 16 – 24 hours. The longer the immersion time, the more ordered the SAM structure. It has been shown that the evolution of a dense SAM structure on the metal substrate usually begins with a low-density phase (‘lying down’ phase for alkanedithiol SAMs), which then progresses into the final, high-density phase over time.^{36–38}

Electrical measurements of SAM junctions have shown promise for using them in electronic devices.^{2,5,6,39} The experiments involve a variety of techniques to measure electrical conductance, including, scanning tunneling microscopy,^{40,41} conducting probe atomic force microscopy,⁴² nano transfer-printing,⁴³ hanging mercury drop junction,⁴⁴ and eutectic GaIn contact method.⁴⁵

Despite these developments in understanding SAM structures and their electrical transport properties, their potential as a system to study thermal transport between chemically bonded organic and inorganic components have only recently been realized. For the alkane-based SAMs investigated in this study, vibrations dominate thermal transport across the junctions since electronic transport is only possible through weak off-resonant tunneling mechanisms.^{15,16,39,41,46,47} Early measurements suggested that SAM junction thermal conductance

is limited by the molecule-lead interfaces. Z. Wang *et al.*²² probed thermal transport through an alkanethiol SAM grown on Au. They found that the major thermal resistance was the Au-SAM interface (thermal conductance of 220 ± 100 MW/m²-K) and that thermal transport within the molecules was ballistic. R. Y. Wang *et al.*⁴⁸ were the first to investigate SAM junctions studying metal-SAM-semiconductor (Au-alkanedithiol-GaAs) systems and reported a junction thermal conductance of 28 ± 3 MW/m²-K that did not vary with molecular length (eight to ten CH₂), corroborating ballistic thermal transport within the molecules. Meier *et al.*⁴⁹ also reported a length-invariant Au-SAM interface thermal conductance for alkanethiol SAMs having more than ten carbon atoms, but found an increase in interface thermal conductance at shorter chain lengths.

The strength of the interfacial bonding between the molecule head group and the lead has also been found to affect thermal transport across SAM junctions. Using Au-SAM-SiO₂ junctions with alkane-based SAMs, Losego *et al.*⁵⁰ showed that higher interfacial bonding strength could increase the junction thermal conductance from 30 to 65 MW/m²-K. O'Brien *et al.*⁵¹ found that SAMs could be used to amplify the interface thermal conductance between a metal and a dielectric, by increasing the interfacial adhesion energy as well as augmenting the overlap region of the molecule and lead vibrational states.

Computational efforts to quantify thermal transport in organic-inorganic systems have led to similar conclusions. Segal *et al.*⁵² predicted that for junctions comprised of alkane chains with more than ten carbon atoms in contact with two leads, inelastic effects at the interfaces and within the molecules are insignificant. They found the thermal conductance of the junction to be independent of molecular length in this range at a temperature of 300 K, consistent with experimental measurements.^{48,49} Predictions from molecular dynamics (MD) simulations have

found interface thermal conductance to increase with increasing interfacial bond strength and increasing vibrational overlap between molecule and substrate.^{51,53–56} The predicted values of junction thermal conductance from MD simulations,^{53,54,56} however, are at least a factor of two higher than those measured in experiments.^{48,50,51,55}

1.3. Contact and adhesion between two rough surfaces

The ability to accurately model the interaction of two bodies in contact is of great importance in the field of tribology, which is the study of interacting surfaces and their associated friction, lubrication, and/or wear behavior. In actuality, even surfaces that appear very smooth are relatively rough since they are microscopically comprised of protuberances called asperities. Consequently, surfaces that appear to be in significant contact are actually in contact over an area known as the real area of contact. Situations where partial contact of surfaces occurs include micro/nano-scale systems, relatively hard surfaces where interfacial asperities undergo minimal deformation, and mixed lubrication, where the asperities partially support the loads at liquid-mediated interfaces.^{57–61} In all of these cases, the real area of contact must be resolved, usually as a function of the contact load, mechanical properties, surface topography, and adhesive and repulsive surface forces.

The seminal work on the contact of real surfaces is the Greenwood-Williamson (GW) model.⁶² It was developed to model the contact mechanics between two real surfaces by treating asperities as individual Hertzian hemispherical contacts of equal radii and varying heights.⁶³ The GW model can be used to predict the elastic contact stresses on the asperities from the two contacting bodies. While this model continues to be the foundation of most statistical rough surface models, it makes two key assumptions of neglecting both plasticity and adhesion, which can cause errors while evaluating contact of smooth surfaces under large loads.

Asperities on real surfaces usually enter the plastic regime even when light loads are applied.⁶⁴ Adhesion, which generally plays a smaller role in conventional macro-scale applications, becomes a stronger contributor to the resulting contact stress and surface deformation the smoother the surfaces are.⁶⁵ While some surface contact models have added plasticity^{66,67} or adhesion^{68,69} separately to the GW modeling framework, Chang, Etsion, and Bogy (CEB) developed a series of models to introduce both adhesion and the full spectrum of surface deformation regimes – elastic, elastic-plastic, and purely plastic.^{65,70,71} They introduced plasticity effects through the concept of a critical interference, which is the inter-penetration length (or maximum deformation) of an asperity into a surface at which plasticity first begins.⁷¹ Volume conservation and a uniform applied pressure were then assumed at each of the asperities in order to account for plasticity. They incorporated adhesion with the elastic-plastic deformation using their deformed asperity profiles in conjunction with the Derjaguin-Muller-Toporov (DMT) model.^{65,72}

The two primary models for adhesion are the Johnson-Kendall-Roberts (JKR) model⁷³ and the DMT model.⁷² The JKR model allows the adhesive force to affect the surface profile (i.e., shape) of a hemispherical contact and the forces outside of the contact area are neglected. The DMT model, on the other hand, does not allow the adhesive force to affect the profile of a hemispherical contact. Its profile follows a Hertzian profile instead and all adhesive forces, even those outside the contact area, are included. Tabor first postulated that these two models were limiting cases of the same general adhesive theory.⁷⁴ In other words, the DMT model is well-suited for hard materials with a small asperity radius such as metals, while the JKR model is better suited for soft materials with a large asperity radius.⁷⁵ The adhesive force depends on the chosen surface interaction potential employed in the adhesive model, the most common being the

Lennard Jones (LJ) potential.⁷⁶ Muller *et al.* developed a complete model accounting for Tabor's findings using the LJ potential.⁷⁷ The Maugis-Dugdale model was the first to develop a closed form solution for the JKR-DMT transition.⁷⁵ A comprehensive chart for determining which adhesion model to use for elastic contact was presented by Johnson and Greenwood.⁷⁸

The CEB models, due to their generality and simplicity, have been widely-adopted and extended by other authors.^{79,80} The assumptions used, however, do not capture the correct asperity behavior in the elastic-plastic regime. Kogut and Etsion (KE) presented a thorough comparison of the CEB models to finite element analysis (FEA) of an asperity under deformation and found significant deviation.⁸¹ They went on to present a new set of models to capture rough surface contact in the elastic-plastic regime, also including the effects of adhesion.^{64,81-83} Their adhesion model incorporated the DMT model in conjunction with the LJ potential. While the LJ potential is most often used as a first approximation for a given material system due to its simplicity, for many materials it can lead to poor predictions of physical properties.⁸⁴

1.4. Objective

The objective of this work is to use experimental and computational techniques to characterize the junction thermal conductance of organic-inorganic heterojunctions and elucidate its dependence on vibrational properties, molecular structure and contact characteristics of the organic and inorganic components comprising the junction.

1.4.1. Methods

1.4.1.1. Experimental

The thermal conductance of the SAM junctions and the thermal conductivity of all our other thin-film hybrid materials were measured using frequency domain thermorefectance

(FDTR) – a non-contact laser-based measurement technique.^{23,85,86} Our setup consists of an intensity modulated pump laser (488 nm) that periodically heats the sample surface (the topmost 95 nm Au film), leading to a periodic surface temperature oscillation. This temperature oscillation is probed using a second laser (532 nm) based on the high thermorefectance of the topmost Au lead. A mathematical solution to the heat diffusion equation for a semi-infinite layered system heated by a radially Gaussian and temporally periodic surface heat flux is fit to the phase lag of the sample surface temperature with respect to the heat flux to determine the unknown thermal conductance.^{23,87}

Thin films were characterized using a combination of experimental techniques – thermal conductivity (specifically metals) using four-point probe measurements (utilizing the Weidman Franz law); thickness using profilometry, ellipsometry, or X-ray reflectivity (XRR); atomic composition using X-ray photoelectron spectroscopy (XPS); molecular configuration using contact angle measurements, and surface roughness/topology using atomic force microscopy (AFM).

The SAMs were grown on smooth metal substrates created using a template-stripping technique^{88,89} and then a second metal (gold) thin film was printed onto them using a transfer-printing technique,^{50,90} all of which were performed in an ambient laboratory environment at a temperature of 296 K. Template-stripping ensures ultra-flat metal surface (root-mean squared roughness $\sim 3\text{-}5$ Å for a variety of metals) and transfer-printing prevents damage to the SAM, as has been observed when a high-energy deposition process such as sputtering or evaporation is used to create the junction.^{90–92}

1.4.1.2. Computational

Atomistic simulations describing the hybrid materials, which are essentially heterogeneous substances, require the use of large simulation domains that can accurately capture the inhomogeneity of the material system. The structural properties of the organic and inorganic components in the SAMs and particle brush system are what define the unique energy transport characteristics and thus need to be accurately described.

Molecular dynamics (MD) simulations solve the Newton laws of motion to predict the position and momenta of the particles in a system. They are classical in nature (i.e. do not account for quantum effects) but at sufficiently high temperatures (with respect to the Debye temperatures of the systems being simulated), the deviation from quantum calculations is small. MD is well-suited for studying hybrid systems as it can handle domains having tens of thousands of atoms and still not become computationally intractable. Numerous researchers have used MD to predict the thermal conductivity of polyethylene chains,⁹³ the thermal conductance of organic-inorganic junctions in both SAMs and nano-crystal arrays (NCAs),^{24,53,55,56,94} structural configuration of molecules on substrates^{24,95-97} and even diffusion of individual atoms or molecules on surfaces or within confined structures (e.g. carbon nanotubes).^{98,99} It is however imperative to use accurate empirical potentials to describe the atomic interactions – many studies describing the parameters of such potentials are available in literature and have been fit to macroscopic physical properties such as lattice constant or coefficient of diffusion among many others. We use MD in this study to model the thermal transport across the SAM junction and predict thermal conductance.

Lattice dynamics (LD) is also a powerful tool to study the vibrational characteristics of a system. Unlike MD, it is not a simulation technique that explores the entire phase space given a

set of degrees of freedom. LD calculations are carried out at a temperature of 0 K and assume the atoms to be connected to each other with springs described by empirical potentials. An eigenvalue problem is then solved to obtain the eigenmodes or vibrational modes (frequencies) of the system along with the eigenvectors of the atoms present in the computational domain.

For organic-inorganic interfaces, there has existed a discrepancy between experimental measurements of thermal conductance and the corresponding computational predictions.^{48,50,51,53,54,56,100} We resolve this discrepancy using a statistical contact mechanics model to estimate the percentage contact area at the SAM-transfer printed gold interface. The surface topology of the rough gold surface obtained from AFM measurements is transformed into an equivalent system described by hemispherical asperities at various heights. Such a transformation can be performed by assuming the surface height distribution to be Gaussian, a characteristic that can be verified from the AFM measurements. This mathematically transformed surface can then be input into the contact mechanics model to describe the percentage contact area when it is brought in contact with the SAM.^{81,82} We use this technique to gauge the quantitative effect it has on the experimental value of the junction thermal conductance.

1.5. Overview and Scope

A brief description of the chapters in this thesis and their scope is presented below:

1. Experimentally probe the thermal conductance of a SAM junction comprising metal leads and alkanethiol SAMs as a function of vibrational mismatch of the leads [**Chapter 2** – S. Majumdar *et al.* *Nano Lett.* **15**, 2985 (2015)].

The experimental details of fabricating SAM junctions using alkanethiols and metal substrates are discussed. These include the template-stripping method to create ultra-flat substrates, solution-based growth of SAMs, and the transfer-printing method to create the junction. Methods to characterize the junction with regards to its thickness and atomic composition are also described. These are followed by a discussion of FDTR and the mathematical framework used to measure the thermal conductance of the SAM junctions, based on which predictions are made regarding the effect of vibrational mismatch of the metal substrates on the junction thermal conductance.

2. Computationally predict the behavior of thermal conductance of a SAM junction (similar system as in experiments described in Chapter 2) as a function of vibrational mismatch of the metal leads [**Chapter 3** – S. Majumdar *et al. Nano Lett.* **15**, 2985 (2015)].

Details of the MD simulations and LD calculations are presented, which are used to model the thermal transport through the SAM junction and calculate the vibrational modes of the system. Empirical potentials required for modeling the atomic interactions were obtained from literature and used in our simulations. The observed trends from simulation are compared to the FDTR measurements from Chapter 2; hypotheses regarding the nature of vibration/phonon scattering at the interfaces within the SAM junction are made and proven.

3. Develop a statistical framework to predict surface contact within SAM junctions using topographical measurements of the real samples used in the experiments [**Chapter 4** – J.A. Sierra-Suarez *et al. J. Appl. Phys.* **119**, 145306 (2016)].

The derivation and validation of a new statistical contact mechanics model is presented that can accurately handle the adhesion between two bodies interacting through covalent bonds.

The covalent bond is characterized using a Morse potential, a more specialized interaction than the standard Lennard-Jones potential that is mainly for van der Waals interactions. The model also has the capability to handle bodies that have a layered structure composed of more than one kind of atomic species. It is used to predict the percentage contact area between contacting rough surfaces, which is then used to resolve the difference between thermal conductance measurements (Chapter 2) and simulation predictions (Chapter 3).

4. Investigate the cooperative behavior between molecules and its affect on thermal transport across molecular junctions using mixed and partially populated SAM junctions (**Chapter 5 – in preparation**).

The effect of cooperative behavior between molecules on the thermal conductance of SAM junctions is investigated using both experimental and computational techniques. The SAMs used here are binary species (i.e. have two kinds of molecules) and the experimental details of their preparation and characterization (specifically contact angle measurements) are also discussed.

5. Other projects [**Chapter 6** – C. Mahoney *et al. Polymer* (2016), W.-L. Ong *et al. J. Phys. Chem. C*, **118**, 7288 (2014), K.T. Regner *et al. Rev. Sci. Instrum.* **84**, 064901 (2013)].

These projects helped me apply the knowledge I gained from my primary research focus in studying other hybrid materials systems and pump-probe based experimental techniques.

a. Details of FDTR measurements of nanocomposite systems comprised of nanoparticle-polymer brush resins are discussed. The observed trends are used to study the effect of nanoparticle concentration and brush-polymer matrix interactions on the thermal conductivity of the system.

b. MD simulations to model thermal transport in nanocrystal arrays are discussed with emphasis on the variation of thermal properties with the core diameter, packing density of ligands and core-ligand mass mismatch.

c. The experimental details of the broadband FDTR technique are presented, which can be used for phonon spectroscopy measurements of various materials.

6. In Chapter 7, the major contributions of my work and suggestions/scope for future research efforts in this field are provided.

2. Chapter 2: Experimental investigation of thermal conductance in organic junctions with metal leads

2.1. Introduction

The lifetime and efficiency of such micro- or nano-scale devices is affected by their operating temperature so that it is critical to know their thermal properties.^{20,21} For hybrid materials, the thermal conductance of the internal organic-inorganic interfaces plays a key role.^{22–24} Our focus here is on self-assembled monolayers^{32,48–51,55} (SAMs) – two-dimensional periodic arrays of organic molecules that form spontaneously from solution on metal or dielectric surfaces.

There has been no systematic investigation on the effect of the vibrational properties of the leads on thermal transport across SAM junctions. Experimental data are only available for metal-SAM-dielectric junctions,^{48,50,51,55} wherein the vibrational properties of the two leads are highly mismatched. Using metals, it is possible to select leads with varying degrees of vibrational mismatch. In this study, we use thermoreflectance experiments and MD simulations of metal-SAM-metal junctions to investigate the effect of vibrational spectra overlap on the junction thermal conductance. We find that the thermal conductance (per molecule) is highest when the leads are the same and reduces as the vibrational mismatch increases. Furthermore, we reconcile the discrepancy between experimentally-measured values of thermal conductance and those predicted from simulations by estimating the percentage contact area in the SAM junction using contact mechanics models¹⁰¹ informed by atomic force microscopy (AFM) surface roughness data of our leads.

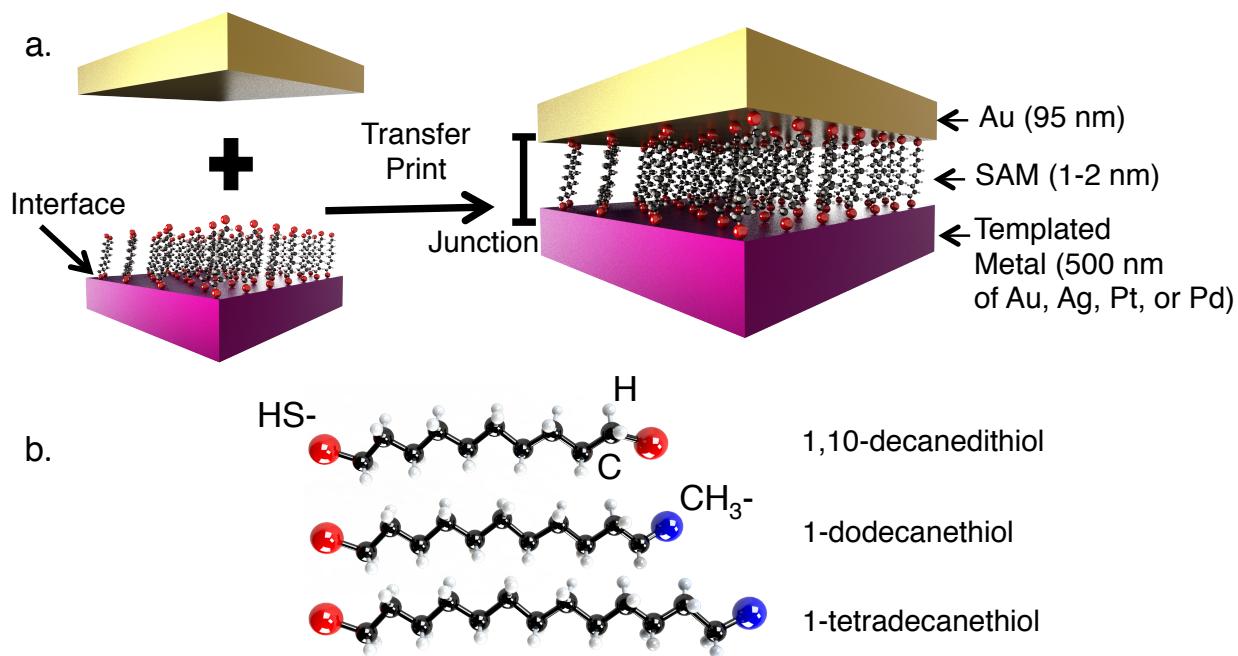


Figure 2.1. (a) Schematic diagram of the transfer printing process to create a SAM junction. A 95 ± 5 nm Au layer is transfer printed onto a SAM grown on a $475\text{--}530 \pm 20\text{--}30$ nm (see **Table 2.4**) templated metal substrate. (b) Straight chain alkane-based molecules used to create the SAMs in this study (1,10-decanedithiol, 1-dodecanethiol, and 1-tetradecanethiol).

Metal-SAM-metal junctions were fabricated using a transfer printing technique⁹⁰ (Figure 2.1a). Molecules of 1,10-decanedithiol ($\text{C}_{10}\text{H}_{22}\text{S}_2$), 1-dodecanethiol ($\text{C}_{12}\text{H}_{26}\text{S}$), and 1-tetradecanethiol ($\text{C}_{14}\text{H}_{30}\text{S}$), as shown in Figure 2.1b, were used to grow the SAMs. Both dithiols and monothiols were considered to probe the effect of end-group chemistry. The SAMs were grown on ultra-flat metal leads that were made using a templating procedure.^{89,102} These samples were then immersed in a dilute solution (0.1 mM) of the SAM molecules in ethanol for 18-24 hours.^{27,32} A 95 ± 5 nm Au film (originally evaporated onto a Si wafer, then lifted off using a PDMS stamp) was then transfer printed onto these structures to complete the junction. Thus, the junctions have the configuration metal-SAM-Au, where the bottom metal lead is Au, Ag, Pt, or

Pd, the top lead is Au, and the SAM is an alkanedithiol or alkanethiol. At least five samples were made of each configuration.

The metal-SAM interface was characterized through X-ray photoelectron spectroscopy (XPS) measurements to study the atomic composition and bonding environment. The measurements confirmed the presence of the SAM and the absence of a parasitic oxide layer that could affect SAM coverage and add thermal resistance. Ellipsometry measurements were also performed to measure the SAM thickness and were found to agree with previous studies, further confirming the presence of a pure monolayer.^{28,32}

2.2. Sample preparation and characterization

2.2.1. *Templated metal synthesis*

First, metal layers of Au, Ag, Pt or Pd (475 ± 25 nm) was sputtered onto a Si substrate having a 1 μm thermally grown oxide layer (wafer cleaned using acetone, isopropyl alcohol and DI water, and later dried in nitrogen gas) using a Perkin Elmer 6J sputtering system. The thickness of the metal was measured using a KLA Tencor P-15 profilometer. Then, Si templates (2 cm \times 2 cm) were attached onto the metal surface using epoxy (EPOTEK 377, baked at 150°C for 2 hours), as shown in Figure 2.2a. About 40 templates can be attached to a 4" diameter Si wafer, which can then be stored for months without deterioration. The templates were then stripped off using a razor blade, as shown in Figure 2.2b. Placing the edge of the razor blade on one side of the template and applying a gentle pressure to lift-off the template from the wafer achieved this. The template-stripping exposed the smooth metal surface, previously attached to the thermal oxide layer of the Si wafer, having a surface roughness of 4 ± 1 Å as measured by atomic force microscopy (AFM), consistent with prior Au templates.^{89,102}

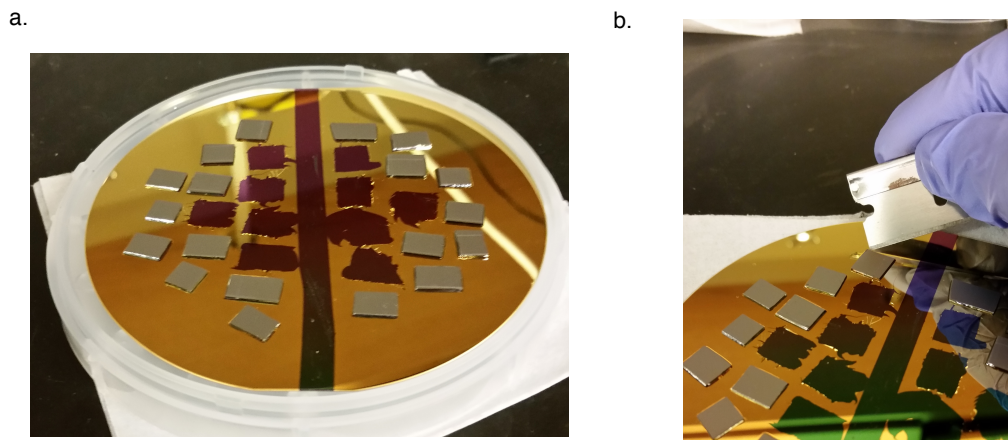


Figure 2.2. (a) Si templates attached to a gold substrate (sputtered onto an Si wafer) using EPOTEK 377 epoxy, after curing. (b) Si template being stripped off using a razor blade.

The templated metal leads were then immersed for 24 hours in dilute (0.1-1 mM) solutions of the SAM forming molecules (1,10-decanedithiol, 1-dodecanethiol and 1-tetradecanethiol, purchased from Sigma Aldrich) in ethanol, as shown in Figure 2.3. The samples are then removed, washed with ethanol for 10 s and then dried in nitrogen gas for 10 s.

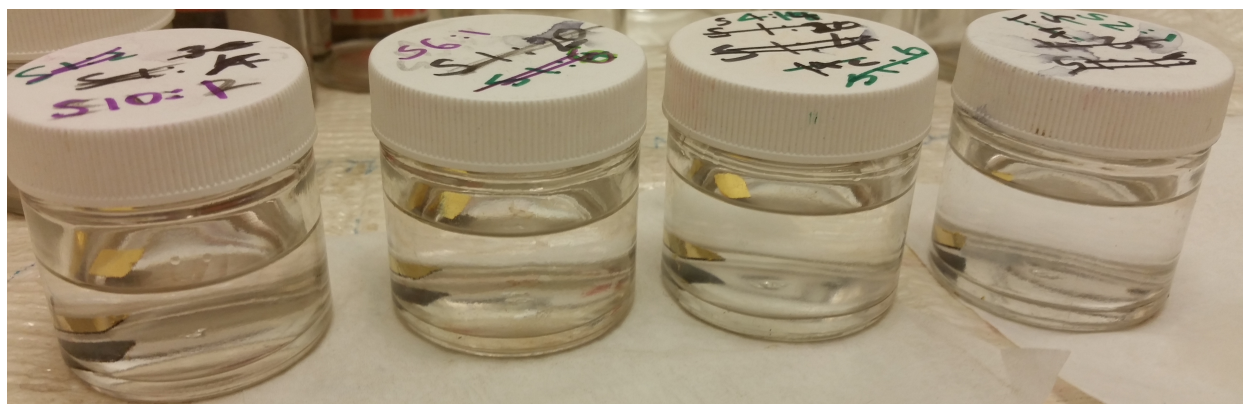


Figure 2.3. Dilute solutions of SAMs (~0.1-1 mM) in ethanol having template metal leads immersed in them.

For the case of the 1,10-decanedithiol SAM solutions, dithiothreitol (DTT – bought from Sigma Aldrich, 1-10 mM) was also added to the solution mixture. This ensured the dithiol molecules did not oxidize and form bi- or multi-layers on the metal surface.⁵⁰ Another effective

method to use the DTT was to create a separate 1-10 mM solution of DTT in ethanol and immerse the metal leads having SAMs into it after the initial 24 hours (the original SAM solution was kept free of DTT in this case). In this procedure, the DTT removed any extraneous molecules bonded to the SAM without affecting the initial SAM structure during its growth stage. The leads were immersed in the DTT solution for 30 min and then removed, washed in ethanol and dried in nitrogen gas like the other samples, similar to the procedure described above.

2.2.2. Transfer printing procedure

After the immersion process, a second Au layer of 95 ± 5 nm thickness (measured using a X'Pert Pro MRD x-ray diffractometer) was printed on to this Au surface with a SAM layer using a PDMS stamp (Sylgard 184 Elastomer Kit, bought from Fisher – 1:3.5 mixing ratio of base and curing agent), thus forming the metal-SAM-metal junction.^{50,90} This 95 nm Au was first grown on a Si substrate having a native oxide layer (wafer cleaned using acetone, isopropyl alcohol and DI water, and later dried in nitrogen gas) using a Ultek E-Beam evaporator. Its surface was then covered with a 1:10 by mass polyvinyl alcohol (PVA) solution (SigmaAldrich MW: 18000-23000 with 89% hydrolization) in DI water. This solution was prepared by dissolving the PVA (solid form) in DI water with constant stirring (150 rpm) at 60° C for 24 hours. The PVA solution provides a protective layer on the Au surface to prevent crack formation during printing. The solution was dried by heating the sample at 85° C on a hot plate for 3-4 min.

The sample was then stuck onto the lab counter with a doubles-sided tape. The edges of the Au film were removed using a razor blade since these may not be completely flat. A PDMS stamp (cleaned with scotch tape and nitrogen) was then pressed onto the (PVA + Au) surface and

quickly lifted off, peeling off the Au from the Si substrate. This stamp was then pressed onto the SAM and rigidly held for 120 s while placing the assembly on a hot plate heated to 85° C. The stamp was then slowly peeled off leaving behind the Au transducer on the SAM. The PVA was washed off with DI water and the sample was dried under nitrogen gas.

2.2.3. XPS measurement

X-ray photoelectron spectroscopy (XPS) measurements were performed on the SAM (1-dodecanethiol) on the metal substrates to evaluate the presence of oxide layers on the metal surfaces. The oxide layer can provide additional thermal resistance and impact our interpretation of the thermal conductance measurement. It can also affect the coverage of the alkanethiol molecules on the surface.

The XPS studies were performed with a ThermoFisher ThetaProbe instrument with a hemispherical energy analyzer. The monochromated X-ray beam was focused near the center of each sample on a 200 μm spot with an electron flood gun running continuously for charge neutralization. Survey spectra were obtained across a binding energy range of 50-1200 eV by averaging 5 sequential scans taken with 0.2 eV step size, 0.05 s dwell time, and 200 eV pass energy. Higher-resolution spectra were obtained across narrow ranges containing characteristic binding energy peaks for C 1s (280-290 eV), O 1s (527-537 eV), S 2p (159-169 eV), Pd 3d (330-345 eV), Ag 3d (360-380 eV), Pt 4f (64-87 eV), and Au 4f (81-91 eV). These spectra were obtained by averaging 10 sequential scans taken with 0.05 eV step size, 0.05 s dwell time, and 100 eV pass energy.

It can be seen in Figure 2.4 that there is no peak for O atoms indicating the absence of any significant oxide layer.

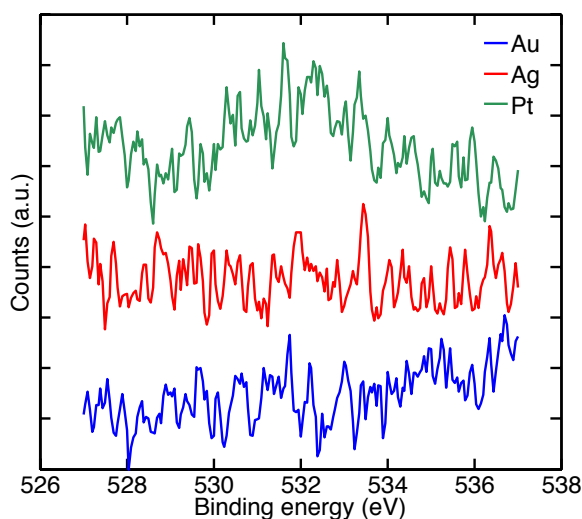


Figure 2.4. XPS measurement showing binding energy spectra O 1s electrons for samples having 1-dodecanethiol grown on Au, Ag, Pt and Pd leads. No peaks (near 532 eV) can be seen indicating absence of oxide layer. Plot for O 1s on Pd is not shown as the Pd $3p_{3/2}$ peak also lies within this energy range.

Peaks can be seen for both S and C atoms, as shown in Figure 2.5. The presence of S peaks indicates the presence of a SAM. They are also shifted relative to each other for each substrate due to the slightly different bonding energies between the S atom and different metal substrates. The C atoms have a large peak, as they constitute most of the initial 1-1.5 nm of sample depth. The peaks are symmetrical indicating a pure monolayer formation.¹⁰³ The height of the C peak with and without the SAM differs significantly and indicates that a high density of molecules get adsorbed on the metal surface upon SAM formation. These XPS measurements agree with prior measurements in literature.²⁷

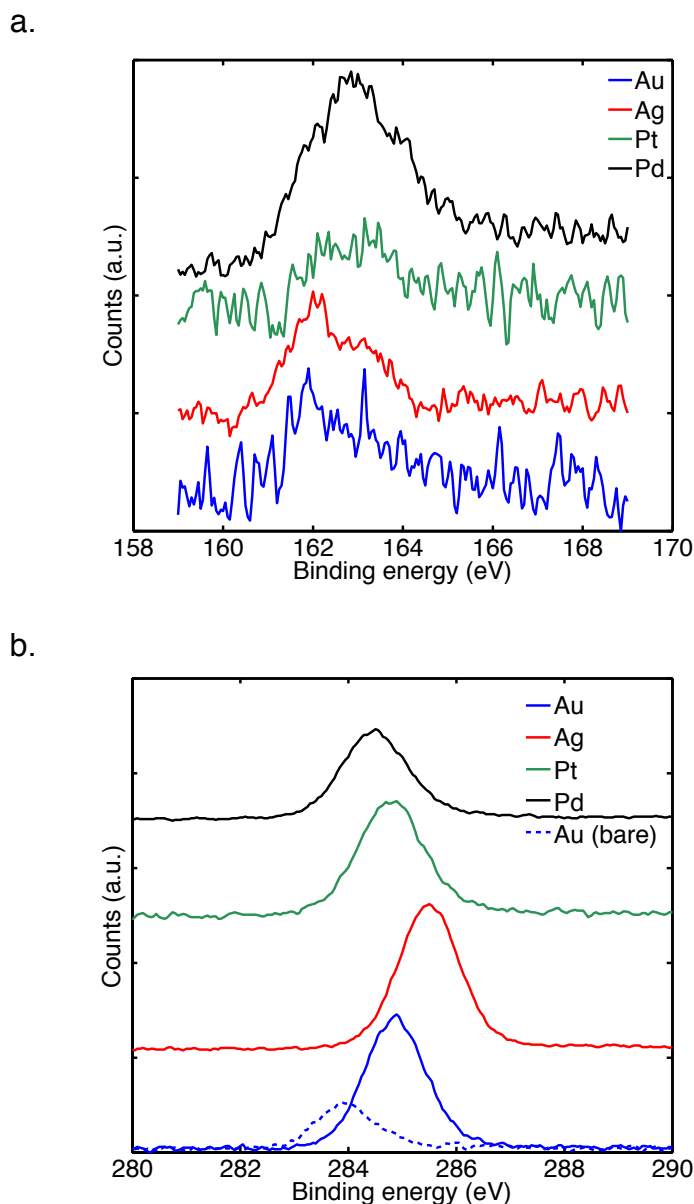


Figure 2.5. (a) XPS measurement showing binding energy peaks for S 2p electrons indicating formation of the SAM. (b) XPS measurement showing binding energy peaks for C 1s electrons. Measurements for samples with SAM have larger peaks indicating large presence of C atoms (due to presence of SAM layer).

2.2.4. Ellipsometry measurement

The SAM thicknesses are measured by phase-modulated ellipsometry with a Picometer Ellipsometer (Beaglehole Inc.). A homogeneous, stratified thin-film optical model consisting of the metal substrate, monolayer, and ambient air was used. The complex refractive index of the

underlying metal substrate (Au, Ag, Pt or Pd) is first determined from a multi-angle scan of the bare substrate, and the monolayer thickness is calculated assuming a refractive index of 1.5 for the alkanethiols. Errors represent the 95% confidence interval from fitting the monolayer thickness. Table 2.1 has the variation of SAM thickness with molecule length and substrate.

Table 2.1. Refractive indices for all metal leads and SAM thicknesses. Measured using ellipsometry.

Metal	SAM Thickness (Å)		
	S-C ₁₀ -S	S-C ₁₁ -C	S-C ₁₃ -C
Au	14±2	17±1	22±2
Ag	8±1	11±1	16±1
Pt	15±1	13±1	15±1
Pd	20±2	19±2	22±2

2.2.5. Debye temperatures of leads

The vibrational spectrum of the metal lead on which the SAM is grown is characterized by its Debye temperature. The Debye temperatures for the leads are listed in Table 2.2.¹⁰⁴

Table 2.2. Debye temperatures of the metal leads.

Metal	Debye temperature (K)
Au	170
Ag	215
Pt	240
Pd	275

2.3. Frequency domain thermorefectance

2.3.1. Experimental setup

Frequency domain thermorefectance (FDTR) is a non-contact laser-based thermal measurement technique for measuring the thermal transport characteristics of thin films.^{23,85} Two continuous wave lasers (Coherent Inc) are used to simultaneously heat the sample surface (Au transducer surface) and probe the surface temperature. A 488 nm pump beam is intensity modulated in frequency range of 100 kHz – 10 MHz and imparts a periodic heat flux to the sample surface. A 532 nm probe beam simultaneously monitors the thermal response of the Au surface by thermorefectance. The pump and probe signals are measured using a radiofrequency lock-in amplifier (Stanford Instrument, SR844) and we record the frequency dependent phase lag of temperature (probe) with respect to heat flux (pump). This phase lag data is then fit with a thermal conduction model⁸⁷ using the known parameters in Table 2.3 to determine the unknown thermal conductance of the SAM junction.

Table 2.3. Parameters used in solution of heat diffusion equation for FDTR measurements. The SAM thermal conductance (G) is the only fitting parameter.

	Au	SAM	Metal	Epoxy
Thermal conductivity (W/m-K)	4 point probe measurement (see Table S4)	Fitting parameter ($k = G*L$)	4 point probe measurement (see Table S4)	0.12±0.01 (independently measured by FDTR)
Density (kg/m³)	19000	1	Literature ¹⁰⁵	1250
Specific heat (J/kg-K)	130	1	Literature ¹⁰⁵	900
Thickness (nm)	95±5	1e-9 (L)	Profilometry measurement (see Table S4)	1e4

2.3.2. Uncertainty analysis

The uncertainty in a single FDTR measurement ($\sim 10\%$) is due to uncertainties in thicknesses, thermal conductivities, specific heats, and densities of the sample layers, and laser spot size used within the thermal model.^{23,85} The thermal conductivities of the metals were measured through sheet resistance measurements of co-sputtered metal films on dielectric substrates using the Weidemann-Franz Law and are listed in Table 2.4.

Table 2.4. Thermal conductivities of metal films.

Metal	Thickness (nm)	Thermal conductivity (W/m-K)
Au (top layer)	95 \pm 5	185 \pm 10
Au (bottom layer)	475 \pm 25	205 \pm 11
Ag	530 \pm 30	380 \pm 21
Pt	470 \pm 20	67 \pm 4
Pd	500 \pm 20	67 \pm 4

The densities and heat capacities used for the metals are standard values from literature.¹⁰⁵ The SAM is modeled as an interface having negligible heat capacity and density and a thickness of 1 nm. The major sources of uncertainty are from the thickness and thermal conductivity bottom (thicker) metal layer. A conservative estimate of the thickness uncertainty is 5% (which satisfies all thickness variations for all the four metals) obtained from profilometry measurements, which leads to a 5% uncertainty in the thermal conductivity inferred from the Weidemann-Franz Law.

The properties of the epoxy were obtained from Epotek and we independently verified its thermal conductivity using FDTR. The sample for this measurement was comprised of a 475 ± 25 nm template Au layer on a $10 \mu\text{m}$ layer of epoxy cured on a Si substrate.

Variations in thermal conductance measurements from different spot locations, even though small ($\sim 5\%$), must still be accounted for when specifying the uncertainties in the reported values in Figure 2b. For the case of N independent measurements x_i , each having a standard deviation σ_i , (based on the uncertainty in a single measurement), the final reported value \bar{x} and its standard deviation $\bar{\sigma}$ (which is how we specify the size of the error bars) is

$$\bar{x} = \frac{1}{N} \sum_{i=1}^N x_i, \quad (2.1)$$

$$\bar{\sigma}^2 = \left[\frac{1}{N} \sum_{i=1}^N (\sigma_i^2 + x_i^2) \right] - \bar{x}^2. \quad (2.2)$$

To obtain Equation 2.2, we assume that each measurement x_i can be characterized by its own Gaussian distribution and that σ_i is obtained by independent sampling of the distribution. We also assume this sampling is sufficiently large to give an unbiased estimate of the variance σ_i^2 .

2.4. Molecular footprint

The molecular footprint is the area occupied by one molecule of the SAM on a particular substrate. The footprints for alkanethiols on the metal substrates measured using a combination of XPS, reflection absorption infrared spectroscopy, and scanning tunneling microscopy techniques are listed in Table 2.5.^{28,32,106–108}

Table 2.5. Molecular footprints of 1,10-decanedithiol on a metal leads.

Metal	Molecular footprint ($\text{\AA}^2/\text{molecule}$)
Au	$21.7 \pm 1.7^{32,106}$
Ag	18.9 ± 1.9^{28}
Pt	19.2 ± 1.6^{107}
Pd	19.6 ± 1.5^{108}

2.5. FDTR results

The SAM junction thermal conductance was measured at an ambient temperature of 296 K using frequency domain thermoreflectance (FDTR), a non-contact laser-based measurement technique.^{23,85} An intensity modulated pump laser (488 nm) periodically heats the sample surface (the topmost 95 nm Au film), leading to a periodic surface temperature oscillation. This temperature oscillation is probed using a second laser (532 nm) based on the high thermoreflectance of the topmost Au lead. An analytical solution to the heat diffusion equation for a semi-infinite layered system heated by a Gaussian-shaped periodic surface heat flux is fit to the phase lag of the sample surface temperature with respect to the applied heat flux.^{23,87} Representative phase lags for Au-alkanedithiol-Au and Au-alkanethiol-Au SAMs are plotted in Figure 2.6a versus modulation frequency. The solid lines correspond to the solution of the heat diffusion equation having the junction thermal conductance as the only fitting parameter. There is a stark difference in the phase responses between these two configurations, with junction thermal conductances of $65 \pm 7 \text{ MW/m}^2\text{-K}$ and $34 \pm 3 \text{ MW/m}^2\text{-K}$. They also differ from the phase response of a Au-Au interface (no SAM), also plotted in Figure 2.6a. These phase responses demonstrate the sensitivity of our measurements to the possibility of metal-metal shorting across

the SAMs and indicate that such shorting is not present. Supporting this conclusion, previous studies of SAM junctions created through transfer prints have shown a high degree of repeatability in creating junctions without shorting between the electrodes.^{43,109} We note that direct indication of metal-metal shorting is possible through current-voltage measurements but these experiments were beyond the scope of this study. Measurements were made for at least five different laser spot locations on each sample. These results demonstrate the sensitivity of the phase response in FDTR to the presence and chemistry of the SAM.

The measured junction thermal conductances for all configurations are plotted in the left panel of Figure 2.6b versus the Debye temperature (T_D) of the metal contact on which the SAM is grown (for a list of Debye temperatures, see Table 2.2). The uncertainty of an individual thermal conductance measurement (as reported in Figure 2.6a) was calculated from the fitted thermal model by accounting for the uncertainty in the properties of the layered sample.^{23,85} The error bars in Figure 2.6b represent the combination of the uncertainties of the individual measurements with the variability arising from different spot locations and samples using a statistical model, details of which are provided in Section 2.3.2. The Debye temperature is an estimation of the temperature at which all vibrational states in a system are activated. It can thus be used to characterize the extent of the vibrational frequency spectrum for a material.^{52,110,111} We use the Debye temperature as a measure of the vibrational mismatch between the two metal leads (Au with either Au, Ag, Pt, or Pd) in a particular SAM junction. We note that this is a simple approximation but is sufficient to illustrate our findings of the effect of vibrational mismatch on the junction thermal conductance. Au has the lowest Debye temperature ($T_{D_{Au}} = 170$ K) and thus Debye temperature mismatch between the leads increases (i.e., the ratio $T_D/T_{D_{Au}}$ increases) as we move from left to right along the horizontal axis in both panels of Figure 2.6b.

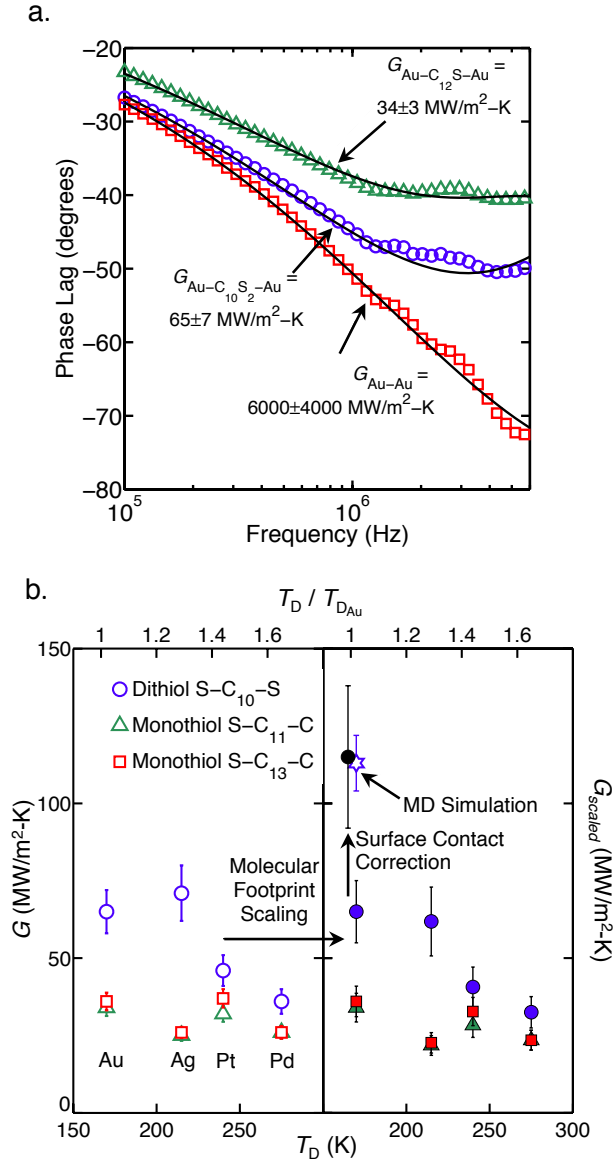


Figure 2.6. (a) FDTR phase responses for junctions with 1,10-decanedithiol, 1-dodecanedithiol, and no molecules are clearly distinguishable. Solid lines represent the best-fit solutions of the heat diffusion equation for a semi-infinite layered system heated by a Gaussian-shaped periodic heat flux at the surface. (b) Variation of junction thermal conductance G with the Debye temperature of the templated metal substrate on which the SAM is grown. The raw experimental data (left panel, unfilled data points) are scaled by the molecular footprint (right panel, filled data points) to isolate the effect of the leads vibrational spectra on G . Also plotted is the MD prediction of G for a Au-(1,10-decanedithiol)-Au junction (unfilled star) and percentage area corrected experimental thermal conductance (filled black circle), which has been displaced slightly to the left for clarity. All experiments were performed at an ambient temperature of 296 K.

The 1,10-decanedithiol SAMs exhibit a larger range of junction thermal conductances (mean values of 36 to 71 MW/m²-K) than either the 1-dodecanethiol or 1-tetradecanethiol SAMs (25 to 37 MW/m²-K). The two monothiols have comparable junction thermal conductance values for all configurations, corroborating the previously reported length independence for alkane chains having more than ten carbon atoms.^{48,49,52,110} Our measurements are comparable to previous measurements of junction thermal conductance of Au-1,10-decanedithiol-GaAs⁴⁸ (28±3 MW/m²-K) and Au-(11-mercapto-undecyltrimethoxysilane)-quartz⁵⁰ (65±5 MW/m²-K) junctions. As further confirmation, we also fabricated Au-decanedithiol-GaAs junctions and measured a thermal conductance of 32±4 MW/m²-K, in agreement with R.Y. Wang *et al.*'s⁴⁸ result.

The junction thermal conductance plotted in the left panel of Figure 2.6b is related to the molecular footprint (i.e., the projected area per molecule) of the SAM, which depends on the lead on which it is grown.^{28,32,107} To isolate the effect of the vibrational properties of the leads from the footprint effect, we scaled the measured experimental data (G) using the molecular footprint of the 1,10-decanedithiol SAM (σ_{SAM-Au}) grown on Au according to:

$$G_{scaled} = \frac{\sigma_{SAM-metal}}{\sigma_{SAM-Au}} G. \quad (2.3)$$

Here, $\sigma_{SAM-metal}$ is the molecular footprint of the SAM on the bottom metal lead (Au, Ag, Pt, or Pd). The scaled data (G_{scaled}) is plotted in the right panel of Figure 2.6b. The scaled junction thermal conductance decreases as the difference in the Debye temperatures of the leads increases. The reduction is strong for the 1,10-decanedithiol SAMs and weak for the 1-dodecanethiol and 1-tetradecanethiol SAMs. The values of $\sigma_{SAM-metal}$ for the systems investigated here are within 15% of each other, a range comparable to the error bars associated with the thermal conductance measurements plotted in Figure 2.6b. The total range of thermal

conductances of the Au-alkanedithiol-metal systems is larger than this uncertainty, giving us confidence in the observed decreasing trend. We hypothesize that the decrease happens as the combined overlap between the density of states (DOS) of the leads and the discrete vibrational states of the molecules decreases, or equivalently as the Debye temperatures of the leads diverge. The weak trend for the monothiol SAMs is likely due to the weak metal-CH₃ bond acting as the dominant resistance to thermal transport, thus overpowering the effect of the mismatched metal leads.

2.6. Contact area correction

Though in agreement with similar measurements,^{48–51,55} our thermal conductance for the Au-alkanedithiol-Au junction (65 ± 7 MW/m²-K) is a factor of two lower than our MD prediction (113 ± 9 MW/m²-K, plotted as a white star in the right panel of Figure 2.6b, discussed later) and the MD prediction (200 ± 60 MW/m²-K) by Luo and Lloyd.^{56,112} We hypothesize that a major source of this discrepancy is that the surface roughness of the Au leads causes imperfect surface contact within the junction. To test this hypothesis, we calculated the percentage contact between the leads upon transfer printing using a rough surface contact model.¹⁰¹ The model is an extension to the work of Kogut and Etsion⁸¹ (the KE model), who included finite element analysis (FEA)-validated plasticity effects while determining surface deformations. The rough surface is modeled as a collection of spherical asperity tips with areal density and dimensions based on surface topography data obtained using AFM (shown in Figure 2.7a). The contact between the two rough surfaces is made mathematically-equivalent to a single rough surface in contact with a smooth one, as illustrated in Figure 2.7b, as originally proposed by Greenwood and Tripp.¹¹³ The balance between the reaction pressure and attractive adhesive pressure allows us to predict the contact area of the asperities.

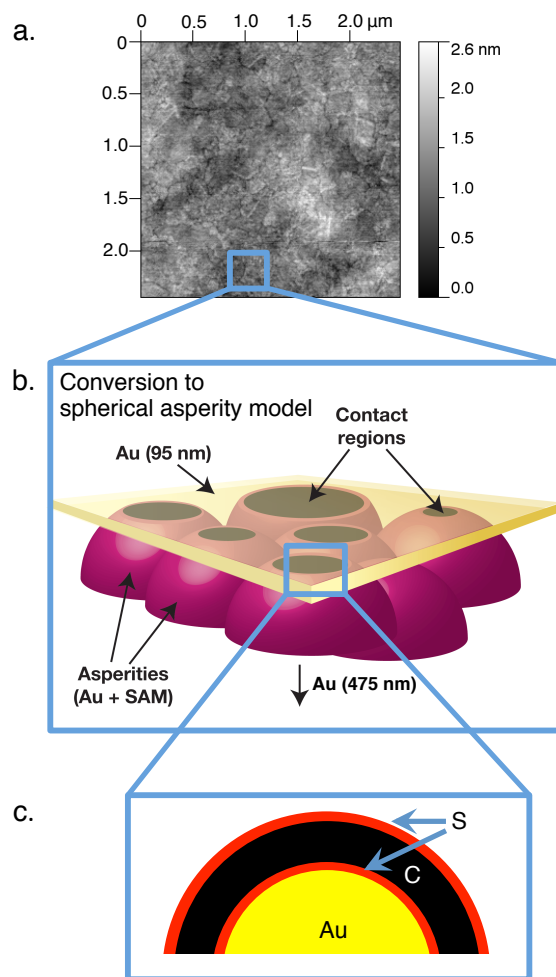


Figure 2.7. (a) AFM image of a templated Au lead (RMS roughness $4 \pm 1 \text{ \AA}$). (b) Schematic diagram of two rough surfaces represented as spherical asperities (475 nm Au + SAM) in contact with a flat, undeformable surface (95 nm Au). (c) A single asperity is a layered, composite structure consisting of an outer shell of the SAM molecules [S (red) and C (black) atoms] enclosing an inner Au core. Interactions between all atoms and the upper Au surface are considered when calculating the percentage contact area.

Previous studies that predicted percentage contact area only considered adhesion stemming from van der Waals bonding at the surface characterized by a Lennard-Jones (LJ) potential.^{72,73,114} The strong thiol-Au interaction^{97,98} in our system required us to modify the adhesion force calculation derived by Derjaguin *et al.*⁷² and Muller *et al.*¹¹⁴ (the DMT model) by using a Morse potential instead of the LJ potential.¹⁰¹ Furthermore, previous applications of the

DMT model considered asperities comprised of one material. In our case, we have a SAM grown on Au, which creates a composite asperity, as shown in Figure 2.7c. To account for the SAM, the total adhesion force between the asperity and the flat surface was assumed to be a linear combination of adhesion forces for each shell. Our contact model, like the DMT and KE models, is based on the assumptions originally made by Greenwood and Tripp:¹¹³ (i) the analysis is valid for a surface profile that is isotropic with a Gaussian distribution of peak heights, (ii) a single asperity tip is not influenced by the deformation of neighboring asperities and the bulk solid behind the asperity layer is rigid. In addition, we also assumed the SAM layer has the same elastic properties as the deforming metal asperity it is grown on.

From our analysis, we predict that the percentage contact area A^* for the Au-alkanedithiol-Au junction to be $56 \pm 21\%$. The measured junction thermal conductance can be related to A^* and that of a perfect contact through the analysis described by Seong *et al.*¹¹⁵ and Prasher *et al.*¹¹⁶ Together with the experimental measurement of 65 ± 7 MW/m²-K for the Au-alkanedithiol-Au junction, we thus predict a perfect contact junction thermal conductance of 115 ± 22 MW/m²-K, which is plotted as a black circle in the right panel of Figure 2.6b. This value agrees with our MD prediction and supports our hypothesis that the major source of the discrepancy between experimental measurements and MD simulations is incomplete contact (another source could be the presence of a monolayer of water on the SAM though XPS measurements could not confirm this). Although measured RMS roughnesses of templated Ag, Pd, and Pt samples are similar to that of Au,⁸⁹ new interatomic potentials for the thiol-metal bonds would be required to apply our contact mechanics model to those junctions. As such, we cannot rigorously confirm the universality of this result.

In summary, we experimentally probed how the selection of leads affects the thermal conductance of metal-SAM-metal junctions. We found the junction thermal conductance to decrease as the vibrational mismatch increases. The discrepancy between the experimental measurement of the Au-alkanedithiol-Au junction thermal conductance and that predicted from MD simulations was resolved by correcting for the true contact area realized in the experiments using a contact mechanics model for rough surfaces. We thus see that thermal transport properties of SAM junctions can be manipulated by adjusting lead material as well as end-group chemistry.

3. Chapter 3: Computational techniques to probe thermal transport scattering mechanisms in organic junctions with metal leads

3.1. Molecular dynamics simulation

3.1.1. *Structure relaxation and non-equilibrium simulations*

In Chapter 2, we experimentally demonstrated that the thermal conductance of self-assembled monolayer (SAM) junctions with metal leads decreases as the vibrational mismatch between the leads increases. We attributed this behavior to the existence of elastic scattering at the metal-SAM interfaces. To further probe these vibrational coupling and scattering effects in the SAM junctions presented in Figure 2.6b, we performed MD simulations of Au-alkanedithiol-Au structures representative of the experimental setup. All molecular dynamics simulations were performed using LAMMPS.¹¹⁷

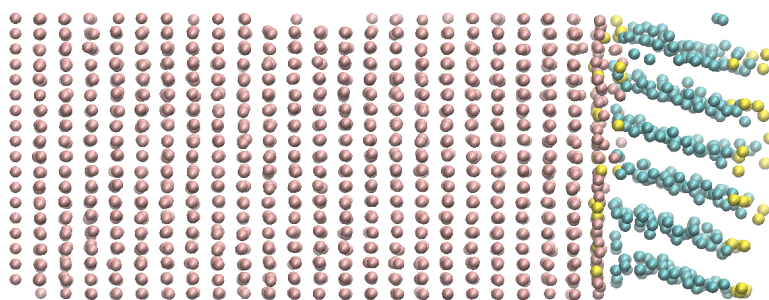


Figure 3.1. Relaxed structure of 1,10-decanedithiol on Au lead at a temperature of 300 K from an *NVT* ensemble using MD simulation.

The SAM was first created on an Au substrate that had a cross-sectional area of 2.5×2.5 nm² and represented a region of perfect contact. The SAM layer was placed on the (111) surface of Au to form a $R(\sqrt{3} \times \sqrt{3})$ packing arrangement that exhibits a coverage of 21.7 ± 1.7 Å² per molecule.^{32,106} The molecules were first placed exactly above the 3-fold hollow sites of the (111)

surface. This system was equilibrated in an *NVT* (canonical) ensemble at a temperature of 300 K, as shown in Figure 3.1, for 1.5 ns with a timestep of 1 fs. This resulted in a steady-state tilt angle of $26 \pm 5^\circ$ for the molecules, which agrees with experimental observations of $30 \pm 7^\circ$.³² The second lead was then placed above the molecules so as to create the metal-SAM-metal junction. This structure was then relaxed for 1.5 ns under the *NVT* ensemble at a temperature of 300 K, with the final structure shown in Figure 3.2. Non-equilibrium molecular dynamics (NEMD) was employed to predict a temperature difference across the junction for a known heat flux q'' . The junction thermal conductance was calculated using $G = q''/\Delta T$, where ΔT is the temperature drop across the entire junction.

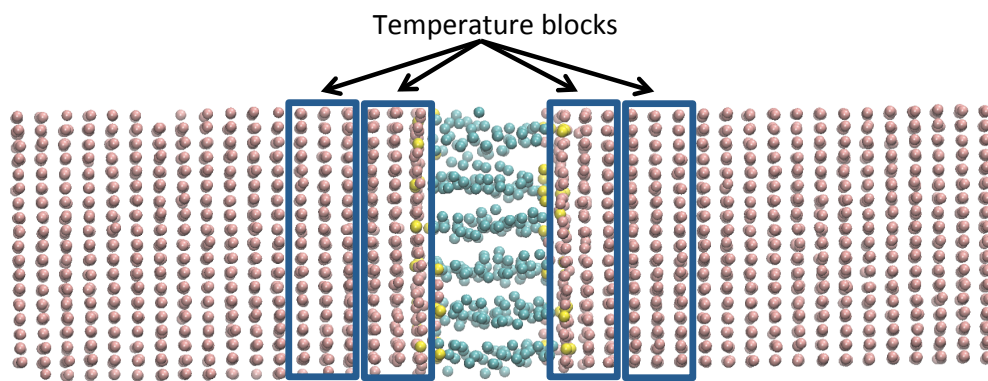


Figure 3.2. Relaxed structure of 1,10-decanedithiol junction comprising two Au leads at 300 K from an *NVT* ensemble using MD.

Kinetic energy was then added/removed from the heat source/sink at to the ends of the two Au blocks at a rate of $q = 10^{-4}$ eV/ns. Each atom in the source/sink has an equal amount of heat added/removed from it. After 2.5 ns, temperature data were collected for blocks of 270 atoms (see Figure 3.2) for a period of 20 ns, averaged every 100 steps. This length of simulation was found to be sufficient to reach a steady state and minimize noise in the data.

The Au-Au interactions leads were modeled using an embedded atom method (EAM) potential¹¹⁸ that accurately reproduces the maximum frequency in the density of states for Au. The thiol – Au interaction was modeled using a Morse potential.⁹⁸ The united atom method was used to model the SAM molecules.¹¹⁹ In this framework, the hydrogen atoms are not explicitly modeled but are lumped onto their connected carbon atom to make a pseudo, heavier CH₂ atom. The basis for this assumption is that the stiff, high frequency C-H bonds will not play a significant role in the thermal transport across the interface and also are not activated at a temperature of 300 K. For the interactions within the molecular chain, harmonic potentials were used for bond-stretching and bending and the Ryckaert-Bellemans potential¹²⁰ was implemented for four-body dihedral interactions. Lennard-Jones potentials and the Lorentz-Berthelot mixing rules were used for all non-bonded interactions.⁹⁵ A summary of the parameters used in the potentials can be found in the supplemental information of the study published by Ong *et al.*²⁴

3.1.2. Calculating the junction and interface thermal conductances

Since there are no clear boundaries of the junction and there is a strong non-linearity in the temperature profile near the Au-SAM interface (see Figure 3.3), we calculate the temperature drop using data from the regions where the profile is linear. On average, this region begins two temperature blocks (red squares – each corresponding to 270 Au atoms) away from the metal-SAM interfaces. Linear fits to five temperature blocks in the two leads were generated using a least-squares algorithm and the lines were extended to the metal-SAM interfaces, as shown in Figure 3.3. A linear fit was also made to the temperature blocks within the SAM, excluding two points on each end. Three separate temperature differences were calculated corresponding to (i) the Au-SAM interface conductance (G_{Au-SAM} , ΔT_1), (ii) the SAM-metal interface conductance

($G_{SAM-\alpha Au}$, ΔT_2) and (iii) the total junction thermal conductance (G_{total} , ΔT) as shown in Figure S5. The thermal conductance G_i was calculated from: $q'' = G_i \Delta T_i$. The left and right lead endpoint temperatures are calculated based on the three temperature blocks in the non-linear portion of the leads resulting in three values of thermal conductance for each G_i . The endpoint temperatures of the SAM are based on the fit. For example, as illustrated in Figure 3.3, ΔT_1 , ΔT_2 , and ΔT are calculated at the second temperature block of the lead away from each interface. Averaging over the three resulting thermal conductances for each G_i gives their means and uncertainties. Multiple simulations were performed for each case and the global mean and uncertainty were calculated using the procedure detailed in Section 2.3.2.

The molecules themselves (i.e., the SAM) have a finite thermal resistance indicating the presence of inelastic scattering events. Assuming the average thickness of the SAM layer to be $L = 1.5$ nm, we calculate its thermal conductivity from $q'' = -k \Delta T_{mol} / L$ where $\Delta T_{mol} = \Delta T - (\Delta T_1 + \Delta T_2)$. The SAM thermal resistance is small ($< 9\%$ of the total thermal resistance of the junction at a temperature of 300 K) when compared to the resistances at the interfaces. Even for the cases when the mean system temperature is 950 K or when the atomic masses of the carbon and sulphur atoms are 1000 times their standard values, the thermal resistance of the SAM does not exceed 20% of the total thermal resistance of the junction.

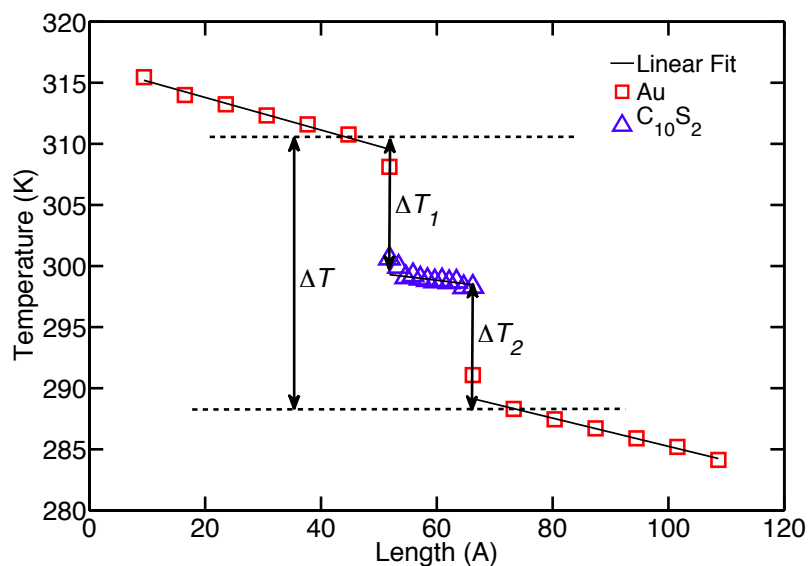


Figure 3.3. Temperature profile in the MD simulation cell.

3.1.3. *Cross-sectional area and length convergence*

A series of convergence tests were performed to find the appropriate cross-sectional area and length of the Au leads. The results are shown in Figure 3.4. The final chosen configuration has a cross sectional area of $24 \times 24 \text{ Å}^2$ and Au lead length of 56 Å . These choices correspond to 2160 atoms in each Au lead and 30 molecules in the SAM.

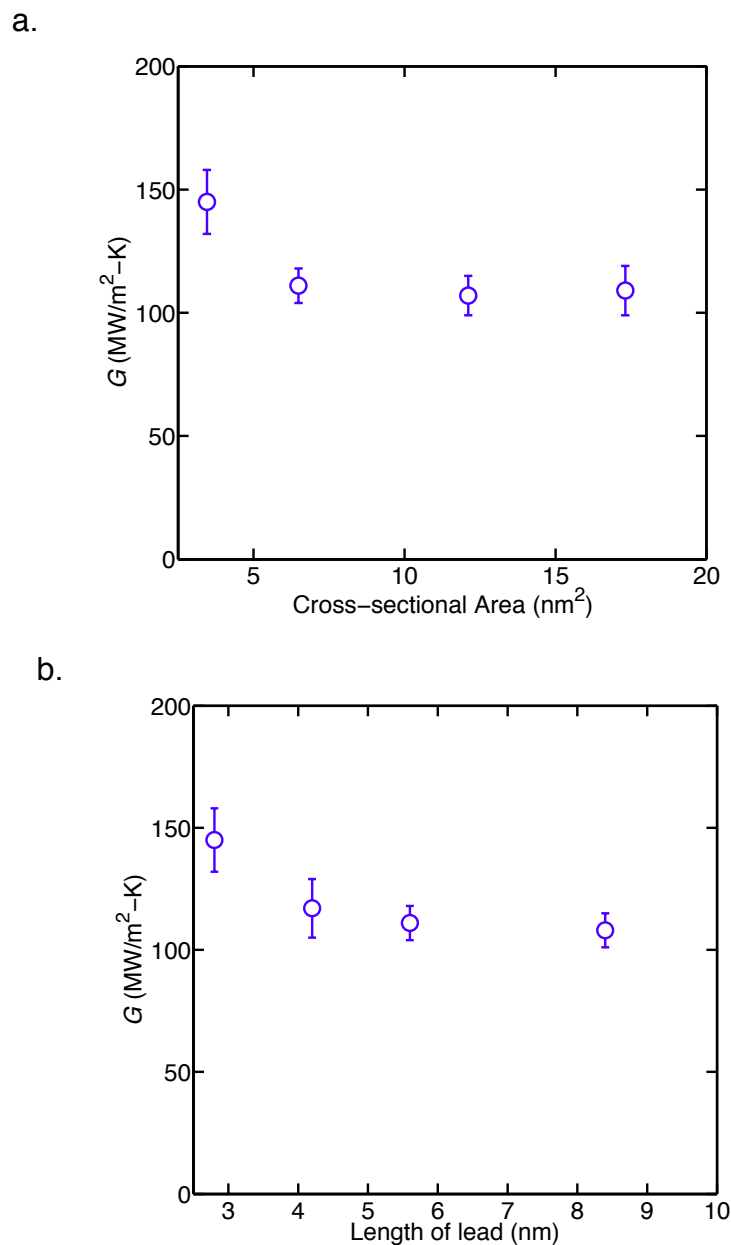


Figure 3.4. (a) Convergence analysis with cross-sectional area of Au leads. (b) Convergence analysis with length of Au leads.

Effect of temperature

The mean temperature of the simulation cell was changed to study the effect of anharmonic scattering (which is temperature-dependent) on the junction thermal conductance. The system (Au-decanedithiol-Au) was first equilibrated at the desired temperature in an *NVT* ensemble following which NEMD simulations were performed. The variation of junction

thermal conductance versus mean temperature of the system is plotted in Figure 3.5. The junction thermal conductance remains unchanged over the entire temperature range of 300 K – 950 K, indicating that elastic scattering dominates at the metal-SAM interfaces.

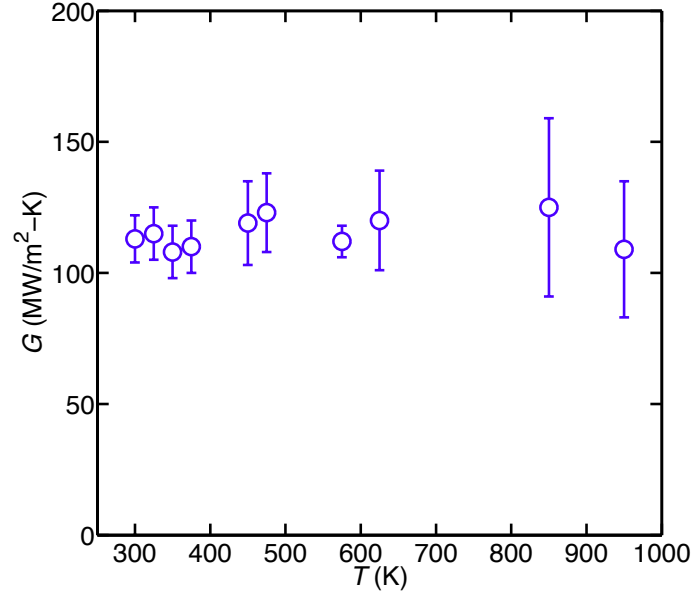


Figure 3.5. Effect of system mean temperature on the junction thermal conductance.

3.2. Vibrational mismatch effects using MD simulations

To model the effect of mismatched metal leads, we varied the atomic mass (m) of one lead. We assume that the main contribution to the vibrational properties is from the atomic mass of the lead. This approximation is reasonable because all of the metals in our experiments are face-centered cubic with similar lattice constants. If the ratio of the bottom lead atomic mass with respect to that of Au is $\alpha = m/m_{\text{Au}}$, its Debye temperature (T_D) can be set from:

$$\frac{T_D}{T_{D_{\text{Au}}}} = \alpha^{-1/2}. \quad (2.4)$$

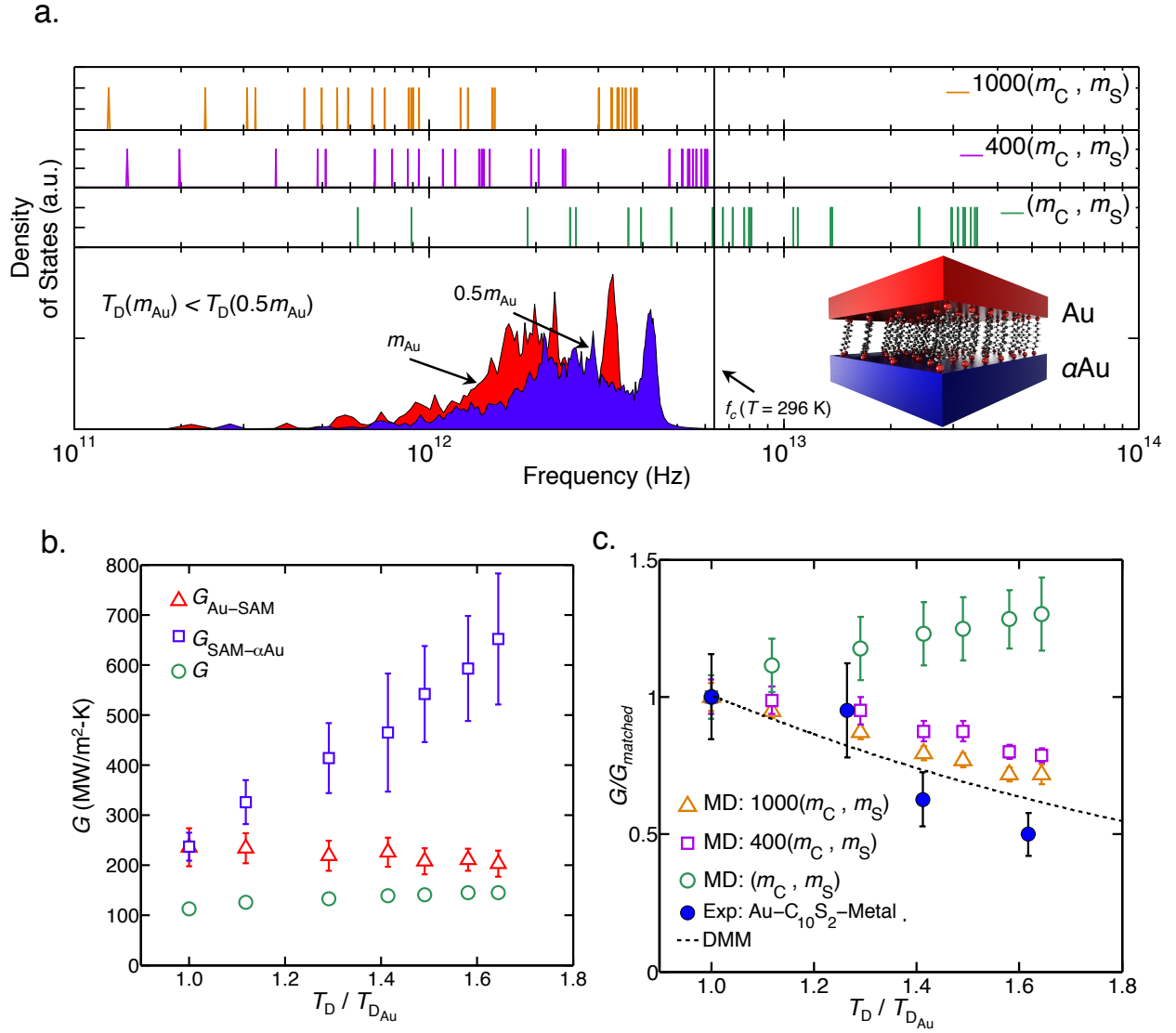


Figure 3.6. (a) DOS of the metal leads with atomic masses m_{Au} (red) and $0.5m_{\text{Au}}$ (blue), and 1,10-decanedithiol having carbon and sulphur atoms with atomic masses $(m_{\text{C}}, m_{\text{S}})$ (green), $(400m_{\text{C}}, 400m_{\text{S}})$ (purple) and $(1000m_{\text{C}}, 1000m_{\text{S}})$ (orange). (b) MD-predicted variation of the thermal conductance of the individual interfaces (blue square and red triangles) and the entire junction (green circles) with the Debye temperature ratio of the metal leads. (c) Variation of junction thermal conductance, normalized by the value of the matched lead case, with the Debye temperature ratio of the metal leads. The MD predictions (orange triangles, purple squares, and green circles) are compared to the experimental results (blue filled circle) and DMM calculations (dashed line).

Vibrational DOS calculations were performed using velocity autocorrelation data from MD simulations for the bulk leads and lattice dynamics calculations using GULP¹²¹ for the molecules. The predicted DOS for two leads whose atoms have masses of m_{Au} and $0.5m_{\text{Au}}$

(comparable to the atomic mass of Pd) are plotted in the bottom panel of Figure 3.6a. The discrete states of 1,10-decanedithiol molecule are plotted in the panel immediately above the lead DOS (in green).

The junction thermal conductance of such mismatched systems depends strongly on the nature of vibrational scattering at the individual metal-SAM interfaces. For an elastic scattering event, the frequencies of the reflected and/or transmitted energy carriers are the same as that of the incident energy carrier. For an inelastic (i.e., anharmonic) event, the scattered frequencies will be different. If only elastic scattering is present at the interfaces and the thermal transport in the SAM is ballistic, the metal lead having the DOS with the narrowest spectrum will dictate the highest frequency that can transmit energy across the entire junction and contribute to the junction thermal conductance. Vibrational modes with frequencies above this cutoff will be fully reflected from the interface. This scenario would imply that as the vibrational spectra of the two leads increase in mismatch, the junction thermal conductance would decrease because the number of overlapping vibrational modes between the SAM and the two leads would also decrease. This hypothesis is consistent with our experimental measurements, suggesting the dominance of elastic scattering at the interfaces.

The variation of the junction thermal conductance with the lead Debye temperature ratio ($T_D/T_{D_{Au}}$) from MD simulations is plotted in Figure 3.6b (green circles). In contrast to our experimental measurements, the junction thermal conductance increases by a factor of 1.3 as $T_D/T_{D_{Au}}$ increases. We also plot the metal-SAM interface thermal conductances on either side of the junction in Figure 3.6b. The thermal conductance of the interface whose Debye temperature is varied ($G_{SAM-aAu}$) increases as the Debye temperature increases, while the interface conductance at the Au lead (G_{Au-SAM}) remains constant. These observations contradict our experimental

measurements and suggest that overlap between the vibrational states at each interface in the MD simulations is independently realized.

3.3. Effects of the classical nature of MD

Why do the interfaces in our MD simulations act independently while those in the experiments appear not to? Noting that MD simulations obey classical (i.e. Boltzmann) statistics, all vibrational states are activated. From Figure 3.6a, we see that many vibrational states in the molecule have frequencies higher than the characteristic thermal frequency $f_c = k_B T / h$ (where k_B is the Boltzmann constant and h is the Planck constant), which is 6.2 THz at a temperature of 296 K. While active in the MD simulations, these modes are frozen out in the experiments. Furthermore, the maximum frequency for the lightest lead (Pd, $T_D = 275$ K) lies below this cutoff such that all the lead states are fully active for all the experimental systems.

We hypothesize that the classical nature of the MD simulations and inelastic scattering effects within the molecules themselves lead to predictions different from the experimental measurements. The atomic interactions in our MD simulations are anharmonic, which allows inelastic processes to occur within the molecules. Since all the vibrational states are active in the MD simulations, an anharmonic scattering event within the SAM involving three vibrational states could facilitate down-conversion of modes above the frequency cutoff of the heavier lead. In particular, one mode above the cutoff can scatter into two modes below the cutoff, creating additional channels for vibrational coupling across the junction. Such events cannot occur in the experiments since vibrational modes with characteristic temperatures above 296 K are not activated. Anharmonic events within the SAM would allow each metal lead to interact with the SAM independently, as seen in the MD results, therein opening pathways for thermal transport across the junction that are not present in the experiments.

To test this hypothesis, the vibrational spectrum of the SAM needs to be restricted to coincide with the activated spectrum in the experiments. As the classical nature of MD forces all available vibrational states to be activated, the states themselves need to be changed. To lower the molecular frequencies, the mass of the carbon and sulphur atoms are increased to 400 and 1000 times their actual values. The DOS for these modified molecules are plotted in the top panels of Figure 3.6a (purple and orange). The junction thermal conductance of the modified configurations is plotted in Figure 3.6c (purple squares and orange triangles) along with the original MD results and the molecular footprint-scaled experimental data (G_{scaled}). The data is normalized with respect to the junction thermal conductance of the matched lead case ($G_{matched}$) of each set. As the SAM molecules get heavier and their frequency spectrum is reduced, $G/G_{matched}$ decreases with increasing T_D/T_{DAu} and agrees with our experimental trend.

We also derive a modified form of the diffuse mismatch model (DMM) model used by Duda *et al.*,¹¹⁰ wherein the vibrational modes participating in thermal transport through the junction are limited by the lead with the narrowest DOS. The prediction of $G/G_{matched}$ using this model is plotted as a dashed line in Figure 3.6c and agrees with our experimental and modified MD trends.

3.4. Modified diffuse mismatch model

The thermal conductance at an interface between two semi-infinite solids in perfect epitaxial contact can be calculated using the Landauer formalism and a model for the transmission coefficients. This formalism assumes that the only resistance to thermal transport at the interface arises from the difference in vibrational properties of the two solids. Phonons are treated as particles that are incident on the interface, allowing us to calculate the heat current at

the interface using the properties of the bulk solids. For solids labeled 1 and 2, the phonon heat flux $q_{1 \rightarrow 2}$ from solid 1 (Au crystal) to solid 2 (SAM) can be written as:

$$q_{1 \rightarrow 2} = \frac{1}{8\pi^2} \sum_j \int_{k_j} \hbar \omega(k_j) k_j^2 \alpha_{1 \rightarrow 2} |v_j(k_j)| f(\omega) dk_j \quad (2.5)$$

Here, j is the polarization, k is the phonon wave number, ω is the phonon angular frequency, v is the phonon group velocity, f is the phonon population given by either Boltzmann or Bose-Einstein distribution, and $\alpha_{1 \rightarrow 2}$ is the transmission function for a phonon traveling from solid 1 to 2. The solid (Au) is assumed to be isotropic and the phonon dispersion along the [111] crystallographic direction is chosen to represent the entire Brillouin zone. Debye dispersion is assumed in order to simplify the calculation. Only the longitudinal branch is considered for which the group velocity for Au is taken as 3240 m/s.¹²²

The heat flux $q_{2 \rightarrow 1}$ above must be modified due to the discrete nature of the vibrational modes in the SAM:

$$q_{2 \rightarrow 1} = \frac{1}{AL} \sum_i \hbar \omega_i \alpha_{1 \rightarrow 2} f(\omega_i) v_m \quad (2.6)$$

Here, i is the index spanning all vibrational states in the molecule, A is the cross sectional area per molecule (equals footprint of 1,10-decanedithiol – 21.7 Å²/molecule), L is the length of the molecule (1.5 nm), and v_m is the speed of sound in the SAM (assumed to equal the speed of sound in polyethylene – 2300 m/s¹²³). For a very small temperature drop across the interface, the principle of detailed balance can be invoked by which $q_{1 \rightarrow 2} = q_{2 \rightarrow 1}$.

The transmission function α can be calculated using the diffuse mismatch model (DMM).¹²⁴ It assumes that phonons incident on the interface lose all memory of their previous

state and scatter diffusely upon impact such that $\alpha_{1\rightarrow 2} + \alpha_{2\rightarrow 1} = 1$. These assumptions lead to the following result for a single Au-SAM interface:

$$\alpha_{1\rightarrow 2} = \frac{\frac{1}{AL} \sum_i \hbar \omega_i f(\omega_i) v_m}{\frac{1}{8\pi^2} \sum_j \int_{k_j} \hbar \omega(k_j) k_j^2 |v_j(k_j)| f(\omega) dk_j + \frac{1}{AL} \sum_i \hbar \omega_i f(\omega_i) v_m} \quad (2.7)$$

In modeling an entire junction, an important point to note is that the integration and summation are only performed up to the maximum frequency of the heaviest lead, imposing a frequency cutoff for scattering events that phonons can undergo at both interfaces. All phonon modes with frequencies higher than this value will not transmit energy across the junction and have a zero transmission coefficient.

The findings in this chapter support our hypothesis that elastic scattering mechanisms dominate within the SAM junctions and at each metal-SAM interface in the experiments, therein explaining why vibrational mismatch of the leads reduces G .

4. Chapter 4: Morse potential-based model for contacting composite rough surfaces – Application to self-assembled monolayer junctions

4.1. Introduction

The Morse potential is more general than the LJ potential as it has three free parameters as compared to two free parameters in the LJ potential.¹²⁵ It is suitable for many systems, including molecules and metals.^{126,127} It has been essential for representing complex material interactions, such as adhesion of thin films on metal substrates [e.g., self-assembled monolayers (SAMs) on gold⁹⁸] and has been parameterized for both covalent and van der Waals interactions.^{128–133} Herein, we develop an adhesion-based contact model for interfaces by incorporating the Morse potential into the KE (and as a consequence the DMT) modeling framework. The resulting contact model can be employed for a wide variety of surface materials, from hard-soft interfaces to organic-inorganic heterojunctions.

We first derive expressions for the adhesive pressure and interaction energy per unit area between two macroscopic bodies where atomic interactions are described using the Morse potential in Sections 4.2.1, 4.2.2, and 4.2.3. We then incorporate these expressions into the KE model and calculate the total adhesive pressure between the rough bodies in Section 4.2.4. In Section 4.2.5, we present a method to calculate adhesive pressures where one or both bodies in contact are composed of layers of different materials. In Section 4.2.6, we describe the analytical model used to characterize the roughness parameters of a body. Lastly, we predict the percentage contact area (i.e., the ratio of the real area of contact to total surface area which appears to be in contact) between two rough gold surfaces where one is coated with a SAM in Section 4.3. These

predictions are validated using interface thermal conductance measurements described in Chapter 2.¹⁰⁰

4.2. Theory

4.2.1. Derivation of surface pressure using the Morse potential

The Morse (subscript M) potential between two point particles (atoms), separated by a distance r , is

$$E_{M,pp} = D_e [e^{-2\alpha(r-r_0)} - 2e^{-\alpha(r-r_0)}], \quad (4.1)$$

where the ‘ pp ’ subscript represents a particle-particle interaction. Here, D_e is the depth of the potential well, α describes the inverse of the width of the well, and r_0 is the position of the minimum of the well. The $2D_e e^{-\alpha(r-r_0)}$ term represents London dispersion (i.e., van der Waals) interactions, which are attractive, and the $D_e e^{-2\alpha(r-r_0)}$ term represents exchange repulsion. Repulsive energy is defined as positive and attractive energy as negative. The difference in behavior between the Morse potential and the LJ potential, given by $E_{LJ,pp} = 4\epsilon[(\sigma/r)^{12} - (\sigma/r)^6]$, where ϵ is the depth of the well and σ is interatomic distance at which $E_{LJ,pp} = 0$, is shown in Figure 4.1a. The parameters used in plotting the Morse potential describe the interaction between a thiol group (-SH group) and a gold atom.⁹⁸ The LJ potential is constructed to have the same position and depth of the well as the Morse potential, but ultimately exhibits a different energy landscape at other positions due to its mathematical formulation. All parameters for the potentials used in Figure 4.1a are listed in Table 4.1.

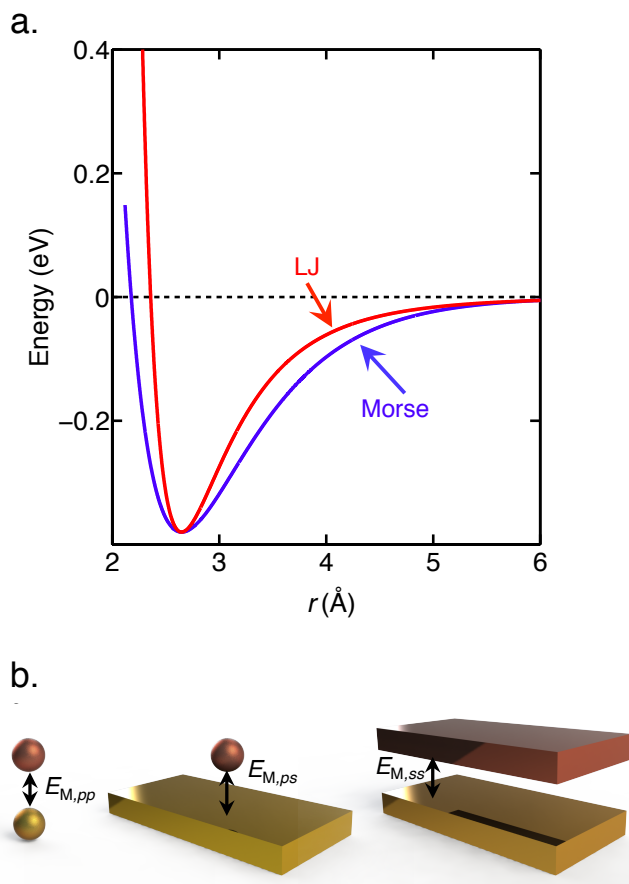


Figure 4.1. (a) Comparison of Morse and LJ potentials for the same energy well depth and equilibrium separation for a thiol-gold interaction.⁹⁸ (b) Schematic diagrams representing interactions between two point particles, one point particle and a flat, semi-infinite substrate, and two flat, semi-infinite substrates.

Table 4.1. Atomic interaction and surface topography parameters.

Morse Potential Parameters (S-Au) ^{98,100}	
D_e (Energy well depth)	0.38 eV
α (Measure of energy well width)	$1.67 \times 10^{-10} \text{ m}^{-1}$
r_0 (Position of energy well minimum)	$2.65 \times 10^{-10} \text{ m}$
LJ Potential Parameters	
	0.38 eV (S-Au)
ϵ (Energy well depth)	0.0029 eV (C-Au) ⁹⁵
	0.0017 eV (Au-Au) ⁹⁵

	$2.360 \times 10^{-10} \text{ m (S-Au)}$
σ (Position where energy is zero)	$3.424 \times 10^{-10} \text{ m (C-Au)}^{95}$
	$2.934 \times 10^{-10} \text{ m (Au-Au)}^{95}$
Surface Potential Parameters	
	$6.60 \times 10^{-1} \text{ J/m}^2 \text{ (Morse – S-Au)}$
$\Delta\gamma$ (Work of adhesion)	$1.35 \times 10^{-2} \text{ J/m}^2 \text{ (LJ – C-Au)}$
	$6.98 \times 10^{-3} \text{ J/m}^2 \text{ (LJ – Au-Au)}$
$\rho_{1,2}$ (Volumetric number density)	$5.89 \times 10^{28} \text{ m}^{-3} \text{ (Au)}$
	$3.85 \times 10^{28} \text{ m}^{-2} \text{ (C)}$
σ_2 (Areal number density)	$4.62 \times 10^{18} \text{ m}^{-2} \text{ (S)}$
	$1.90 \times 10^{-10} \text{ m (Morse – S-Au)}$
r_e (Equilibrium separation)	$3.17 \times 10^{-10} \text{ m (LJ – C-Au)}$
	$2.56 \times 10^{-10} \text{ m (LJ – Au-Au)}$
Material Properties (Au and SAM)	
E (Elastic modulus) ¹¹⁵	$4.712 \times 10^{10} \text{ N/m}^2$
ν (Poisson ration) ¹¹⁵	0.44
H (Hardness) ¹³⁴	210 MPa
Asperity Properties for Effective Rough Surface	
σ_h [Root mean-squared (RMS) roughness]	$6.30 \times 10^{-10} \text{ m}$
η (Areal asperity density)	$2.96 \times 10^{15} \text{ m}^{-2}$
R (Radius of asperity)	$6.98 \times 10^{-8} \text{ m}$
t_1 (Thickness of S layer)	$1.50 \times 10^{-10} \text{ m}$
t_2 (Thickness of C layer)	$13.5 \times 10^{-10} \text{ m}$
t_3 (Thickness of SAM)	$15 \times 10^{-10} \text{ m}$

To study the asperities that describe rough surfaces, this point-point potential must be extended to describe interactions between macroscopic bodies. Let us first consider the attractive

part of the pair potential given by $E_{M,pp}^a = -2D_e e^{-\alpha(r-r_0)}$. We assume additivity of these interactions, such that the net interaction between a single atom and a monatomic substrate is the sum of its interactions with all the atoms in the substrate.¹¹⁴ If we consider a substrate (semi-infinite solid) with a flat surface having a volumetric density of atoms ρ_1 at a distance D from an atom (the point particle), the attractive interaction energy will be

$$E_{M,ps}^a(D) = -\frac{4\pi\rho_1 D_e}{\alpha^3} (\alpha D + 2) e^{-\alpha(D-r_0)}, \quad (4.2)$$

where the subscript ‘*ps*’ denotes a particle-substrate interaction. A schematic diagram of this geometry is shown in Figure 4.1b. Following a similar procedure, the attractive interaction energy per unit area between two substrates, whose surfaces are separated by a distance D , is

$$E_{M,ss}^{a''}(D) = -\frac{4\pi\rho_1\rho_2 D_e}{\alpha^4} (\alpha D + 3) e^{-\alpha(D-r_0)}. \quad (4.3)$$

Here, ρ_2 is the volumetric density of atoms in the second substrate. If the second structure is instead a single layer of atoms (i.e., a surface, such as in a two-dimensional material) with an areal atomic density σ_2 , the attractive interaction energy per unit area is

$$E_{M,surf-s}^{a''}(D) = -\frac{4\pi\rho_1\sigma_2 D_e}{\alpha^3} (\alpha D + 2) e^{-\alpha(D-r_0)}, \quad (4.4)$$

where the subscript ‘*surf*’ denotes surface. The corresponding attractive forces per unit area are

$$F_{M,ss}^{a''}(D) = -\frac{dE_{M,ss}^{a''}}{dD} = P_{M,ss}^a = -\frac{4\pi\rho_1\rho_2 D_e}{\alpha^3} (\alpha D + 2) e^{-\alpha(D-r_0)}, \quad (4.5)$$

$$F_{M,surf-s}^{a''}(D) = P_{M,surf-s}^a = -\frac{4\pi\rho_1\sigma_2 D_e}{\alpha^2} (\alpha D + 1) e^{-\alpha(D-r_0)}. \quad (4.6)$$

where $P_{M,ss}^a$ and $P_{M,surf-s}^a$ are the attractive pressures.

Until now, we have only considered the attractive interaction. To realize a potential with an equilibrium separation, we need to add the repulsive interaction. Following the procedure of

Eqs. (4.2)-(4.6), we obtain the general form of the repulsive interaction for either the substrate-substrate or surface-substrate configurations to be $P_M^r = A_1(\alpha D + A_2)e^{-2\alpha(D-r_0)}$ and the subsequent total adhesive pressure is $P_M = P_M^r + P_M^a$. To determine the unknown coefficients A_1 and A_2 , we first enforce the physical limit that when the distance between the surfaces of the two bodies equals their equilibrium separation r_e , zero pressure (i.e., zero force) is felt by them, i.e. $P_M(r_e) = 0$. We note that r_e does not equal r_0 . This assumption maintains a continuity of the physical picture of atomic-scale interactions when moving from the atomic to the macro-scale and was employed in the derivation of the DMT model using the LJ potential.^{75,114,135} We can then solve for A_1 in terms of A_2 for the substrate-substrate and surface-substrate cases as

$$A_{1,ss} = \frac{4\pi\rho_1\rho_2 D_e}{\alpha^3} \left(\frac{\alpha r_e + 2}{\alpha r_e + A_{2,ss}} \right) e^{\alpha(r_e - r_0)} \quad (4.7)$$

$$A_{1,surf-s} = \frac{4\pi\rho_1\sigma_2 D_e}{\alpha^2} \left(\frac{\alpha r_e + 1}{\alpha r_e + A_{2,surf-s}} \right) e^{\alpha(r_e - r_0)}. \quad (4.8)$$

The physical constraint of $P_M(D \rightarrow \infty) = 0$ is naturally satisfied by the form of the Morse potential. There are no more physical constraints that can be imposed to specify the coefficient A_2 .

Table 4.2. Coefficients in the expressions for pressure [Eq. (4.9)], energy per unit area [Eq. (4.10)], and work of adhesion [Eq. (4.11)] derived for the interaction between two substrates (*ss*), and a surface with a substrate (*surf-s*) described by a Morse potential.

	B_1	B_2	B_3
$P_{M,ss}$	$\frac{\rho_2}{\alpha}$	$\frac{(\alpha D + A_{2,ss})(\alpha r_e + 2)}{(\alpha r_e + A_{2,ss})}$	$\alpha D + 2$
$P_M(D)$			
$P_{M,surf-s}$	σ_2	$\frac{(\alpha D + A_{2,surf-s})(\alpha r_e + 1)}{(\alpha r_e + A_{2,surf-s})}$	$\alpha D + 1$

$E_M''(D)$	$E_{M,ss}''$	$\frac{\rho_2}{\alpha}$	$\frac{(\alpha r_e + 2)(2\alpha D + 2A_{2,ss} + 1)}{4(\alpha r_e + A_{2,ss})}$	$\alpha D + 3$
	$E_{M,surf-s}''$	σ_2	$\frac{(\alpha r_e + 1)(2\alpha D + 2A_{2,surf-s} + 1)}{4(\alpha r_e + A_{2,surf-s})}$	$\alpha D + 2$
$\Delta\gamma_M$	$\Delta\gamma_{M,ss}$	$\frac{\rho_2}{\alpha}$	$\frac{(\alpha r_e + 2)(2\alpha r_e + 2A_{2,ss} + 1)}{4(\alpha r_e + A_{2,ss})}$	$\alpha r_e + 3$
	$\Delta\gamma_{M,surf-s}$	σ_2	$\frac{(\alpha r_e + 1)(2\alpha r_e + 2A_{2,surf-s} + 1)}{4(\alpha r_e + A_{2,surf-s})}$	$\alpha r_e + 2$

We generalize the expression for P_M by grouping parameters into the coefficients B_1 , B_2 , and B_3 (defined in Table 4.2), leading to

$$P_M(D) = \left(\frac{4\pi\rho_1 D_e}{\alpha^2} \right) B_{1,P_M} [B_{2,P_M} e^{\alpha(r_e - r_0)} e^{-2\alpha(D - r_0)} - B_{3,P_M} e^{-\alpha(D - r_0)}], \quad (4.9)$$

where the corresponding interaction energy per unit area is

$$E_M''(D) = \left(\frac{4\pi\rho_1 D_e}{\alpha^3} \right) B_{1,E_M''} [B_{2,E_M''} e^{\alpha(r_e - r_0)} e^{-2\alpha(D - r_0)} - B_{3,E_M''} e^{-\alpha(D - r_0)}]. \quad (4.10)$$

For hemispherical asperities, a common form for expressing the energy and pressure equations is through the work of adhesion $\Delta\gamma$, which represents the magnitude of E_M'' at its minimum value (i.e., at $D = r_e$) and is

$$\Delta\gamma_M = |E_M''(D = r_e)| = \left| \left(\frac{4\pi\rho_1 D_e}{\alpha^3} \right) B_{1,\Delta\gamma_M} e^{-\alpha(r_e - r_0)} (B_{2,\Delta\gamma_M} - B_{3,\Delta\gamma_M}) \right|. \quad (4.11)$$

We note that evaluation of Eqs. (4.9)-(4.11) requires specification of r_e and A_2 . All other parameters are based on the Morse potential parameters and the crystal structures of the bodies under consideration and thus, known *a priori*.

We evaluate r_e and A_2 using single-point energy calculations. We first place a single layer of atoms above a substrate of another kind of atoms. A schematic diagram of this structure is shown in Figure 4.2a. The substrate is an fcc solid having a (111) surface with a lattice constant

of 4.08 Å (i.e., that of gold). The surface is a close-packed structure having a nearest neighbor distance of 4.997 Å (i.e., that of a thiol-based SAM).^{32,95,100} Our calculations correspond to the case where the atoms of the single-layer surface are directly above the three-fold hollow sites of the surface of the substrate. Only the interaction potential (Morse or LJ) between the layer and the substrate is considered while calculating the energy of the system at different separations.

The variation of the interaction energy between the surface and the substrate (non-dimensionalized by $\Delta\gamma_{\text{LJ}}$) as a function of the separation distance between them is plotted in Figure 4.2b for both Morse (blue circles) and LJ (red squares) potentials, corresponding to a thiol-gold interaction whose parameters are listed in Table 4.1. The magnitude of the interaction energy at its minimum value is $\Delta\gamma$ and the corresponding separation distance is r_e . We can thus find the ratio $\Delta\gamma_{\text{M}}/\Delta\gamma_{\text{LJ}}$ from this calculation, as shown in Figure 4.2b. We take this approach because exact analytical expressions for $\Delta\gamma$ exist for an LJ potential and are⁷⁵

$$\Delta\gamma_{\text{LJ},ss} = \frac{\pi\rho_1\rho_2(4D_e\sigma^6)}{16r_e^2}$$

$$\Delta\gamma_{\text{LJ},surf-s} = \frac{\pi\rho_1\sigma_2(4D_e\sigma^6)}{9r_e^3}.$$
(4.12)

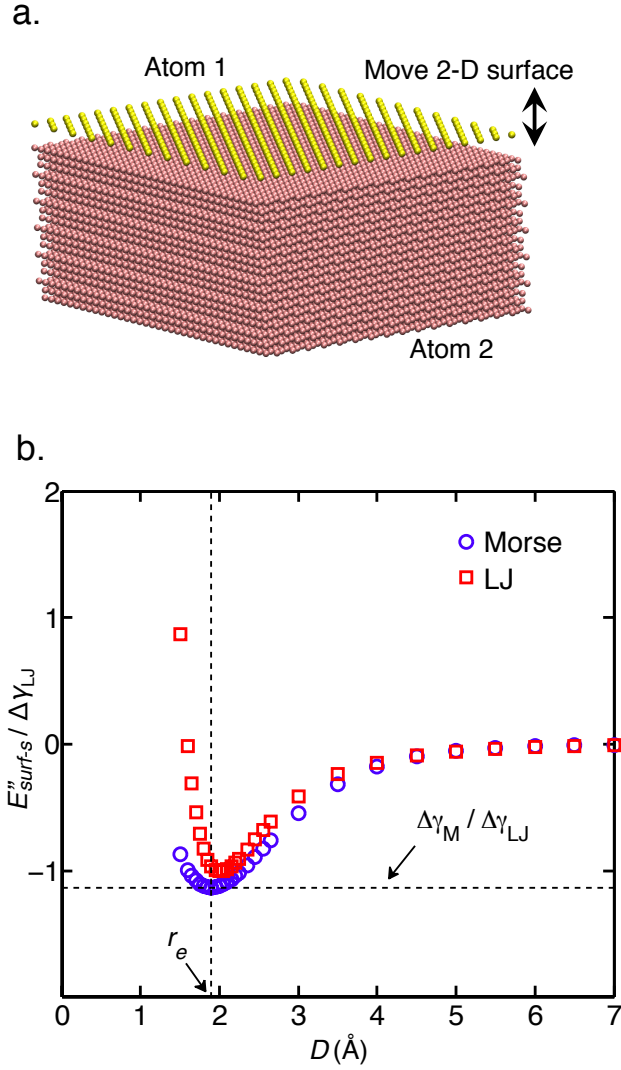


Figure 4.2. (a) Schematic diagram of the structure for single-point energy calculations between a two-dimensional surface of atom type 1 (yellow) placed at different heights above a substrate of atom type 2 (pink). (b) Interaction energy, non-dimensionalized by $\Delta\gamma_{LJ}$, using both Morse (red squares) and LJ (blue circles) potentials for a thiol-gold interaction (parameters in Table 4.1) plotted as a function of separation distance D between the surface and substrate. The magnitude of the interaction energy at its minimum value (where $D = r_e$) is equal to $\Delta\gamma$.

Once $\Delta\gamma_M$ is calculated using the results of the single-point energy calculations and Eq. (4.12), we can analytically determine A_2 from Eq. (4.11). We note, however, that these calculations are specific to our system, with A_2 equal to -4.9138 and $\Delta\gamma_M$ equal to 0.66 J/m². To

allow the implementation of this model to other surface-substrate systems, we provide generalized expressions describing the variation of r_e/r_{NN} and $\Delta\gamma_M/\Delta\gamma_{LJ}$ as a function of the parameters αr_{NN} and r_0/r_{NN} (r_{NN} being the nearest neighbor distance between atoms in the substrate) in Appendix 8.1

The expressions for adhesive pressure and energy per unit area based on the Morse potential, represented by Eqs. (4.9)-(4.11), can now be used with the DMT and KE models to estimate the total adhesive force for hemispherical asperities contacting a flat substrate.

4.2.2. *Single asperity deformation*

The DMT model provides a method to calculate the adhesive force for a deformed hemisphere contacting a flat, undeformable surface. The method to calculate the deformed sphere profile is summarized in this section.⁷² The hemisphere is assumed to obey Hertzian theory and to deform elastically. The height Z of any point on the surface of the hemisphere at a radial distance x from the asperity center, following the DMT convention, is

$$Z(a, x, R) = \frac{1}{\pi R} \left[a(x^2 - a^2)^{1/2} - (2a^2 - x^2) \tan^{-1} \left(\sqrt{\frac{x^2}{a^2} - 1} \right) \right], \quad (4.13)$$

where R is the radius of the hemisphere and a is the radius of the contact region. A schematic diagram of this setup is shown in Figure 4.3a.

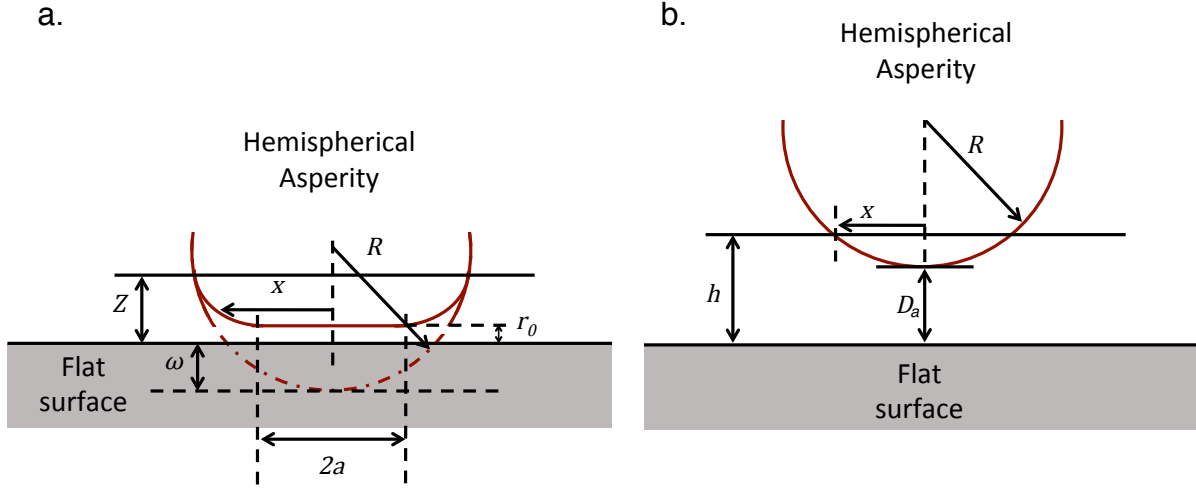


Figure 4.3. (a) Schematic diagram of a hemispherical asperity in contact with a flat surface and undergoing deformation. The flat surface is assumed to be rigid. (b) Schematic diagram of a hemispherical asperity at a height D_a above a flat surface.

The expression for Z can also be written in terms of the interference ω , which is the centerline deflection of the asperity, i.e., the maximum deformation of the compressed asperity.¹³⁶ It can be seen that $Z = 0$ when $x = a$. Eq. (13) was, however, developed for macro-scale deformations. When molecular potentials are taken into account, it is physically impossible for two atoms, or in this case two bodies, to have a separation distance of zero. Thus, Eq. (4.13) is adjusted such that the minimum value of Z equals the equilibrium separation between the surfaces r_e (derived in Section 4.2.1) and is further simplified by substituting the Hertzian relation for the contact radius

$$a = (\omega R)^{1/2}, \quad (4.14)$$

thus arriving at

$$Z(\omega, \bar{x}) = \frac{\omega}{\pi} \left[(\bar{x}^2 - 1)^{1/2} - (2 - \bar{x}^2) \tan^{-1} \left(\sqrt{\bar{x}^2 - 1} \right) \right] + r_e, \quad (4.15)$$

where $\bar{x} = x/a$. Eq. (4.15) is valid for elastic deformations, but it has been shown that the elastic deformation assumption is not adequate for most scenarios since plastic deformation occurs.⁷⁹ In

order to account for both elastic and plastic deformation, we follow the approach taken by Kogut and Etsion,⁸² where Z is further non-dimensionalized with respect to the critical interference ω_c , which is the interference at which plasticity begins (details in Appendix 8.2). Thus, the separation Z in the elastic regime, from Eq. (4.15), can be expressed as

$$\frac{Z(\omega, \bar{x})}{\omega_c} = \frac{1}{\pi} \frac{\omega}{\omega_c} f(\bar{x}) + \frac{r_e}{\omega_c} \quad \text{for } 0 \leq \omega/\omega_c \leq 1, \quad (4.16)$$

where $f(\bar{x}) = (\bar{x}^2 - 1)^{1/2} - (2 - \bar{x}^2)\tan^{-1}(\sqrt{\bar{x}^2 - 1})$. This non-dimensionalization allows for the study of the Hertzian profile independent of material properties. For the deformation regimes where $\omega/\omega_c \geq 1$ (elastic-plastic regimes), we use the FEA derived dimensionless separations found by Kogut and Etsion^{81,82}

$$\frac{Z(\omega, \bar{x})}{\omega_c} = \frac{0.951}{\pi} \left(\frac{\omega}{\omega_c}\right)^{1.153} f(\bar{x}) + \frac{r_e}{\omega_c} \quad \text{for } 1 \leq \omega/\omega_c \leq 6, \quad (4.17)$$

and

$$\frac{Z(\omega, \bar{x})}{\omega_c} = \frac{0.457}{\pi} \left(\frac{\omega}{\omega_c}\right)^{1.578} f(\bar{x}) + \frac{r_e}{\omega_c} \quad \text{for } 6 \leq \omega/\omega_c \leq 110. \quad (4.18)$$

Table 4.3. Range of contact regimes.

Regime	Dimensionless Separation
Non-Contact	$\omega/\omega_c \leq 0$
Elastic	$0 \leq \omega/\omega_c \leq 1$
Elastic-Plastic I	$1 \leq \omega/\omega_c \leq 6$
Elastic-Plastic II	$6 \leq \omega/\omega_c \leq 110$
Plastic	$\omega/\omega_c \geq 110$

Kogut and Etsion validated Eqs. (4.17) and (4.18) for a range of values of the plasticity index ψ , which Greenwood and Williamson showed to be directly related to the critical

interference as $\psi \propto \omega_c^{-0.5}$.⁶² We specifically note that the interference ω of the contacting asperities must fall within the range of 0 to $110\omega_c$ in order for the FEA data used to be accurate. The various deformation regimes used in this study are listed in Table 4.3.

4.2.3. Morse potential-based adhesion model based on asperity deformation

We now derive expressions for the adhesive pressure between a single hemispherical asperity and a substrate interacting through a Morse potential. The asperity may be a solid structure (having a volumetric density of atoms ρ_1) or hollow and composed of a single layer of atoms on its surface (having an areal density of atoms σ_2). Derjaguin *et al.* found the adhesive force between atoms in a slice along the surface of the hemisphere (i.e. a ring with radius x and thickness dx) and the flat surface to be⁷²

$$dF_c^{ad} = 2\pi x P_M(Z) dx. \quad (4.19)$$

It is important to note that the pressure $P_M(Z)$ contains the effect of all the atoms behind the exposed surface (if any). Thus, if we integrate Eq. (4.19) for all x , we get the total adhesive force between a deformed hemispherical asperity and a substrate to be

$$F_c^{ad} = 2\pi \int_a^\infty x P_M(Z) dx. \quad (4.20)$$

Strictly speaking, the upper limit of the integral should be the hemispherical radius R , but it can be approximated as infinity without significant error if $P_{M,ss}(Z) \rightarrow 0$ at separations much smaller than R , as is the case here.⁷² Now, from Eq. (4.20), we define $F_c^{ad}(a=0) = F_0^{ad} = 2\pi R \Delta\gamma$ as the point contact adhesive force. We use F_0^{ad} to normalize the total contact adhesive force in the same manner as Kogut and Etsion by changing the integrating variable to $\bar{x} = x/a$ and then dividing throughout by F_0^{ad} .⁸² The variables ω, α, r_0 , and r_e are also non-

dimensionalized using ω_c . The normalized force of adhesion for an asperity in contact (in any deformation regime), with respect to the point contact adhesive force, is found from Eq. (4.20) using the expression for P_M from Eq. (4.9). A general form of this expression is

$$\frac{F_c^{ad}(\omega)}{F_0^{ad}} = G_{1,F^{ad}} \int_1^\infty \left[G_{2,F_c^{ad}} e^{\alpha(r_e-r_0)} e^{-2(\alpha\omega_c)\left(\frac{Z}{\omega_c}-\frac{r_0}{\omega_c}\right)} - G_{3,F_c^{ad}} e^{-(\alpha\omega_c)\left(\frac{Z}{\omega_c}-\frac{r_0}{\omega_c}\right)} \right] \bar{x} d\bar{x}, \quad (4.21)$$

where the coefficients G_1 , G_2 , and G_3 for the substrate-substrate and surface-substrate cases are listed in Table 4.4. For any deformation regime, the corresponding separation Z [Eqs. (4.16)-(4.18)] can be used in Eq. (4.21).

In the case of a hemispherical asperity not in contact with the surface, the adhesive force from the DMT model is

$$F_{nc}^{ad} = 2\pi R \int_{D_a}^\infty P_M(h) dh, \quad (4.22)$$

where h is the separation between a slice of thickness dh within the asperity and the flat surface, and D_a is the minimum separation between the asperity and flat surface, as shown in Figure 4.3b. Using the expression for P_M from Eq. (4.9) and normalizing with F_0^{ad} , we derive the non-contact adhesive force to be

$$\begin{aligned} \frac{F_{nc}^{ad}(D_a)}{F_0^{ad}} = G_{1,F_{nc}^{ad}} & \left[G_{2,F_{nc}^{ad}} e^{\alpha(r_e-r_0)} e^{-2(\alpha\omega_c)\left(\frac{D_a}{\omega_c}-\frac{r_0}{\omega_c}\right)} \right. \\ & \left. - G_{3,F_{nc}^{ad}} e^{-(\alpha\omega_c)\left(\frac{D_a}{\omega_c}-\frac{r_0}{\omega_c}\right)} \right], \end{aligned} \quad (4.23)$$

where the coefficients G_1 , G_2 , and G_3 for the substrate-substrate and surface-substrate cases are listed in Table 4.4.

Table 4.4. Coefficients in the expressions for contact [Eq. (4.21)] and non-contact [Eq. (4.23)] adhesive pressures derived for the interaction between two substrates (ss) and a surface with substrate (surf-s) described by a Morse potential. The coefficients B_2 and B_3 are listed in Table II.

	G_1	G_2	G_3	
$\frac{F_c^{ad}(\omega)}{F_0^{ad}}$	$\frac{F_{c,ss}^{ad}(\omega)}{F_0^{ad}}$	$\frac{(\alpha\omega) e^{\alpha(r_e-r_0)}}{B_{2,\Delta\gamma_{M,ss}} - B_{3,\Delta\gamma_{M,ss}}}$	$\frac{(\alpha r_e + 2) \left[(\alpha\omega_c) \left(\frac{Z}{\omega_c} \right) + A_{2,ss} \right]}{(\alpha r_e + A_{2,ss})}$	$(\alpha\omega_c) \left(\frac{Z}{\omega_c} \right) + 2$
$\frac{F_0^{ad}}{F_{c,surf-s}^{ad}(\omega)}$	$\frac{F_{c,surf-s}^{ad}(\omega)}{F_0^{ad}}$	$\frac{(\alpha\omega) e^{\alpha(r_e-r_0)}}{B_{2,\Delta\gamma_{M,surf-s}} - B_{3,\Delta\gamma_{M,surf-s}}}$	$\frac{(\alpha r_e + 1) \left[(\alpha\omega_c) \left(\frac{Z}{\omega_c} \right) + A_{2,surf-s} \right]}{(\alpha r_e + A_{2,surf-s})}$	$(\alpha\omega_c) \left(\frac{Z}{\omega_c} \right) + 1$
$\frac{F_{nc}^{ad}(D)}{F_0^{ad}}$	$\frac{F_{nc,ss}^{ad}(D)}{F_0^{ad}}$	$\frac{1}{B_{2,\Delta\gamma_{M,ss}} - B_{3,\Delta\gamma_{M,ss}}}$	$\frac{(\alpha r_e + 2) \left[2(\alpha\omega_c) \left(\frac{D}{\omega_c} \right) + 2A_{2,ss} + 1 \right]}{4(\alpha r_e + A_{2,ss})}$	$(\alpha\omega_c) \left(\frac{D}{\omega_c} \right) + 3$
$\frac{F_0^{ad}}{F_{nc,surf-s}^{ad}(D)}$	$\frac{F_{nc,surf-s}^{ad}(D)}{F_0^{ad}}$	$\frac{1}{B_{2,\Delta\gamma_{M,surf-s}} - B_{3,\Delta\gamma_{M,surf-s}}}$	$\frac{(\alpha r_e + 1) \left[2(\alpha\omega_c) \left(\frac{D}{\omega_c} \right) + 2A_{2,surf-s} + 1 \right]}{4(\alpha r_e + A_{2,surf-s})}$	$(\alpha\omega_c) \left(\frac{D}{\omega_c} \right) + 2$

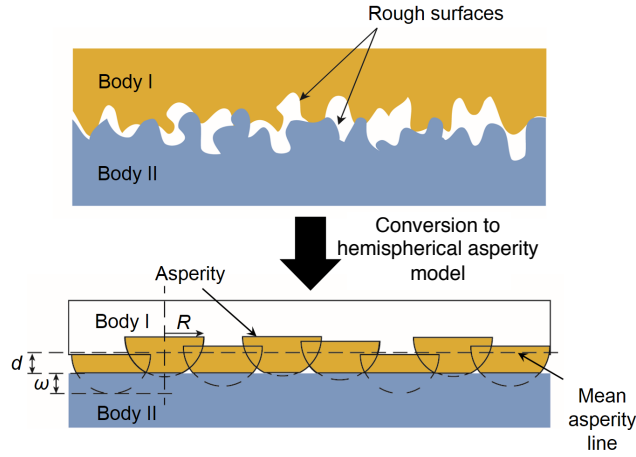


Figure 4.4. Conversion of two real surfaces to a statistical representation. The real surfaces are mapped to a flat surface in contact with a rough surface comprised of hemispherical asperities of radii R , which follow a statistical distribution [Eq. (25)], allowing for the height of each asperity to vary about the mean line.

4.2.4. Extension to two-body contact problem

Until now, we have derived expressions for the adhesive interaction of a single asperity with a substrate. To model the interaction between two real bodies, we analyze the interaction of a number of asperities (representing the rough surface of one body) with a substrate. The two-

body contact problem can be visualized as shown in Figure 4.4. A balance between any externally applied force, the adhesive force, and the contact force must exist for the bodies to be in equilibrium. In this section we present the equations necessary to calculate each of these forces and the percentage contact area for the two-body system. In order to simplify the problem, the two bodies with rough surfaces are transformed into an equivalent system of one rough body (Body I) in contact with a smooth, rigid body (Body II). The geometrical properties of Body I are equal to the sum of the geometrical properties of the original two rough bodies. The elastic modulus of Body I is calculated using Eqn. (B3). The surface of Body I is represented in a statistical manner as a distribution of hemispherical asperities of uniform radii R with heights varying based on a specified probability distribution $\phi(z)$. The total non-dimensional adhesive force F^{ad*} between the asperities and the surface is calculated as the sum of all the adhesive forces (i.e. contact and non-contact) weighted by the distribution of asperity heights for all of the deformation regimes. Thus, using Eqs. (4.21) and (4.23), we arrive at

$$F^{ad*} = \frac{F^{ad}}{A_n H} = \frac{2\pi\eta R \Delta\gamma}{H} \left(\int_{-\infty}^{d^*} \frac{F_{nc}^{ad}(d^* - z^* + r_e^*)}{F_0^{ad}} \phi^*(z^*) dz^* + \int_{d^*}^{d^* + 110\omega_c^*} \frac{F_c^{ad}(z^* - d^*)}{F_0^{ad}} \phi^*(z^*) dz^* \right), \quad (4.24)$$

where η is the areal density of asperities. Here, any variable with the superscript $*$, except for F^{ad} , is dimensionless and is normalized using the standard deviation of surface heights, σ_h . F^{ad} is normalized by the nominal contact area A_n and the hardness H . d^* represents the non-dimensional separation between the flat surface and the mean-line of asperity heights. The distribution ϕ has each of its variables normalized by σ_h . For a normal distribution of asperity heights,⁸¹

$$\phi^*(z^*) = \frac{\sigma_h}{\sqrt{2\pi}\sigma_s} e^{-\frac{1}{2}\left(\frac{\sigma_h}{\sigma_s}\right)^2 (z^*)^2}. \quad (4.25)$$

Alternatively, a deterministic approach could be used to calculate the percentage contact area and the mean separation between our two surfaces.^{136–143} In addition to the complexity of numerically solving the elastic and plastic constitutive equations for deformation, such an approach would require an iterative optimization method in order to calculate the balance between the adhesive and contact stresses. While such a deterministic approach may shed additional insight, we believe that a statistical model better represents our system due to its isotropic nature and Angstrom-scale RMS roughness of the surface (Table 4.1). The measurements of Majumdar *et al.*¹⁰⁰ were also statistically averaged representations of the thermal conductance values. The potential difference between statistical and deterministic models is thus left for future study.

4.2.5. Composite asperity model for modeling layered structures

We now extend our formulation to model adhesion between two surfaces where one of them has a thin film grown on it. The thin film is treated as an incompressible coating that follows the deformation behavior of the underlying substrate, such as in the case of an organic SAM grown on a metal or dielectric substrate.¹⁴⁴ Modeling the surface topography of such a system requires the asperities to be composed of multiple materials in a layered configuration, thus creating a composite asperity. Assuming substrate effects dominate, all materials of the composite asperity are assumed to have the same elastic modulus, Poisson ratio, and hardness, while having independent Morse (or LJ) parameters, layer thicknesses, and distances from the flat surface.

The contribution of each layer in the composite asperity to the adhesive pressure is incorporated by adjusting its distance from the flat surface. For example, considering only elastic deformations, each slice within the asperity will now have a height Z from the surface [derived from Eq. (4.16)] given by

$$\frac{Z(\omega, \bar{r})}{\omega_c} = \frac{1}{\pi} \frac{\omega}{\omega_c} f(\bar{r}) + \frac{r_e}{\omega_c} + \frac{t}{\omega_c} \quad \text{for } 0 \leq \omega/\omega_c \leq 1, \quad (4.26)$$

where t is the minimum separation of a hemisphere composed of one kind of atoms within the composite asperity and the surface of the asperity. Similar adjustments are made for the elastic-plastic deformation regimes [Eqs. (8.3.1) and (8.3.2)]. The remaining calculations are the same as given by Eqs. (4.19)-(4.25). The contribution of each material layer to the adhesive pressure is modeled by subtracting the adhesive pressure of a smaller hemisphere from the adhesive pressure of the larger hemisphere, thus creating the hemispherical layer.

4.2.6. *Characterization of an experimental surface*

A rough surface can be geometrically modeled as being composed of multiple hemispherical asperities arranged with an areal density η . The asperities have a mean radius R with a standard deviation of asperity heights σ_s , which is mathematically correlated to the standard deviation of surface heights σ_h .⁸¹ How these quantities can be obtained from atomic force microscopy (AFM) measurements has been studied in detail by Bush *et al.*,¹⁴⁵ Gibson,¹⁴⁶ and McCool.¹⁴⁷ The quantities η , R , and σ_s were originally derived by Nayak,¹⁴⁸ who built upon the work of Longuet-Higgins.¹⁴⁹ Nayak found that for random and isotropic surfaces having a Gaussian distribution of surface heights, a surface could be completely characterized by its spectral moments corresponding to height, slope, and curvature. Kotwal and Bhushan¹⁵⁰ studied non-Gaussian surfaces with kurtosis and skew but such an analysis is extremely complex and

beyond the scope of this study. More recent work has focused on the fractal-like behavior of surfaces and addressed variations with AFM scan parameters.^{139,151,152}

As opposed to surfaces explored in multi-scale studies,¹⁵³ the sputtered thin-film surface discussed in Section 4.3 does not exhibit any trend in the roughness parameters between different AFM scans. Instead, random variations in σ_h , R , and η are found between scans. Poon and Bhushan¹⁵⁴ also found that AFM surfaces do not follow a trend in roughness properties with scan size. We speculate that the dominant cause of our variations is related to the surface manufacturing process. Furthermore, given the Angstrom-scale roughness of our surfaces, we do not believe that it is meaningful to consider them from a fractal perspective. We thus follow McCool's approach to characterize the surface topography.¹⁴⁷ From metrology data (i.e., AFM images) of a given surface, the parameters η , R , σ_h , and σ_s can be calculated from

$$\eta = \frac{\langle (d^2\xi/d^2x)^2 \rangle / \langle (d\xi/dx)^2 \rangle}{6\pi\sqrt{3}}, \quad (4.27)$$

$$R = \frac{3\sqrt{\pi}}{8 \langle (d^2\xi/d^2x)^2 \rangle^{1/2}}, \quad (4.28)$$

$$\sigma_h = \langle \xi^2 \rangle^{1/2}, \quad (4.29)$$

and

$$\sigma_s = \sigma_h \left(1 - \frac{0.0003717}{(\eta R \sigma_h)^2} \right)^{1/2}, \quad (4.30)$$

where ξ is the measured height (above the mean-line) and the operator $\langle \rangle$ denotes a spatial arithmetic average. The derivatives are calculated along a set of straight lines parallel to the

horizontal axis of an AFM scan. The derivatives are numerically calculated using central difference schemes (providing second-order error with respect to grid spacing). The derivatives are only calculated for the interior points, i.e., the edge points are not considered.

4.3. Results

4.3.1. *Parameters of AFM measurements*

The AFM scans were taken with a Park Xe-70 AFM. We use scans having resolutions of 1024×1024 , 512×512 , and 256×256 pixels. Each resolution was used for scan areas of 10×10 , 7.5×7.5 , 5×5 , and $2.5 \times 2.5 \mu\text{m}^2$ (for those combinations where the AFM tip size is larger than the size of a pixel). The data presented in Figure 4.5c and Table 4.1 in the manuscript were obtained from the $7.5 \times 7.5 \mu\text{m}^2$ measurement and 1024×1024 pixel resolution. The deviation in the root mean-squared (RMS) roughness is within 1 Å across all sizes and resolutions. The individual parameters of RMS surface roughness (σ_h), radius of asperity (R), and areal asperity density (η) are listed (in order) below in Table 4.5 for the different values of scan sizes and resolutions.

The values of σ_h and R used in the model should be 2.0 and 0.5 times their values listed in Table 4.5 since we consider an equivalent rough surface having the surface heights equal to twice the measured AFM heights, which is in contact with a perfectly smooth surface. It is assumed that the templated Au substrate (having the self-assembled monolayer) and the transfer-printed Au substrate have comparable roughnesses since they were both originally grown on similar Si wafers.

Table 4.5. Parameters of RMS surface roughness (σ_h), radius of asperity (R), and areal asperity density (η) for all AFM measurements of a template Au surface.

	Resolution (pixels×pixels)			
		256×256	512×512	1024×1024
Scan size (μm)	2.5	3.12×10 ⁻¹⁰ m, 0.20×10 ⁻⁶ m, 2.41×10 ¹⁵ m ²	3.28×10 ⁻¹⁰ m, 0.06×10 ⁻⁶ m, 7.12×10 ¹⁵ m ²	-
	5.0	5.02×10 ⁻¹⁰ m, 0.11×10 ⁻⁶ m, 3.17×10 ¹⁵ m ²	4.05×10 ⁻¹⁰ m, 0.09×10 ⁻⁶ m, 3.65×10 ¹⁵ m ²	-
	7.5	5.55×10 ⁻¹⁰ m, 0.27×10 ⁻⁶ m, 1.95×10 ¹⁵ m ²	2.86×10 ⁻¹⁰ m, 0.13×10 ⁻⁶ m, 3.84×10 ¹⁵ m ²	3.15×10 ⁻¹⁰ m, 0.14×10 ⁻⁶ m, 2.96×10 ¹⁵ m ²
	10.0	4.47×10 ⁻¹⁰ m, 0.36×10 ⁻⁶ m, 6.48×10 ¹⁴ m ²	5.71×10 ⁻¹⁰ m, 0.19×10 ⁻⁶ m, 1.01×10 ¹⁵ m ²	4.11×10 ⁻¹⁰ m, 0.08×10 ⁻⁶ m, 4.27×10 ¹⁵ m ²

4.3.2. Comparison of Morse and LJ adhesive pressures

We now use the example of a thiol-gold interaction to highlight the difference in adhesive behavior predicted by a Morse potential and an equivalent LJ potential [Figure 4.1a]. The non-dimensional adhesive ($F^{ad*} = F^{ad}/A_n H$) force between a flat gold substrate and a rough thiol surface (i.e., a single layer of thiol groups) is plotted in Figure 4.5a as a function of d^* using Eq. (24) (Morse potential-based, solid blue line) and using the KE model⁸¹ (LJ potential-based, solid red line) with appropriate values of $\Delta\gamma$ (calculated separately for the Morse and LJ cases), r_0 , and σ . Details of the formulation involving surface-substrate adhesion based on the LJ potential are described in Appendix 8.4 and were derived as an extension to the KE model. The roughness parameters η , R , σ_h , and σ_s are obtained from AFM measurements of a gold surface, as outlined

in Section 4.2.6, and are listed in Table 4.1 for one particular AFM measurement from a set of separate measurements (details in Appendix 8.6). It must be noted that the roughness parameters listed in Table 4.1 are for the new, effective rough surface for which the AFM measurements of the surface heights were doubled before using Eqs. (4.27)-(4.30). Expressions for the total non-dimensional contact pressure P_{cs}^* and the percentage contact area A^* between deforming asperities and the substrate are provided in Appendix 8.5. The contact reaction pressure using Eq. (8.5.1) is also plotted in Figure 4.5a (dashed line).

The equilibrium separation between the bodies under contact is achieved when $P_{ad}^* = F^{ad^*}/A_n = P_{cs}^*$, (i.e., a balance between the adhesive and contact pressures). This separation is found by identifying the point of intersection between the adhesive and contact pressure curves, as shown in Figure 4.5a. If an external load is applied to the top surface, then it is added to P_{ad}^* . This equilibrium separation is then used to find the percentage contact area A^* , whose behavior as a function of d^* [using Eq. (8.5.2)] is shown in the inset of Figure 4.5a. The Morse potential-based adhesion model predicts 1.74 times the percentage contact area than the LJ based model, therein emphasizing the importance of the specialized framework based on the Morse potential.

4.3.3. *Application to thin films: Self-assembled monolayer on gold*

Thin films of SAMs provide a convenient and simple system to tailor interfacial properties of surfaces.³² They have gained widespread use in nanoscience with applications in surface functionalization,^{155,156} electrochemistry,^{33,157} electronics,^{3,6} and thermoelectrics.^{12,46,158} A thiol-based SAM on a gold substrate is the most widely-studied configuration with detailed studies performed on its preparation,³² structure,^{27,30} and transport properties.^{48,50,55,100}

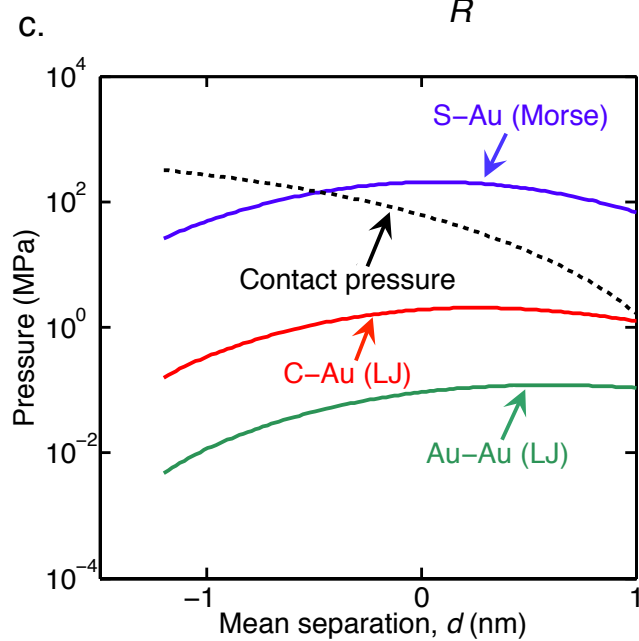
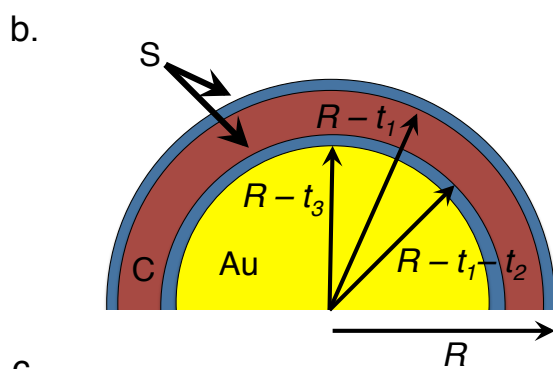
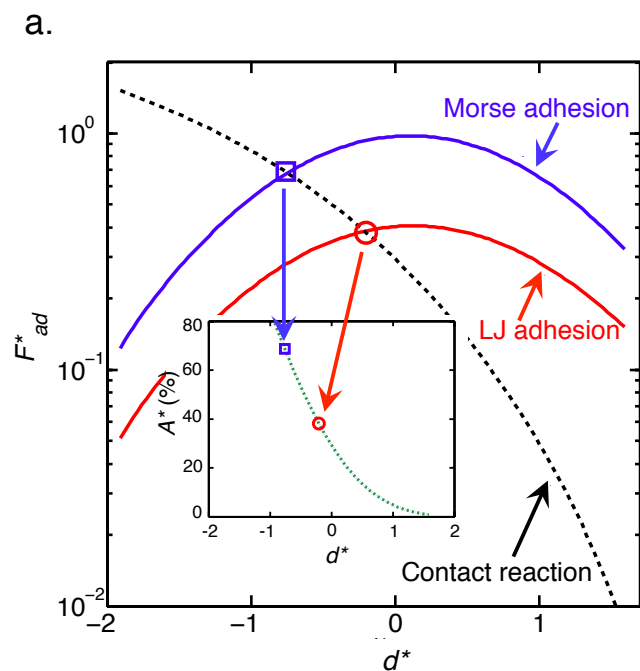


Figure 4.5. (a) Comparison of the non-dimensional adhesive pressure calculated using the Morse potential-based (solid blue line) and LJ potential-based (solid red line, similar to the KE model⁸¹) contact models, and the non-dimensional contact stress, plotted as a function of non-dimensional mean separation (d^*) between a rough thiol surface and a smooth gold substrate. Inset: Percentage contact area A^* plotted as a function of d^* . (b) Hemispherical asperity composed of a thin film (1,10-decanedithiol SAM) on a gold substrate. There is an outer layer of thiols, followed by a shell of carbon atoms (thickness of $t_2 - t_1$) and an inner region of gold atoms (radius of $R - t_3$). There is an additional single thiol layer at the inner gold surface. (c) Adhesive pressure versus mean separation of asperities for different material components of the asperity – thiol (blue line), carbon (red line), and gold layers (green line) with the planar gold substrate. The contact reaction pressure (dashed line) for the asperity is also plotted and is not affected by the structure of the asperity.

Many experiments for probing the transport properties of SAMs require the formation of a SAM junction.^{48–51,55,100} Here, a SAM grown on one substrate has another substrate (usually a metal) brought in contact with it either through high-energy deposition techniques such as sputtering or evaporation¹⁵⁹ or through transfer printing.⁹⁰ The latter technique is widely used, as it does not damage the underlying SAM layer during the formation of the junction.^{90–92} This technique has recently been used to create SAM junctions comprised of metal-dielectric^{48,50} and metal-metal substrates¹⁰⁰ to study the junction thermal conductance. Experimental measurements of the junction thermal conductance,^{50,100} however, do not agree with predictions from molecular dynamics simulations.^{53,56,100} We hypothesize that a major source of this discrepancy is incomplete contact between the two surfaces – one being the SAM grown on a metal/dielectric and the other being the bare transfer-printed metal.

Using our Morse potential-based contact model in conjunction with the composite asperity model, we can predict the percentage contact area between two rough metal substrates where one has a SAM grown on its surface. We choose a system composed of a 1,10-decanedithiol SAM grown on a gold substrate brought in contact with another gold substrate, which is identical to the system recently studied by Majumdar *et al.*¹⁰⁰ The asperities are composed of three materials – thiol (denoted by S), carbon (denoted by C), and gold (denoted by

Au: we also neglect the contribution of hydrogen atoms) as shown in Figure 4.5b. The planar substrate is gold. The thiol layers are single-atom thick and are treated as surfaces. The thickness of the carbon layer is assumed to be 12 Å, given that the SAM layer has an average thickness of 16 Å,¹⁰⁰ which is commensurate to that measured in other experiments.^{30,32} The asperities defining the carbon shell are assumed to be shifted 1.5 Å (t_1) and 13.5 Å (t_2) from the asperity surface. The inner thiol layer is shifted by 15 Å (t_3), which is also where the Au section of the asperity is assumed to begin. The thiol-gold interaction is modeled using a Morse potential while the carbon-gold and gold-gold interactions are modeled using LJ potentials (and the KE model for their adhesion). We calculate a plasticity index of 12 ± 3 for our gold samples [using Eq. (8.2.4)], which is consistent with those reported in literature for sputtered gold.¹¹⁵

The adhesive pressure between the flat gold substrate and each of the three components in the asperities and the contact pressure are plotted in Figure 4.5c as a function of the mean separation between the two surfaces. The contribution from the two different thiol layers is added together into a single thiol adhesion curve. The material properties used to plot the curves in Figure 4.5c are listed in Table 4.1. The total adhesive pressure is the sum of the individual contributions from each material within the asperity and is dominated (>99%) by the thiol-gold adhesion involving the thiol layer closest to the asperity surface. Materials deeper in the asperity and thus further away from the flat substrate exhibit a lower adhesion. The equilibrium separation between the surfaces is found from the intersection of the total adhesive pressure and contact pressure, which is then used to find the percentage contact area using Eq. (8.5.2). Using surface topography data obtained from our AFM scans of the gold substrate used to create the SAM junction in Ref. 100, we predict a percentage contact area A_M^* of $56 \pm 25\%$ ¹⁶⁰ between the two surfaces. The percentage contact area is strongly correlated to the RMS surface roughness,

as shown in the sensitivity analysis (details in Appendix 8.6). The uncertainty value of 25% is obtained by averaging the uncertainty for each AFM scan, details of which are provided Section 2.3.2.

To demonstrate the importance of using the Morse potential-based contact model within the composite asperity model, we also predict the percentage contact area by using an equivalent LJ potential to describe the thiol-gold adhesion (as described in Section 4.3.2). Keeping all other parameters the same (as listed in Table 4.1), we predict a percentage contact area A_{LJ}^* of $31 \pm 17\%$.

We assess the accuracy of the predicted percentage contact areas from the Morse and LJ models by using them to compare experimental measurements of junction thermal conductance G_{exp}^{junc} , performed by Majumdar *et al.*,¹⁰⁰ to area-corrected predictions $G_{M/LJ}^{junc}$ from MD simulations. For an Au-(1,10-decanedithiol)-Au junction, G_{exp}^{junc} was obtained using frequency domain thermoreflectance (FDTR) and represents the thermal conductance of the entire SAM junction.¹⁰⁰ Assuming that the SAM itself has a negligible thermal resistance compared to the interfaces, G_{exp}^{junc} can be approximated as two interface thermal conductances in series (one at each gold substrate). Based on the fabrication technique described in Ref. 100, the interface on which the SAM is grown is assumed to be perfect. Its interface thermal conductance is represented by G_{MD}^{int} , the MD predicted thermal conductance of a perfect thiol-gold interface and is $226 \pm 18 \text{ MW/m}^2\text{-K}$.¹⁰⁰ The other interface is comprised of a rough gold substrate transfer printed onto the SAM surface. Its interface thermal conductance $G_{M/LJ}^{int}$ is estimated using the Morse- or LJ-based contact models. The final prediction of $G_{M/LJ}^{junc}$ is thus given by

$$\frac{1}{G_{M/LJ}^{junc}} = \frac{1}{G_{MD}^{int}} + \frac{1}{G_{M/LJ}^{int}}. \quad (4.31)$$

We follow the methodology described by Seong *et al.*¹¹⁵ and Prasher and Phelan¹¹⁶ to obtain the area-corrected prediction of interface thermal conductance $G_{M/LJ}^{int}$ using

$$\frac{1}{G_{M/LJ}^{int}} = \left(\frac{1}{\eta \int_{d^*}^{\infty} \phi^*(z^*) dz^*} \right) \left[\frac{1}{\pi a_R^2 G_{MD}^{int}} + \frac{\left(1 - \sqrt{A_{M/LJ}^*} \right)^{3/2}}{2 k_H a_R} \right], \quad (4.32)$$

where a_R is the mean radius of the contact region of asperities given by $\sqrt{A_{M/LJ}^*} [\pi \eta \int_{d^*}^{\infty} \phi^*(z^*) dz^*]^{-0.5}$, and k_H is the harmonic mean of the thermal conductivities of the contacting bodies, which here is given by $2k_{SAM}k_{Au}/(k_{SAM} + k_{Au})$, where k_{SAM} (4 ± 1 W/m-K) and k_{Au} (185 ± 10 W/m-K) are the thermal conductivities of the SAM and the gold substrate.¹⁰⁰ The first term inside the square brackets on the right-hand side of Eq. (4.32) represents the thermal conductance for the regime where the mean free path (MFP) of the heat carriers (in this case, atomic vibrations or phonons) is comparable to the size (represented by a_R) of the contact regions. The second term represents the regime where the MFPs are much smaller than a_R . For the case where the MFPs are much smaller than a_R , the interface thermal conductance is the Maxwell constriction conductance as described by Prasher and Phelan.¹¹⁶

Using Eq. (32), we find G_M^{int} to be 112 ± 45 MW/m²-K and G_{LJ}^{int} to be 61 ± 26 MW/m²-K, based on averaging over all AFM measurements (details of the uncertainty calculation are provided in Appendix 8.7). We now use Eq. (4.31), finding G_M^{junc} to be 73 ± 20 MW/m²-K and G_{LJ}^{junc} to be 47 ± 17 MW/m²-K. From the FDTR measurements, the experimental value of the junction thermal conductance G_{exp}^{junc} is 65 ± 7 MW/m²-K.¹⁰⁰ We independently estimate the

degree of agreement between the experiment and Morse or LJ predictions using an overlapping coefficient (OVL).¹⁶¹ The OVL is equal to the area of the overlapping region between the normal two distributions.¹⁶¹ It can be calculated as:

$$\text{OVL} = \int_{-\infty}^{\infty} \min [f_1(x), f_2(x)] dx \quad (9)$$

where f_1 and f_2 are normal distributions. When comparing with G_{exp}^{junc} , we find the OVL to be 0.50 with the Morse-based prediction and 0.38 with the LJ-based prediction.¹⁶²

The Morse potential is a physically-accurate description of the thiol-gold bond present in our junctions (as shown in Ref. 98 and used by us in Ref. 100). Thus, an adhesion model derived using the Morse potential is a better representation of our system. It should also provide the more accurate prediction of percentage contact area compared to using an equivalent LJ potential. Our finding of better agreement between the Morse prediction and the experimental measurements of the SAM junction thermal conductance support these arguments. This study can also potentially explain the discrepancy between electronic conductance measurements of SAMs made by different research groups.^{42,109,163–165} Measurements using nano-transfer printed metal films, AFM tips, STM tips, and sputtered metal films as electrodes are also sensitive to the areal contact between the molecular layer and the surface of the metal film. Some of these works measured the surface roughness of their films and even attributed the observed variations of measured electronic conductance to it,^{42,109,164,165} especially for interfaces having strong, covalent bonds (e.g., the thiol-gold interface studied in this work). None, however, use rigorous mathematical analysis as we have done here to quantify the areal contact at the metal-molecular layer interface.

In this chapter, we formulated a rough surface contact model that accounts for plasticity through the FEA-derived model of Kogut and Etsion, and adhesion through the use of the DMT model in conjunction with the Morse potential. Our Morse potential-based contact model is

especially useful for covalently bonded materials whose interactions cannot be accurately described using an LJ potential. A composite asperity model was derived to extend this study to a layered substrate and applied to a system comprised of a thiol-based SAM on a gold substrate in contact with another rough gold substrate, as shown in Figure 4.5b. Generalized expressions for calculating the work of adhesion and equilibrium separations between a surface and a substrate interacting through a Morse potential were also presented, which only required knowledge of the Morse potential parameters and the substrate lattice constant. The percentage contact area between these rough bodies was found to be $56 \pm 25\%$ when using the Morse-based adhesion model and $31 \pm 17\%$ for the LJ-based model. Using the Morse prediction of percentage contact area provided better agreement between experimentally measured and MD predicted values of the thermal conductance of a thiol-based SAM junction than the LJ prediction. The Morse potential-based contact model will be an important tool for researchers to quantify how charge and energy transport through covalent interfaces are influenced by incomplete areal contact.

5. Chapter 5: Cooperative behavior between molecules and its effect on junction thermal conductance

5.1. Introduction

Devices based on molecular junctions have garnered widespread interest among researchers especially for their use in electronics,^{2,5,6,166} LEDs,^{8,167,168} and thermoelectrics.^{12-14,158,169,170} The interfaces between the organic and inorganic components dominate both electronic and thermal transport phenomena in these devices and materials. Both electronic and thermal transport properties of organic-inorganic heterojunctions have been shown to be tunable based on vibrational and electronic properties of the substrate, type and length of molecule, and nature of end-groups.^{13,51,100,15,39,49,50} However, the effect of local molecular environment on transport physics has only been characterized for electronic transport.¹⁷¹⁻¹⁷³ Intermolecular ‘cooperative’ effects need to be understood in order to effectively scale between single molecule devices and two-dimensional devices involving an array of molecules such as in self-assembled monolayers (SAMs).

The cooperative behavior between molecules influencing the electronic conductance of heterojunctions has been extensively investigated. Selzer *et al.* experimentally measured different per molecule conductances for an Au-(1-nitro-2,5-di(phenylethynyl-4'-mercapto)benzene)-Au junction depending on whether they probed an isolated molecule or a SAM.¹⁷¹ They showed that for high bias voltages, the conductance of an isolated molecule junction could increase and be comparable to the conductance of a SAM junction. Nerngchamnong *et al.* used the ‘EGaIn’ technique to experimentally measure the rectifying current through a SAM-based diode and found that a higher strength of intermolecular van der

Waal interactions led to increase packing density, ability to rectify current and overall device efficiency.¹⁷² Computational investigations employing first-principles calculations and tight-binding models have shown the per molecule electronic conductance to be a function of direct electronic (dipole) coupling between molecules,^{173,174} level of interaction of the molecular states with the substrate energy levels,¹⁷⁵ and electrostatic effects within the molecules.¹⁷⁶ Such detailed analyses investigating the effect of the local molecular environment and cooperative behavior between molecules on the thermal conductance in SAM junctions is still missing.

In order to probe such cooperative effects, binary SAM junctions can be used since they create an anisotropic bonding environment at one metal-SAM interface. Experimentally probing thermal transport properties of such systems is a convenient method to observe any cooperative molecular effects. The morphology of binary SAM systems has been well established in the literature and it has been conclusively shown that in solution-based binary SAM preparations, the concentration of the molecules in the solution does not equal the concentration of the molecules in the SAM.^{177,178}

Thermal transport through SAM junctions have been extensively explored only for systems synthesized from a single species of organic molecule.^{51,100,50,22,48,179} The vibrational overlap between organic molecules and inorganic substrates and the interfacial bond strength have been leveraged to tune the thermal conductance of a SAM junction from 10 MW/m²-K to 300 MW/m²-K.^{51,100,50} In a standalone study, Losego *et al.* investigated the variation of junction thermal conductance for thiol- and methyl-terminated binary SAMs between Au and quartz substrates.⁵⁰ Both kinds of molecules had equal lengths and they found that the thermal conductance decreased as the concentration of the weaker methyl-terminated molecule in the

SAM-forming solution increased. No further analysis on the variation of the thermal conductance as a function of the SAM composition on the substrate was reported.

With regard to computational investigations of cooperative effects, Sasikumar *et al.* performed molecular dynamics (MD) simulations to predict the interface thermal conductance between two polyethylene chains and Si substrates.¹⁸⁰ They reported that the thermal conductance increases as the mean distance between the polymer chains increases, even when chains are too far apart to directly interact with each other. No additional investigations regarding the origin of this increasing trend of thermal conductance were reported. In another study, Luo and Lloyd performed MD simulations of partially packed Au-decanedithiol-Au SAM junctions and reported a linear decrease in thermal conductance of the junction as they reduced the number of SAM molecules in their simulation cell.⁵⁴ They did not, however, vary the molecular packing down to the scale of a single molecule junction.

In this thesis, we systematically measure the junction thermal conductance of binary (alkanethiol and alkanedithiol) SAMs sandwiched between two Au leads. An analytical mapping between the concentration of molecules in the SAM solution and the composition of the SAM on the substrate is utilized to understand the thermal conductance behavior. We complement these measurements using experimentally validated MD simulations and contact area calculations. Using the MD simulations, we quantify the effect of non-bonded steric interactions and the cooperative behavior between molecules on the thermal transport across the SAM junction.

5.2. Sample preparation and FDTR setup

Binary SAMs were synthesized from 1,10-decanedithiol ($C_{10}H_{22}S_2$, denoted later as $C_{10}S_2$), 1-Hexanethiol ($C_6H_{14}S$, denoted later as C_6S), 1-Undecanethiol ($C_{11}H_{24}S$, denoted later as

C₁₁S), and 1-Tetradecanethiol (C₁₄H₃₀S, denoted later as C₁₄S). The molecules were mixed in 100% ethanol in appropriate ratios, while maintaining a total solution concentration of ~1-10mM. Templated Au leads (475±25 nm in thickness) were then immersed in the SAM solution to initiate SAM growth, as described in Ref. 100. A schematic representation of a fully dithiol, fully monothiol, and a binary SAM of dithiols and monothiols (of equal length) is shown in Figure 5.1a. Every binary SAM in this study consists of the dithiol (C₁₀S₂) mixed with any one of the monothiols (C₆S, C₁₁S, or C₁₄S). For example, the mixture of C₁₀S₂ and C₁₁S will be represented as C₁₀S₂:C₁₁S. A second 95±5 nm Au film was then transfer printed onto the SAM to create the junction. The transfer printing technique was shown by Ref. 100 to be effective in creating reproducible, insulating junctions without electric shorting between the metal leads.

We quantify the molecular configuration of the various mixed SAMs (C₁₀S₂:C₆S, C₁₀S₂:C₁₁S, and C₁₀S₂:C₁₄S) using advancing contact angle measurements. We plot the cosine of the contact angle $\cos \theta_{a,SAM}$ (using DI-H₂O) in Figure 5.1b as a function of the ratio of the molecular concentrations of the monothiol and dithiol in the solvent solution, given by $R_{soln} = [\text{Monothiol}]/[\text{Dithiol}]$. The contact angle increases from a fully dithiol to fully monothiol SAM as the surface changes from hydrophilic (thiol-terminated SAM surface) to hydrophobic (methyl-terminated SAM surface), an observation consistent with findings in literature.^{177,181} The rate of change of the contact angle is different for each mixed SAM composition is due to the difference in relative rates of adsorption of different sized molecules.^{177,182}

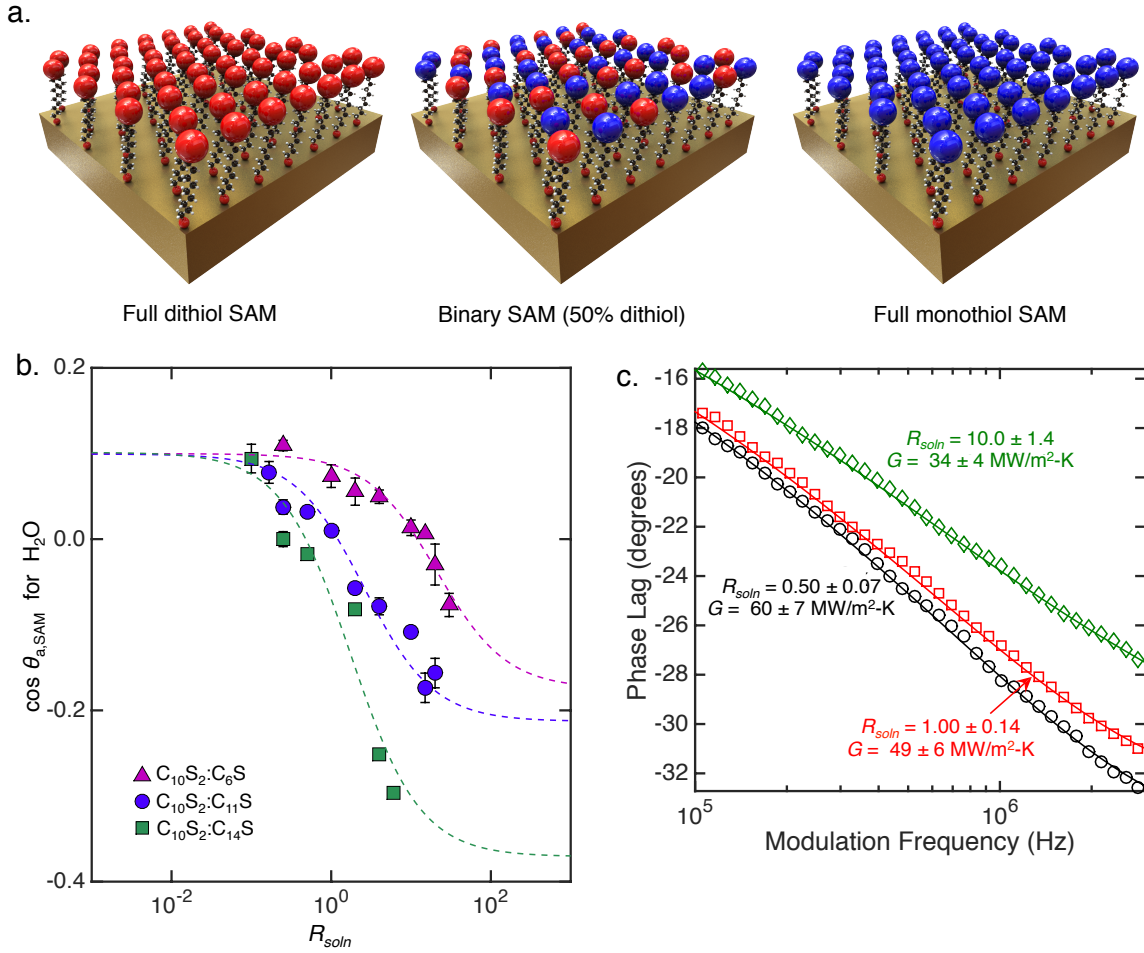


Figure 5.1. (a) Schematic representations of a full dithiol, a full monothiol and a binary SAM (50% di and 50% monothiol) grown on Au leads. The terminal groups have been magnified to emphasize their type. (b) Advancing contact angle measurements of $C_{10}S_2:C_6S$, $C_{10}S_2:C_{11}S$, and $C_{10}S_2:C_{14}S$ mixed SAMs plotted as a function of R_{soln} . The lines represent Eq. 1 fitted to the three mixed SAM compositions. (c) FDTR phase lag data as a function of the modulation frequency are fit with an analytical solution to the heat diffusion equation for three $C_{10}S_2:C_{11}S$ SAM configurations.

The contact angle measurement data can be fit to a first-order adsorption model using the expression¹⁷⁷

$$\cos \theta_{a,SAM} = \cos \theta_{a,1s} + (\cos \theta_{a,2s} - \cos \theta_{a,1s}) \left(\frac{1}{k_{rel} R_{soln} + 1} \right), \quad (5.1)$$

where $\cos \theta_{a,1s}$ is the cosine of the contact angle for a full monothiol SAM, $\cos \theta_{a,2s}$ is the cosine of the contact angle for a full dithiol SAM, and k_{rel} is the ratio of adsorption rates between the monothiol (k_{1s}) and the dithiol (k_{2s}) given by $k_{rel} = k_{1s}/k_{2s}$. We perform a non-linear least squares fit to estimate the value of k_{rel} and use it with Eq. 1 to plot the lines in Figure 1b. The fitted values of k_{rel} are 0.56 ± 0.04 for $C_{10}S_2:C_{14}S$, 0.39 ± 0.01 for $C_{10}S_2:C_{11}S$, and 0.05 ± 0.01 for $C_{10}S_2:C_6S$.

The thermal conductance G of the SAM junction was measured using frequency domain thermoreflectance (FDTR), a non-contact laser based measurement technique that is ideal for measuring thermal properties of atomistic interfaces and thin-films.^{100,85,23} A prior study indicates that our FDTR setup is sensitive to G .¹⁰⁰ In FDTR measurements, the phase lag between the temperature modulation of the sample surface (532 nm probe laser) and the imposed periodic heat flux (488 nm pump laser) is fitted with an analytical solution to the heat diffusion equation to extract G .⁸⁷ The phase lag data along with the associated fitted solution are plotted in Figure 5.1c as a function of the modulation frequency (50 kHz – 3 MHz). The three datasets represent different molecular configurations for the $C_{10}S_2:C_{11}S$ mixed SAM exhibiting different values of G – 60 ± 7 MW/m²K ($R_{soln} = 0.50 \pm 0.07$), 49 ± 6 MW/m²K ($R_{soln} = 1.00 \pm 0.14$), and 34 ± 4 MW/m²K ($R_{soln} = 10.0 \pm 1.4$). We could not successfully measure samples having >80% C_6S and >50% $C_{14}S$ in the solution, probably due to defects being formed in the SAM creating metallic shorting between the Au leads. We prepared at least two samples for every mixed SAM composition and measured at five different laser spot locations on each sample.

5.3. FDTR results

The correlation between R_{soln} and the mole fraction of molecules in the SAM itself is derived from Eq. 1 as

$$\chi_{1s,SAM} = \frac{k_{rel}R_{soln}}{k_{rel}R_{soln} + 1}, \quad (5.2)$$

where $\chi_{1s,SAM}$ is the mole fraction of the monothiol in the SAM. We plot the mole fraction of the monothiol in the solution, given by $\chi_{1s,soln} = R_{soln}/(R_{soln} + 1)$, in the upper panel of Figure 5.2 as a function of $\chi_{1s,SAM}$ for all three binary SAM mixtures. All three data sets deviate from a linear relation between $\chi_{1s,soln}$ and $\chi_{1s,SAM}$ representing the case where the mole fraction of monothiols in the SAM would equal their mole fraction in the solution.

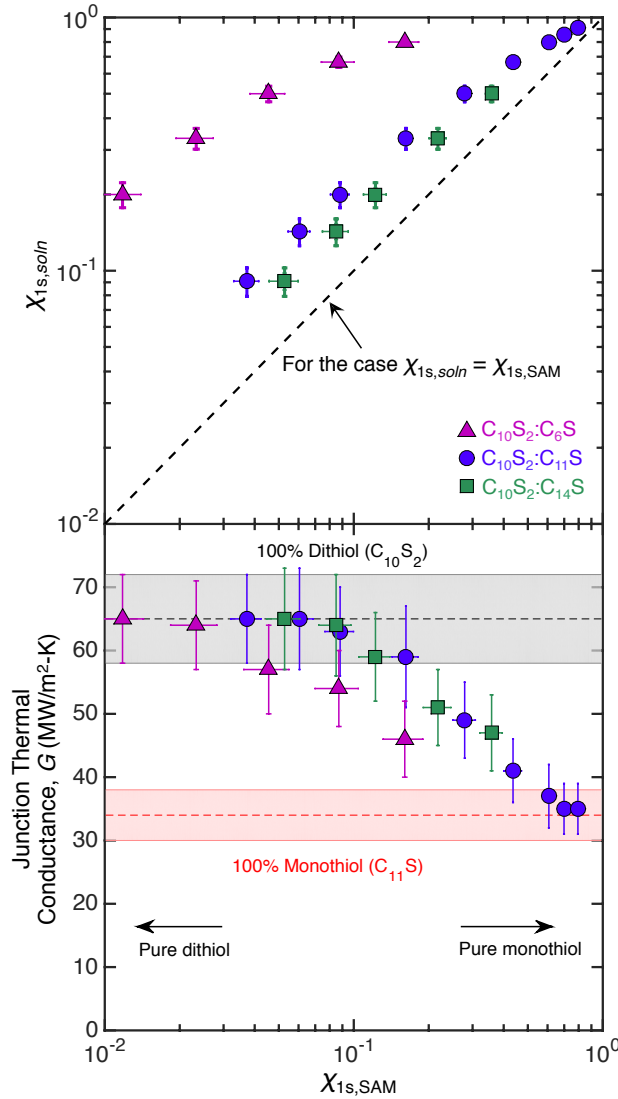


Figure 5.2. (Upper panel) $\chi_{1s,soln}$ for $C_{10}S_2:C_6S$, $C_{10}S_2:C_{11}S$, and $C_{10}S_2:C_{14}S$ plotted as a function of $\chi_{1s,SAM}$. The dashed line denotes the case when there is no difference between the concentration of monothiols in the solution and

the SAM. (Lower panel) G for $C_{10}S_2:C_6S$, $C_{10}S_2:C_{11}S$, and $C_{10}S_2:C_{14}S$ plotted as a function of $\chi_{1s,SAM}$. All experiments were performed at an ambient room temperature of 296 K.

We plot G as a function of $\chi_{1s,SAM}$ in the lower panel of Figure 5.2 for all three mixed SAM compositions. The extreme cases, relating to $R_{soln} = 0$ and $R_{soln} \rightarrow \infty$, are plotted as continuous horizontal lines with shaded uncertainty (65 ± 7 MW/m²-K for an Au- $C_{10}S_2$ -Au, and 34 ± 3 MW/m²-K for an Au- $C_{11}S$ -Au junction). The thiol-Au interaction is stronger than the methyl-Au interaction, which leads to a higher junction thermal conductance for a fully dithiol SAM junction as compared to a fully monothiol SAM junction.^{100,50}

We observe a non-linear decrease in G with increasing $\chi_{1s,SAM}$ for all mixed SAM compositions. This trend suggests the presence of cooperative effects between the molecules affecting thermal transport, and we hypothesize the molecules cannot be treated as independent heat channels. The decreasing trend in G is related to the changing bonding environment at the SAM-Au interface containing the transfer printed Au substrate, as the interface structure changes from a thiol group-dominated interface (strong interfacial bonding) to a methyl group-dominated one (weak interfacial bonding). We find that for any given value of $\chi_{1s,SAM}$, the value G for $C_{10}S_2:C_{11}S$ is consistently higher than $C_{10}S_2:C_6S$. We hypothesize that this behavior is due to the increased distance between the methyl end-group of the monothiol SAM (when using C_6S as compared to $C_{11}S$) and the transfer-printed Au surface, which alters the strength of interaction between the SAM and the Au lead. The values of G for $C_{10}S_2:C_{11}S$ and $C_{10}S_2:C_{14}S$ are comparable and we hypothesize that this is due to bending of the longer $C_{14}S$ molecules leading to an interface that has a similar bonding environment as that of the $C_{10}S_2:C_{11}S$ structure.

5.4. Contact area correction

Probing the origin of these cooperative effects on thermal transport requires a more detailed analysis at the atomistic level, for which we use MD simulations. The MD simulation setup is similar to the system studied previously by us in Ref. 100. We describe the interaction of the terminal methyl group on the monothiols with all other atoms through LJ potentials and by using the standard mixing rules,³⁴ details of which are provided in Section S3 of the SI. All simulations were performed at a mean temperature of 300 K. Our principal system for the MD simulations is the $C_{10}S_2:C_{11}S$ SAM between two Au leads. We vary the fraction of $C_{11}S$ molecules and calculate G for the various configurations. The positions of $C_{10}S_2$ and $C_{11}S$ molecules in the mixed SAM are randomized and the reported values of G are an average of three independent structures. We predict 113 ± 9 MW/m²-K for the Au- $C_{10}S_2$ -Au configuration and 17 ± 2 MW/m²-K for the Au- $C_{11}S$ -Au configuration.

The validity of the MD simulations to predict G of the binary SAMs is tested by comparing its results with the FDTR measurements. The variation of G for $C_{10}S_2:C_{11}S$ is plotted in Figure 5.3 as a function of $\chi_{1s,SAM}$ for both the MD predictions and FDTR measurements. However, a direct comparison is possible only after correcting for the percentage contact area between the SAM and transfer-printed Au lead. The percentage contact area is calculated using a statistical model for contacting rough surfaces developed by us, as reported in Refs. 100,101. The area-corrected MD data, also plotted in Figure 5.3, match the FDTR measurements both in magnitude and observed trend. It must be noted, however, that for the region where $\chi_{1s,SAM} > 0.5$ (where the weak methyl-Au interaction dominates), the area corrected MD predictions begin to underestimate the FDTR measurements. This under-prediction suggests that the LJ potential available in the literature is too weak to describe the methyl-Au surface interaction. Creating a

new empirical potential from first-principle calculations and its subsequent validation is not the goal of this study.

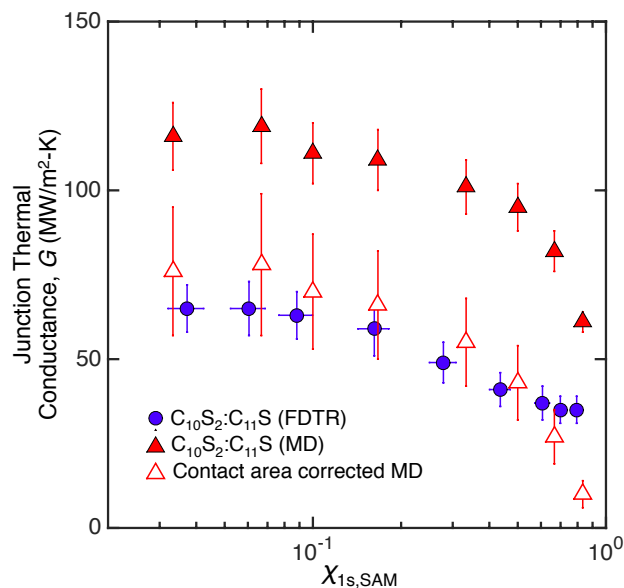


Figure 5.3. Comparison between FDTR measurements, MD predictions, and percentage contact area-corrected MD predictions of the junction thermal conductance of the $C_{10}S_2:C_{11}S$ system as a function of $\chi_{1s,SAM}$.

5.5. Simulation results

We now focus on the MD predictions to systematically investigate the effects of cooperative behavior between the molecules on the junction thermal conductance as well as elucidate its origin, avoiding any effects of incomplete contact on the observed trends. The variation of G as a function of $\chi_{1s,SAM}$ is plotted again in Figure 5.4, but now with a linear horizontal axis. G decreases non-linearly with increasing $\chi_{1s,SAM}$, a trend that is also qualitatively observed in the FDTR experiments. If each SAM molecule acted as an independent heat channel, the junction thermal conductance would linearly change from the fully dithiol to the fully monothiol case (since the molecules would act as thermal conductors connected in parallel), as

indicated by the red-dashed line in Figure 5.4. Since the MD predicted values do not follow this linear behavior, the molecules cannot be represented as independent heat channels – thus proving our initial hypothesis of cooperative behavior between the molecules from the experimental measurements.

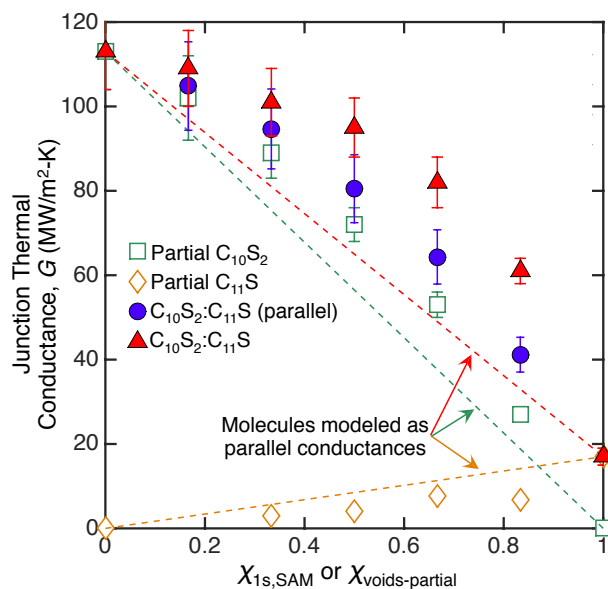


Figure 5.4. Variation of G for the $C_{10}S_2:C_{11}S$ mixed SAM, the partially packed $C_{10}S_2$ SAM, and the partially packed $C_{11}S$ SAM plotted as a function of the fraction of $C_{11}S$ in the mixed system or voids in the partial SAM system. The dashed lines represent the variation of G if the molecules behaved as parallel conductances. Comparison between the MD simulation results of the $C_{10}S_2:C_{11}S$ mixed SAM configuration and the case where the partially packed $C_{10}S_2$ SAM is added to the parallel conductance assumption for the $C_{11}S$ SAM (yellow dashed line in the main plot) to predict an upper limit to the effective thermal conductance for the mixed SAM case based on parallel conductances between the $C_{10}S_2$ and $C_{11}S$ molecules.

The significance of molecular mixing on the behavior of G for the mixed SAM is investigated by creating SAM junctions having partial coverage of $C_{10}S_2$ and $C_{11}S$ molecules and comparing these to the mixed SAM configurations. Cooperative behavior between the $C_{10}S_2$ and $C_{11}S$ molecules that can exist in the mixed SAM configurations are not present in these partial coverage structures. The variation of G for the partially packed $C_{10}S_2$ SAM and the partially packed $C_{11}S$ SAM is also plotted in Figure 5.4 as a function of $\chi_{\text{voids-partial}}$, which is the mole

fraction of voids in the partially packed SAMs. The green and yellow dashed-lines represent the cases if the molecules behaved as independent heat channels. A non-linear behavior of G is observed for the partially packed $C_{10}S_2$ SAM. The $C_{11}S$ data has a noisier trend due to the weak methyl-Au bond leading to large structural fluctuations in the MD simulations. From Figure 5.4, it is seen that at a given value of $\chi_{1s,SAM}$ or $\chi_{voids-partial}$, the partial coverage cases exhibit a lower G as compared to the mixed SAM case. This suggests that the presence of the $C_{11}S$ molecules facilitates better heat transfer across the mixed SAM junction when compared to the partial coverage cases, leading to larger values of G .

The observation of the non-linear behavior in the partially packed $C_{10}S_2$ SAM suggests that any cooperative behavior that exists between the $C_{10}S_2$ molecules persists even without $C_{11}S$ molecules. This effect increases as the average distance between $C_{10}S_2$ molecules decreases. We validate this by calculating the per molecule thermal conductance of the $C_{10}S_2$ from the partially packed SAM data in Figure 5.4. Using the values of G for which $\chi_{voids-partial} = \{0.17, 1.00\}$, the corresponding per molecule thermal conductances are 24 pW/K and 35 pW/K. These disparate per molecule thermal conductances indicate of interactions between the molecules that are a function of the average distance between $C_{10}S_2$ molecules. An important conclusion from this analysis is that the thermal conductance for the fully packed SAM configuration cannot be used to predict the thermal conductance of a single molecule. Intermolecular crosstalk exhibits a damping effect on the thermal conductance for individual molecules as their average intermolecular distance decreases – an observation similar to one reported by Sasikumar *et al.* for polyethylene junctions.¹⁸⁰

We also emphasize that cooperative behavior between the $C_{10}S_2$ molecules alone cannot account for the increased junction thermal conductance of the $C_{10}S_2:C_{11}S$ SAM. We establish an

upper limit for the effective junction thermal conductance, assuming linear superposition between the $C_{10}S_2$ and $C_{11}S$ partial SAMs, by adding the partially packed $C_{10}S_2$ junction thermal conductance predictions from MD and the partially packed $C_{11}S$ junction thermal conductance from the parallel conductance hypothesis (yellow dashed line). We plot this upper limit as blue circle and compare it with the $C_{10}S_2:C_{11}S$ prediction from MD as a function of $\chi_{1s,SAM}$ in Figure 5.4. This upper limit consistently under predicts the MD value of thermal conductance (3% and 32%) for all $C_{10}S_2:C_{11}S$ configurations, proving the existence and importance of cooperative behavior between dithiol and monothiol species.

Our MD simulations show that cooperative behavior between molecular species can enhance thermal transport in the mixed SAM systems and can also inhibit per molecule thermal conductances depending on intermolecular spacing. However, the origin of this cooperative behavior still needs to be established. The possible pathways of crosstalk between the molecules are: i) Steric interactions between the molecules, and ii) non-bonded interactions indirectly through the substrates. Each of these possibilities will be explored using MD simulations.

Steric interactions exist through non-bonded (dipole-dipole) interactions between the molecules and are represented through LJ potentials in the simulations. We probe their effect on thermal transport by weakening these non-bonded LJ potentials by 90% (i.e., reducing the well-depth ϵ_{LJ} by 90%), for the case $\chi_{1s,SAM} = 0.5$ and the mixed SAM configurations $C_{10}S_2:C_6S$, $C_{10}S_2:C_8S$ and $C_{10}S_2:C_{11}S$. We found the predicted value of G to be unchanged when compared to the predictions using the standard LJ potentials. These values are tabulated in Table 5.1. This suggests that the steric interactions are too weak to affect thermal transport across the junction and do not contribute to the cooperative behavior.

Table 5.1. Comparison of junction thermal conductances predicted from MD simulations for three mixed SAM configurations using standard LJ interactions and 90% weaker LJ interactions.

	Junction Thermal Conductance (MW/m ² -K)	
	ϵ_{LJ}	$0.1\epsilon_{LJ}$
C ₆ S	77±4	78±5
C ₈ S	85±5	81±5
C ₁₁ S	95±7	93±6

We hypothesize that the cooperative behavior improving thermal transport through the mixed SAMs is manifested in the enhanced heat conduction through the individual C₁₁S molecules in the presence of the stabilizing C₁₀S₂ molecules. From Figure 5.4, we observe the increase of G in the C₁₀S₂:C₁₁S SAM to be twice as large as compared to the C₁₀S₂ partial SAM when moving from $\chi_{1s,SAM} = 0.83$ to 1. We validate this hypothesis by calculating the root mean-squared (RMS) displacement of the terminal methyl groups of the C₁₁S. We plot the RMS displacements of the terminal methyl group as a function of $\chi_{1s,SAM}$ for the C₁₀S₂:C₁₁S SAM and $\chi_{voids,partial}$ for C₁₁S partial SAM in Figure 5.5a.

The RMS displacements for the partial SAM cases are consistently higher than the mixed SAM cases. Coupled with the observation that G is also lower for the partial SAM cases, this suggests a high frequency of bond breakage and formation between the methyl groups and the Au atoms. This “bond breakage” frequency is likely reduced in the mixed SAM configuration due to confinement by the C₁₀S₂ molecules leading to a higher degree of coupling for the methyl-Au interaction in the presence of stabilizing C₁₀S₂ molecules. Thus, a higher ‘effective’ bond strength and per molecule interface conductance for the C₁₁S molecules is a direct result of the cooperative behavior between the molecular species. We also decompose the RMS displacements into in-plane and transverse directions with respect to the plane of the Au surface

and find that the in-plane displacement contributes to >95% of the total RMS displacement. This suggests that in-plane motion of the terminal methyl groups is the dominant influence on the vibrational coupling.

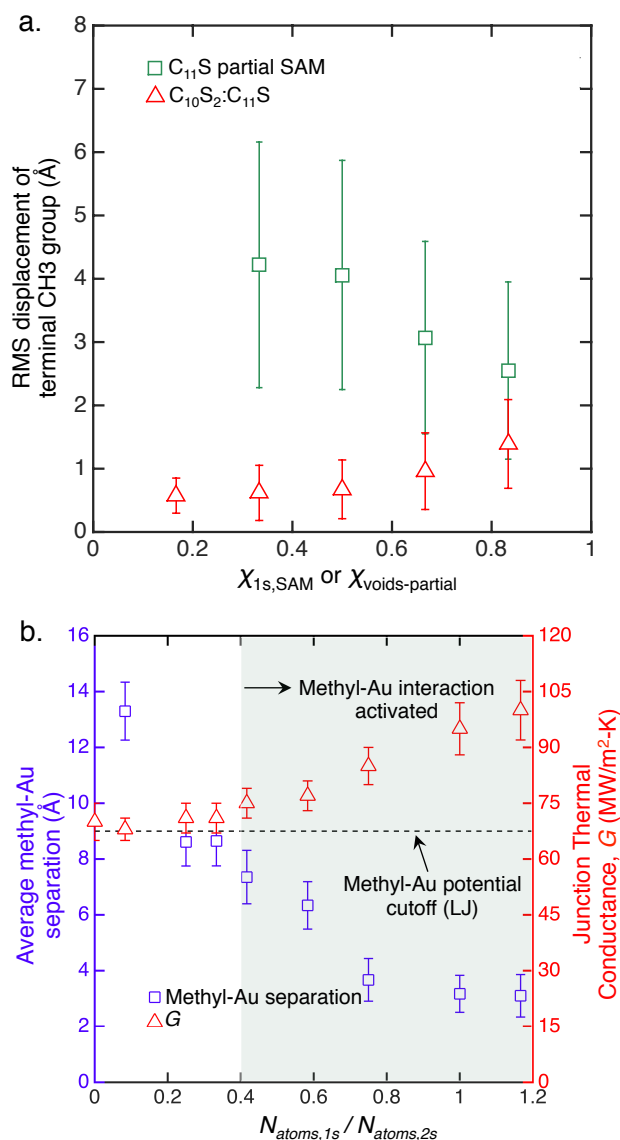


Figure 5.5. (a) Root mean-squared (RMS) displacement of the terminal methyl group plotted as a function of the fraction of $\chi_{1s,SAM}$ in a $C_{10}S_2:C_{11}S$ SAM or $\chi_{voids-partial}$ in a $C_{11}S$ partial SAM. (b) Variation of the average terminal methyl-Au separation (plotted with respect to the left vertical axis) and G from MD simulations for the $C_{10}S_2:C_{11}S$ SAM (plotted with respect to the right vertical axis) as a function of $N_{atoms,1s}/N_{atoms,2s}$ for $\chi_{1s,SAM} = 0.5$. The dashed horizontal line represents the cutoff (9 Å) for the LJ potential describing the methyl-Au bond.

We probe the effect of interactions between the terminal methyl group and the Au lead using MD simulations and mixed SAM systems having monothiols of different lengths. For this study, we keep the fraction of $C_{11}S$ molecules fixed at 0.5 (i.e., $\chi_{1s,SAM} = 0.5$). We plot the average separation of the methyl group from the surface of this Au substrate, as a function of the number atoms in the monothiols $N_{atoms,1s}$ (normalized by the number of atoms in the dithiol $N_{atoms,2s}$, in this case equal to 12) in Figure 5.5b. The average methyl-Au surface separation monotonically decreases for values of $N_{atoms}/N_{atoms,dithiol} < 0.75$, and above which it saturates to a constant value. We plot a horizontal line at 9 Å denoting the numerical cutoff of the methyl-Au LJ potential used in the MD simulations. Interaction between the monothiols and the Au substrate is possible only when the methyl-Au separation is within this cutoff.

Plotting the corresponding predictions of G for these mixed systems in Figure 5.5b, we observe that the value of G is constant for mixed SAM compositions with monothiols having less than 4 atoms, and increases as the monothiol length increases. This change in thermal conductance behavior coincides with the region in Figure 5.5b (colored in grey) where the average methyl-Au separation is less than the methyl-Au LJ cutoff of 9 Å, i.e., when $N_{atoms}/N_{atoms,dithiol} > 0.4$ in our simulations. We conclude that the strength of interaction between the monothiols and the Au substrate in the mixed SAM system can be tuned by the methyl-Au separation. This influences the strength of interaction between the SAM and the lead, supporting the hypothesis we established from our experimental measurements plotted in Figure 5.2. We provide further support for this hypothesis by predicting G as a function of $\chi_{1s,SAM}$ for the $C_{10}S_2:C_6S$ and $C_{10}S_2:C_{14}S$ cases using MD simulations. We found the $C_{10}S_2:C_6S$ predictions to be lower and $C_{10}S_2:C_{14}S$ to be comparable to the $C_{10}S_2:C_{11}S$ predictions, similar to the FDTR measurements plotted in Figure 5.2b.

In this chapter, we investigated the effect of cooperative behavior between molecules on the thermal conductance of SAM junctions using binary SAM and partially covered SAM systems. The mixed SAM configurations were quantified by fitting an adsorption model to contact angle measurements of SAM surface. FDTR measurements and MD predictions of the junction thermal conductance showed a non-linear change from a fully dithiol to a fully monothiol SAM configuration suggesting cooperative interactions between molecules. MD simulations of partially covered SAM systems suggested that the strength of the intermolecular cooperation decreases as the average intermolecular distance increases. The origin of the cooperative behavior was also found to be dominated by the stabilizing effect of the anchored dithiols on the monothiols, thereby enhancing the overall methyl-Au interaction strength. The intermolecular van der Waals interaction was found to have a negligible effect on the junction thermal conductance.

6. Chapter 6: Other projects

6.1. Thermal transport enhancement of nanocomposites using polymer brushes

Polymers can be scalably manufactured and have versatile physical attributes that have led to their widespread applications. However, certain limitations such as their low thermal conductivity impede their use for various applications that include packaging technologies in high energy density applications¹⁸³ or in solid-state lighting.^{168,184} Methods to improve the thermal conductivity include bi-axial stretching to improve chain orientation¹⁸⁵ and the addition of inorganic particles with high thermal conductivity.¹⁸⁶ This work aimed at improving the thermal conductivity of a bulk polymer resin through the addition of inorganic nanoparticle fillers of silica tethered with polymeric chains. The tethered chain augments the interface thermal conductance between the organic-inorganic components. I experimentally measured the thermal conductivity of these polymer nanocomposites and assisted my colleague Clare Mahoney in elucidating the mechanism of thermal transport within these materials.

Organic polymeric resins embedded with phosphors are used as down-conversion material systems (DCMS) in LEDs. However, the decrease in the quantum efficiency of such systems at high operating temperatures is a major bottleneck for these devices and is due to the poor thermal conductivity of the resins. A novel technique to improve the resin thermal conductivity uses covalent tethering of polymer chains on embedded high thermal conductivity nanoparticles, a method developed in the Matyjaszewski lab at CMU.¹⁸⁷⁻¹⁹⁰ Covalent tethering leads to an increased thermal conductance between the particle and polymer matrix while still maintaining the optical properties of the DCMS.

The nanocomposites used in this study consisted of silica (SiO_2) nanoparticles tethered with poly(methyl methacrylate) (PMMA) and poly(styrene-acrylonitrile) PSAN brushes

(denoted as SiO₂-MMA or SiO₂-SAN) embedded in a PMMA matrix. We found that the thermal conductivity of all brush systems was greater than the corresponding binary mixture of neat SiO₂ particles in a PMMA matrix demonstrating the effect of the brushes on thermal transport. The densely grafted SiO₂-MMA28/PMMA system also had a higher thermal conductivity than the sparsely grafted SiO₂-MMA200/PMMA system, albeit the difference is modest due to experimental uncertainty. We hypothesize that this trend results from a) an increased brush-matrix interface conductance for the dense systems due to a larger number of molecules per unit area, as well as b) the potential increase of the thermal conductivity of the brush itself due to the stretched chain conformations of the denser brush system.

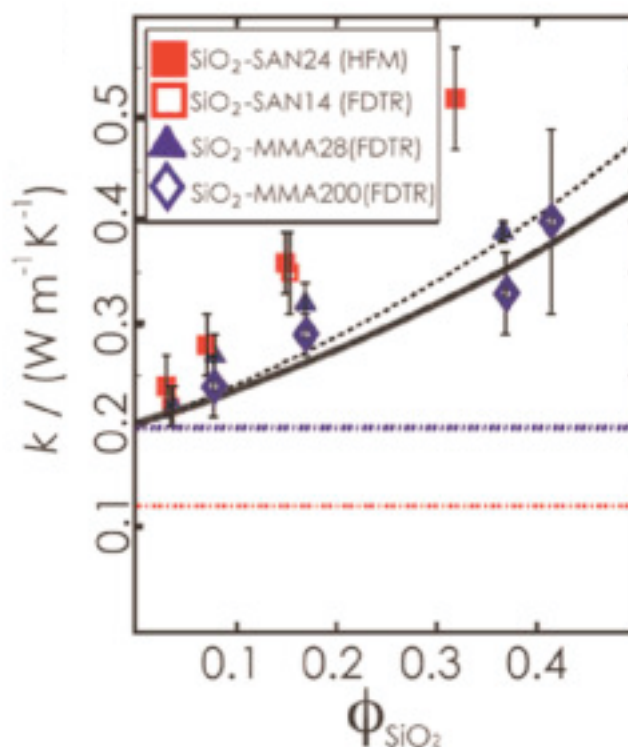


Figure 6.1. Thermal conductivity of PMMA-based composite materials. Symbols represent SiO₂-SAN24/PMMA (filled red squares) and SiO₂-SAN14/PMMA (open red squares), SiO₂-MMA28/PMMA (blue triangle) and SiO₂-MMA200/PMMA (open blue diamond), respectively. Lines represent effective medium predictions based on the Nan effective medium model assuming infinite interface thermal conductance ($G = \infty$, black dashed line) and $G = 420 \text{ MW m}^{-2} \text{ K}^{-1}$ (black solid line) as well as PMMA (blue dashed line) and PSAN (red dashed line). [C. Mahoney *et al. Polymer* (2016)]

An interesting observation was the higher thermal conductivity of the PSAN brushes when compared to PMMA brushes as well as predictions from an effective medium approximation,^{191,192} which could indicate a higher thermal conductance at the brush-matrix interface. Another reason for this observation could be that the PSAN brushes exhibit better chain conformation when tethered, leading to enhanced thermal conductivity of the brush itself.

6.2. Molecular dynamics simulation of nanocrystal arrays for thermal transport investigations

This work elucidates thermal transport physics in nanocrystal arrays (NCAs) using molecular dynamics (MD) simulations and finds that vibrational states couple elastically across the organic-inorganic interfaces in with a resulting flux that depends on the ligand grafting density and the overlap between the core and ligand vibrational spectra.²⁴ An NCA is a close-packed structure of nanocrystals (i.e., inorganic cores 2 – 20 nm in diameter encapsulated in a layer of organic ligands) that self-assemble from a colloidal solution. NCAs have been proposed as cost-effective and versatile alternatives for expensive single-crystal semiconductors in field-effect transistors,¹⁹³ memory devices,¹⁹⁴ light-emitting diodes,⁷ photodetectors,^{195,196} solar cells,^{9,197,198} and thermoelectric generators.^{199–201} I assisted my colleague Wee-Liat Ong in setting up and performing the MD simulations to predict thermal transport. Comparing the predicted NCA thermal conductivities against experimental measurements, with agreement found in both magnitude and trends, validates our approach.

The modeling was performed on an Au-dodecanethiol NCA built using a robust self-assembly methodology. We found the interface thermal conductance between the thiol-group and the Au nanoparticle to be dependent on nanoparticle size, as plotted in Figure 6.2a. This is because

the molecular footprint of the molecules changes with the curvature of the nanoparticle due to steric hindrance effects. The MD thermal conductivities for the NCAs as a function of NCA diameter are plotted in Figure 6.2b along with effective medium approximation (EMA) predictions. The MD data agree poorly with the EMA predictions that do not account for a finite Au-thiol interface thermal conductance, indicating the importance of including the interface thermal conductance in describing the thermal transport in an NCA. Those accounting for the interface thermal conductance, which could be predicted either from SAM simulations as described in Chapter 3 or separate MD simulations of NCAs, agreed well with the MD data and previous experiments. We also investigated vibrational mismatch effects between the nanocrystals and the molecules by changing the mass of the nanocrystals. We found that there is an optimum mass of the nanocrystal atoms to realize a peak in thermal conductivity of the bulk NCA and interface thermal conductance were witnessed.

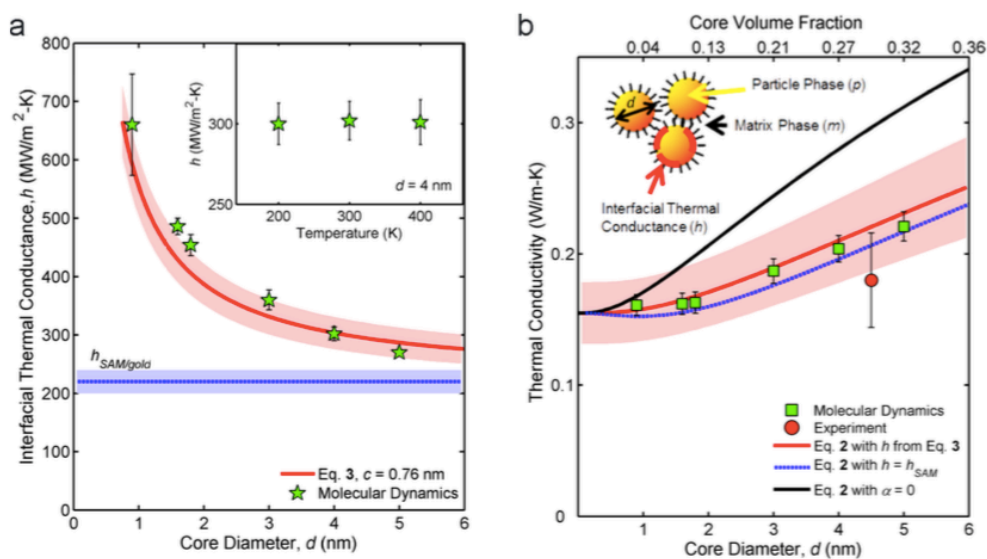


Figure 6.2. EMA investigation for diameter series. (a) Interface thermal conductance as a function of nanoparticle diameter where $h_{SAM/gold}$ is the predicted SAM thermal conductance and $c = 0.76$ nm is obtained from the footprint scaling law. The red shaded region depicts the uncertainty in the $h_{SAM/gold}$. The value of $h_{SAM/gold}$ is plotted as a blue dotted line with its associated uncertainty (blue shaded area). Inset: interfacial thermal conductance shows no temperature dependence between 200 and 400 K, indicating a dominance of elastic scattering between the

core and ligands. (b) MD diameter series is well-described by EMA-h accounting for interfacial thermal conductance between the core and ligand. The red shaded region marks the uncertainty range associated with the EMA-h model due to the uncertainties in its inputs. [W.-L. Ong *et al. J. Phys. Chem. C*, 118, 7288 (2014)]

6.3. Broadband frequency domain thermoflectance for phonon spectroscopy

This work describes the instrumentation for broadband frequency domain thermorelectance (BB-FDTR), a novel, continuous wave laser technique for phonon spectroscopy measurements and experimentally realizing the thermal conductivity accumulation function.⁸⁶ I assisted my colleague Keith Regner in the development and validation of the BB-FDTR technique.

The thermal conductivity accumulation function k_{accum} describes cumulative contributions to the bulk thermal conductivity of a material from energy carriers with different mean free paths.^{202–206} It can be used to map reductions in thermal conductivity in nano-devices, which arise when the dimensions of the device are commensurate to the mean free path of energy carriers. Efforts to measure k_{accum} had thus far been limited, the first measurement having been made only in 2007 using time-domain thermorelectance (TDTR).²⁰⁷ The dominant time scale in such experiments decides the characteristic length scale L_c , which is then compared to the mean free path of phonons in the materials under investigation. Alternatively, L_c can be set by the dimensions of nano-patterned heaters to extract the average phonon MFP of the substrate,²⁰⁸ or can be proportional to the grating period in transient grating experiments.^{203,209}

The BB-FDTR technique is based upon frequency domain thermorelectance, which is described in Chapter 2, but has additional complexity to adequately resolve k_{accum} .⁸⁶ Theoretically, since FDTR uses continuous-wave lasers, the pump beam can be modulated at an infinitely high frequency f_1 to measure the entire k_{accum} . The pump modulation creates an

exponentially decaying temperature profile characterized by the thermal penetration depth L_p that identifies the depth normal to the sample surface at which the temperature amplitude is e^{-1} of its surface amplitude. However, signal to noise ratios in FDTR decrease at larger heating frequencies due to the decreasing signal size and presence of coherent noise and ambient noise at high frequency. The BB-FDTR technique produces a high fidelity thermal signal by inducing an additional modulation on the reflected, thermally modulated probe laser at frequency f_2 . Heterodyning the probe laser allows for heating frequencies up to 200 MHz but measurement of the thermal response at a much lower frequency, $f_1 - f_2$, where the signal to noise ratio is much larger.

We present k_{accum} here for an intrinsic c-Si sample at $T = 311$ K, k_{bulk} is determined from Ref. 210 and r_{spot} was measured using the knife-edge profiling technique outlined in Ref. 26. Fitting the phase data over the entire frequency range (as is done in FDTR described in Chapter 2) to a constant value of thermal conductivity yields a poor fit and underestimates the bulk value of Si by 34%. Consequently, the phase data is divided into different windows and each window is fit individually. Using the assumption $L_c = L_p$ yields k_{accum} , as seen for Si at $T = 311$ K in Figure 6.3. In the past two years, more sophisticated methods using a suppression function relating L_c and L_p ,²¹¹ and a two-temperature model to accurately describe the metal transducer have been proposed for more accurate interpretation of the BB-FDTR data.²¹²

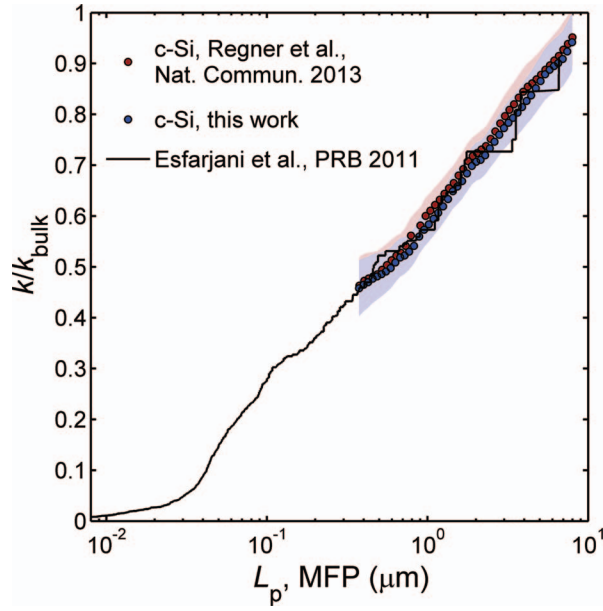


Figure 6.3. k_{accum} for c-Si at $T = 311$ K as a function of L_p . The data is normalized to $k_{bulk, Si} = 143$ W/mK and compare favorably to results in literature, both experimental²¹³ and numerical.²⁰² [K.T. Regner *et al. Rev. Sci. Instrum.* 84, 064901 (2013)]

7. Chapter 7: Summary and outlook

7.1. Experimental measurement of self-assembled monolayer (SAM) junction thermal conductance

In Chapter 2, the first-ever measurements of junction thermal conductance of metal-SAM-metal junctions were presented. The vibrational mismatch between the metal leads was varied and the effect of the mismatch on the junction thermal conductance was investigated. A statistical model for rough surfaces, described in Chapter 4, was used to estimate the percentage contact area in the SAM junctions and correlate the experimental measurements with the simulation predictions described in Chapter 3. My key findings were:

- The thermal conductance of metal-SAM-metal junctions decreases with increasing vibrational mismatch between the metal leads, especially for alkanedithiol-based SAMs. This observation was not present for alkanethiol-based SAMs, which we hypothesize is due to the weak methyl-Au bond overpowering the vibrational mismatch effect and acting as the dominant thermal resistance.
- The molecular footprint is an important quantity affecting junction thermal conductance. It must be accounted for when comparing junction thermal conductance measurements of different samples where the SAM is grown on different substrates, especially when studying vibrational mismatch effects.
- Incomplete surface contact between species comprising an interface is a critical factor affecting the measured value of junction thermal conductance. This was shown by calculating the percentage contact area in the Au-decanedithiol-Au SAM, using it to obtain an area-corrected value of junction thermal conductance (for a perfect SAM

junction) and comparing it to molecular dynamics (MD) simulation predictions. The area corrected value and MD predictions were found to agree within uncertainty.

7.2. Computational modeling thermal transport in SAM junctions

In Chapter 3, MD simulations and lattice dynamics calculations were used to study the thermal transport physics in metal-SAM-metal junctions. My key findings were:

- Elastic scattering dominates at the metal-SAM interfaces but inelastic effects occur with the SAM itself. Coupled with the classical nature of MD simulations, this can lead to the anomalous prediction that the junction thermal conductance in such systems increases with increasing vibrational mismatch of the leads.
- Reconciliation with experimental measurements of junction thermal conductance was successfully obtained by inhibiting the vibrational spectrum of the molecules. This was achieved by increasing their atomic masses and thus preventing any non-physical scattering behavior to occur within the molecules.
- A diffuse mismatch model (DMM) prediction of junction thermal conductance was found to show a similar trend as seen in the experiments and molecule-mass-corrected MD simulations. Thus, a DMM model can be used to estimate any trends in such mismatched systems as long as the interfacial bonding environment remains relatively unchanged.

7.3. Rough surface contact model for covalent interfaces

In Chapter 4, a rough surface contact model was presented to predict the percentage contact area between covalently bonded interfaces, whose interaction was described using a

Morse potential. The input to the contact model was surface topology information obtained from atomic force microscopy (AFM) measurements of the actual experimental samples. The results were validated using thermal conductance measurements of SAM junctions. My key findings were:

- The Morse potential prediction of percentage contact area differs from a prediction using an equivalent Lennard-Jones (LJ) potential to describe the interfacial bond. This is because the Morse potential has more free parameters than the LJ, thus allowing a greater adjustment to the shape of the potential well, allowing it to be more physically accurate for covalent bonds than an equivalent LJ potential well.
- The contact model can describe substrates composed of layered structures and predict the adhesion pressure between each of the layers and another substrate, which is in contact with the surface of the layered substrate.
- Junction thermal conductance can be used to validate percentage contact area predictions. This was done by using the percentage contact prediction to compare experimental measurements and MD simulation predictions of junction thermal conductance for an Au-decanedithiol-Au system. It was also found that the Morse potential-based contact model provided a better match between experiment and simulation than an LJ potential-based model.

7.4. Collective behavior of molecules affecting thermal transport in SAMs

In Chapter 5, the effect of the cooperative behavior between molecules in a SAM junction on the thermal conductance was investigated. My key findings were:

- Cooperative effects between molecules leads to a non-linear change in thermal conductance as a function of the SAM configuration when transitioning from a fully dithiol to a fully monothiol setup. This was verified with both experimental measurements and computational predictions.
- The strength of the cooperative effect decreases as the average distance between the molecules increases, and is manifested in a lower per molecule thermal conductance. Thus, SAM structures cannot be used to make predictions of single molecule junctions and vice-versa.
- The origin of the cooperative effect in the SAM junctions is related to the stabilizing effect the dithiol molecules exhibit onto the monothiols thus increasing the effective strength of interaction between the terminal methyl end group and the gold surface.

7.5. Future outlook

The work presented in this thesis describes thermal transport in insulating SAM junctions and polymer systems. Some directions in which this work can be extended are:

7.5.1. *Energy transport in electrically conducting SAM junctions*

Conducting molecules having π -stacked electronic orbitals are being extensively studied for use in thermoelectrics^{12,158,170} and solar cells^{167,184,214}. However, no experimental and computational attempts have been made to measure their thermal conductance with metal leads, especially in periodic structures such as SAMs. The methods described in Chapters 2 and 3 can be used to study the thermal properties of SAM systems composed of conducting molecules, although requiring additional steps to include charge transport, electron-electron, and electron-

phonon interactions. The thermoelectric properties of such systems will also be interesting and can be compared to single-molecule measurements. These measurements will include measurement of the Seebeck coefficient and electrical conductance, which can in turn be used to estimate the power factor and figure of merit for such systems.

7.5.2. Temperature dependent thermal measurements of SAM junctions

Low temperature measurements of metal-SAM-metal junction thermal conductance have not yet been performed and will allow us to experimentally probe the scattering mechanisms in such mismatched SAM junctions. The slope of the junction thermal conductance v.s. temperature plot may provide insight into variations of the scattering rate of vibrations at the metal-SAM interfaces as the degree of vibrational mismatch is varied.

7.5.3. Nanocomposites with high- k nanoparticles and polymer brushes

The upper limit of thermal conductivity of nanocomposite particle-polymer brush systems, described in Chapter 6, may be improved by using nanoparticles having higher thermal conductivity than silica. MD simulations can be performed for such systems, albeit large computational resources will be required due to the complexity of the potentials and large number of atoms, to study the thermal transport. Simulations investigating the behavior of particle brushes on flat substrates with respect to their grafting density, extent of branching and average molecule length will also be useful in understanding their structure. Probing the interface thermal conductance between such brushes and a bulk polymer matrix using MD simulations can help answer the questions regarding the high thermal conductivities of the particle brush systems described in Chapter 6.

7.5.4. Specialized methyl-gold interatomic potential from first principles

The methyl-gold interatomic potential, used in Chapter 5, was not taken from the literature¹¹⁹ and was inadequate in describing the interaction of the gold surface with the methyl end groups, leading to under-prediction of the junction thermal conductance. Density functional theory, using hybrid functionals such as B3LYP,^{215,216} can be used to obtain a new empirical potential for the methyl-gold interaction. This will be a good foundation for other studies involving interactions between chemical groups at surfaces that interact only through van der Waals forces and do not form any covalent bonds.

8. Appendix

8.1. Generalized expressions to calculate r_e and A_2

Calculating r_e : We find a numerical fit for the variation of the ratio r_e/r_{NN} obtained from the single-point energy calculations for a range of values of αr_{NN} and r_0/r_{NN} to be

$$\frac{r_e}{r_{NN}} = C_1(\alpha r_{NN})^{C_2} + C_3 \quad \text{for } 3 \leq \alpha r_{NN} \leq 14, \quad (8.1.1)$$

where

$$\left. \begin{aligned} C_1 &= -1.373 \times 10^5 e^{-11.88 \left(\frac{r_0}{r_{NN}} \right)} - 13.32 e^{-1.078 \left(\frac{r_0}{r_{NN}} \right)} \\ C_2 &= 1.933 \left(\frac{r_0}{r_{NN}} \right)^5 - 9.226 \left(\frac{r_0}{r_{NN}} \right)^4 + 16.530 \left(\frac{r_0}{r_{NN}} \right)^3 \\ &\quad - 15.850 \left(\frac{r_0}{r_{NN}} \right)^2 + 12.000 \left(\frac{r_0}{r_{NN}} \right) - 8.558 \\ C_3 &= 1.138 \left(\frac{r_0}{r_{NN}} \right) - 0.328 \end{aligned} \right\} \text{for } 0.79 \leq \frac{r_0}{r_{NN}} \leq 1.96. \quad (8.1.2)$$

For our case, $r_{NN} = l_c/\sqrt{2}$, where l_c is the lattice constant. Eq. (8.1.1) has a maximum error of 8% with respect to the energy calculations for our chosen ranges of αr_{NN} and r_0/r_{NN} , which are sufficient to describe both covalent and van der Waals bonding characteristics. A plot indicating the quality of the fit is shown in Figure 8.1. The fits exhibit $R^2 > 0.85$ and consistently capture the behavior of r_e/r_{NN} for the chosen span of αr_{NN} and r_e/r_{NN} .

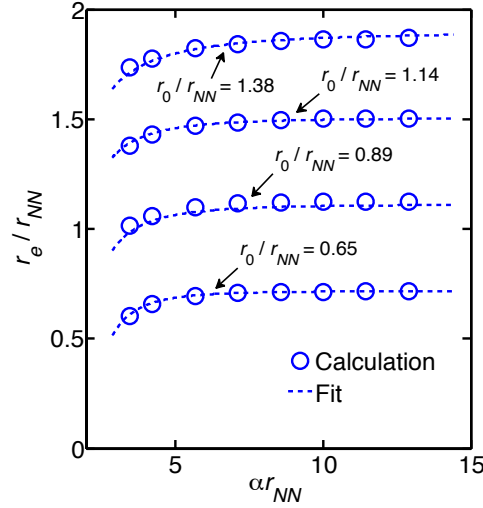


Figure 8.1. Variation of r_e/r_{NN} plotted as a function of αr_{NN} for specific values of r_0/r_{NN} from single-point energy calculations (open circles) and numerical fits (dashed lines).

Calculating A_2 : We find a numerical fit for the variation of the ratio $\Delta\gamma_M/\Delta\gamma_{LJ}$ obtained from the single-point energy calculations for a range of values of αr_{NN} and r_0/r_{NN} to be

$$\frac{\Delta\gamma_M}{\Delta\gamma_{LJ}} = E_1(\alpha r_{NN})^{E_2} + E_3 \quad \text{for } 3 \leq \alpha r_{NN} \leq 14, \quad (8.1.3)$$

where

$$\left. \begin{aligned} E_1 &= 204.10e^{-2.172\left(\frac{r_0}{r_{NN}}\right)} + 0.0504e^{1.796\left(\frac{r_0}{r_{NN}}\right)} \\ E_2 &= -0.3229\left(\frac{r_0}{r_{NN}}\right)^2 + 2.096\left(\frac{r_0}{r_{NN}}\right) - 4.49 \\ E_3 &= 0.3135\left(\frac{r_0}{r_{NN}}\right)^2 - 1.407\left(\frac{r_0}{r_{NN}}\right) + 1.683 \end{aligned} \right\} \quad \text{for } 0.79 \leq \frac{r_0}{r_{NN}} \leq 1.96. \quad (8.1.4)$$

Eq. (8.1.3) has a maximum error of 12% with respect to the energy calculations for our chosen ranges of αr_{NN} and r_0/r_{NN} . A plot indicating the quality of the fit is shown in Figure 8.2. The fits exhibit $R^2 > 0.99$ and consistently capture the behavior of $\Delta\gamma_M/\Delta\gamma_{LJ}$ for the chosen span of αr_{NN} and r_e/r_{NN} .

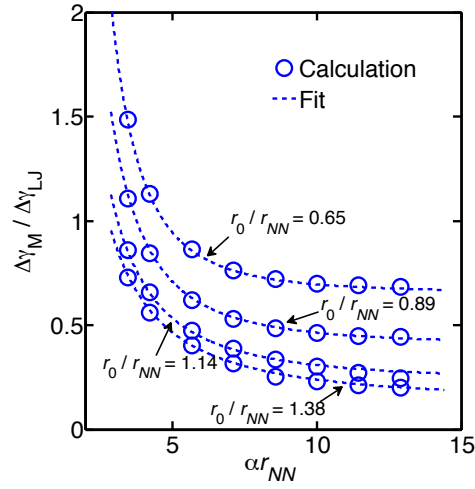


Figure 8.2. Variation of $\Delta\gamma_M/\Delta\gamma_{LJ}$ plotted as a function of αr_{NN} for specific values of r_0/r_{NN} from single-point energy calculations (open circles) and numerical fits (dashed lines).

8.2. Expression for critical interference and plasticity index

The critical interference is

$$\omega_c = \left(\frac{\pi KH}{2E} \right)^2 R, \quad (8.2.1)$$

where K is the hardness coefficient,⁷¹

$$K = 0.454 + 0.41\nu, \quad (8.2.2)$$

H is the Vickers hardness of the softer material, ν is the Poisson ratio of the softer material, E is the Hertz elastic modulus,

$$\frac{1}{E} = \frac{1 - \nu_1^2}{E_1} + \frac{1 - \nu_2^2}{E_2}, \quad (8.2.3)$$

E_1 and E_2 are the Young's moduli for the sphere and surface, and ν_1 and ν_2 are their Poisson ratios. The plasticity index Ψ is calculated as follows

$$\Psi = \frac{2E}{\pi KH} \left(\frac{\sigma_s}{R} \right)^{1/2}. \quad (8.2.4)$$

8.3. Plastic deformation regimes for composite asperities

For the deformation regimes where $\omega/\omega_c \geq 1$ (elastic-plastic regime), we adjust the FEA derived dimensionless separations found by Kogut and Etsion to be^{81,82}

$$\frac{Z(\omega, \bar{x})}{\omega_c} = \frac{0.951}{\pi} \left(\frac{\omega}{\omega_c}\right)^{1.153} f(\bar{x}) + \frac{r_e}{\omega_c} + \frac{t}{\omega_c} \quad \text{for } 1 \leq \omega/\omega_c \leq 6, \quad (8.3.1)$$

and

$$\frac{Z(\omega, \bar{x})}{\omega_c} = \frac{0.457}{\pi} \left(\frac{\omega}{\omega_c}\right)^{1.578} f(\bar{x}) + \frac{r_e}{\omega_c} + \frac{t}{\omega_c} \quad \text{for } 6 \leq \omega/\omega_c \leq 110. \quad (8.3.2)$$

8.4. Adhesive pressure and energy between a surface and a substrate for an LJ potential

The analogous expressions of Eqs. (4.9)-(4.10), (4.21), and (4.23), for describing adhesive pressure, energy per unit area, and work of adhesion between a single layer of atoms (surface) and a substrate interacting through an LJ potential are

$$P_{\text{LJ}, \text{surf-s}}(D) = \frac{\pi \rho_1 \sigma_2 (4\epsilon \sigma^6)}{2r_e^4} \left[\left(\frac{r_e}{D}\right)^{10} - \left(\frac{r_e}{D}\right)^4 \right], \quad (8.4.1)$$

$$E_{\text{LJ}, \text{surf-s}}''(D) = \frac{\pi \rho_1 \sigma_2 (4\epsilon \sigma^6)}{6r_e^3} \left[\frac{1}{3} \left(\frac{r_e}{D}\right)^9 - \left(\frac{r_e}{D}\right)^3 \right], \quad (8.4.2)$$

$$\frac{F_c^{ad}(\omega)}{F_0^{ad}} = \frac{9(\omega/\omega_c)}{2(r_e/\omega_c)} \int_1^\infty \left[\left(\frac{r_e/\omega_c}{Z/\omega_c}\right)^4 - \left(\frac{r_e/\omega_c}{Z/\omega_c}\right)^{10} \right] \bar{x} d\bar{x}, \quad (8.4.3)$$

$$\frac{F_{nc}^{ad}(D)}{F_0^{ad}} = \frac{3}{2} \left[\left(\frac{r_e}{D}\right)^3 - \frac{1}{3} \left(\frac{r_e}{D}\right)^9 \right]. \quad (8.4.4)$$

8.5. Contact stress and contact area

The total non-dimensional contact stress P_{cs}^* and the percentage contact area A^* between deforming asperities and the surface are given by⁸¹

$$P_{cs}^* = \frac{P_{cs}}{A_n H} = \frac{2\pi\eta R \sigma_h K \omega_c^*}{3} \left(\int_{d^*}^{d^* + \omega_c^*} I^{1.5} + 1.03 \int_{d^* + \omega_c^*}^{d^* + 6\omega_c^*} I^{1.425} \right. \\ \left. + 1.4 \int_{d^* + 6\omega_c^*}^{d^* + 110\omega_c^*} I^{1.263} + \frac{3}{K} \int_{d^* + 110\omega_c^*}^{\infty} I^1 \right), \quad (8.5.1)$$

and

$$A^* = \frac{A}{A_n} = \pi\eta R \sigma_h \omega_c^* \left(\int_{d^*}^{d^* + \omega_c^*} I^1 + 0.93 \int_{d^* + \omega_c^*}^{d^* + 6\omega_c^*} I^{1.136} \right. \\ \left. + 0.94 \int_{d^* + 6\omega_c^*}^{d^* + 110\omega_c^*} I^{1.146} + 2 \int_{d^* + 110\omega_c^*}^{\infty} I^1 \right), \quad (8.5.2)$$

where

$$I^\alpha = \left(\frac{z^* - d^*}{\omega_c^*} \right)^\alpha \phi^*(z^*) dz^* \quad (8.5.3)$$

8.6. Sensitivity analysis of the Morse contact model

The sensitivity of our model to topographical features is performed by calculating the variation of the predicted percentage contact area with respect to the variation of the parameters that affect σ_h , radius of asperity R , and areal asperity density η . From Eqs. (4.27)-(4.30) in the main text, it is clear that R and η are not independent parameters, as both depend on the second derivative of surface heights, $d^2\xi/dx^2$. Thus, we perform our sensitivity analysis with respect to the independent parameters in Eqs. (4.27)-(4.30), which are the individual surface heights (ξ) and the derivatives $d\xi/dx$ and $d^2\xi/dx^2$. In Fig. S4, the relative change in percentage contact

area is plotted as ξ , $d\xi/dx$, and $d^2\xi/dx^2$ are separately varied by $\pm 10\%$, $\pm 20\%$, $\pm 30\%$, $\pm 40\%$ and $\pm 50\%$.

The percentage contact area is most sensitive to ξ and $d\xi/dx$. ξ is a measure of RMS surface roughness and $d\xi/dx$ affects only the areal asperity density. To obtain practical uncertainties in the predicted percentage contact area, we use the AFM measurements to generate limits in the sensitivity analysis. From Table 4.5, the variation in σ_h across all scans is 25%, 58% for R , and 59% for η . As seen from Eqs. (4.30), (8.5.1) and (8.5.2), R and η always appear as a product. The variation of $R\eta$ is only 30%, comparable to the variation in σ_h . Thus, a conservative estimate of the uncertainty in the roughness parameters for a particular AFM measurement can be set at 30%. This uncertainty is subject to change based on sample preparation techniques and the value reported here is accurate for our samples. From Figure 8.3, the estimate of uncertainty in percentage contact area for a 30% uncertainty in roughness parameters is 35%.

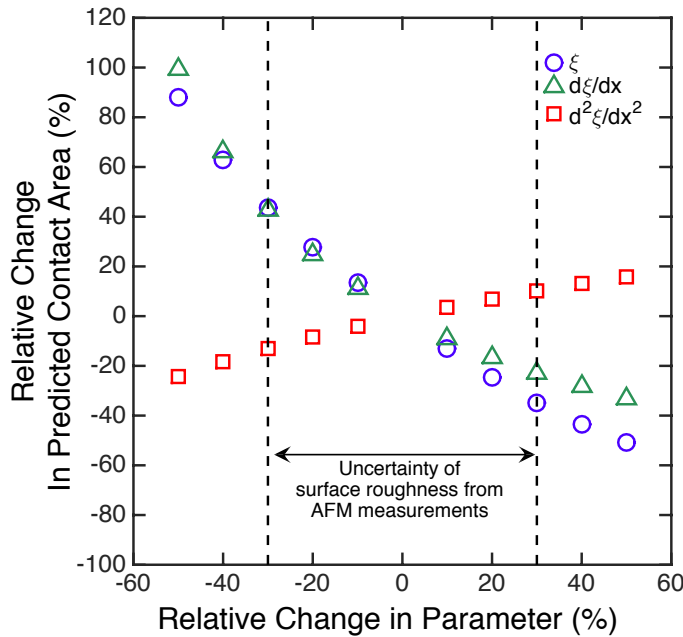


Figure 8.3. Sensitivity analysis showing variation of percentage contact area predicted using the Morse potential-based contact model with respect to relative change of the independent parameters ξ , $d\xi/dx$, and $d^2\xi/dx^2$. The nominal values for all parameters are taken from Table 4.1.

8.7. Uncertainty analysis of area-corrected thermal conductance

The uncertainty of Eq. (32) in the manuscript is obtained from

$$\Delta G_{M/LJ}^{int} = \left[\left(\frac{\partial G_{M/LJ}^{int}}{\partial k_H} \right)^2 \Delta k_H^2 + \left(\frac{\partial G_{M/LJ}^{int}}{\partial G_{exp}} \right)^2 \Delta G_{exp}^2 + \left(\frac{\partial G_{M/LJ}^{int}}{\partial A^*} \right)^2 \Delta A_{M/LJ}^{*2} \right]^{\frac{1}{2}}, \quad (8.7.1)$$

which evaluates to

$$\Delta G_{M/LJ}^{int} = \frac{G_{M/LJ}^{int2}}{\left(\eta \int_{d^*}^{\infty} \phi^*(z^*) dz^* \right)^2} \left[\frac{(1-\sqrt{A^*})^3}{4k_H^4 a_R^2} \Delta k_H^2 + \frac{1}{\pi^2 a_R^4 G_{MD}^{int4}} \Delta G_{MD}^{int2} + \frac{(1-\sqrt{A_{M/LJ}^*}) b_R^2}{16k_H^2 a_R^2} \left(\frac{1-\sqrt{A_{M/LJ}^*}}{A_{M/LJ}^*} + \frac{3}{\sqrt{A_{M/LJ}^*}} \right)^2 \Delta A_{M/LJ}^{*2} \right]^{\frac{1}{2}}, \quad (8.7.2)$$

where, $b_R = \left[\pi \eta \int_{d^*}^{\infty} \phi^*(z^*) dz^* \right]^{0.5}$, $\Delta k_H = 2 \text{ W/m-K}$, $\Delta G_{MD}^{int} = 9 \text{ MW/m}^2\text{-K}$ and $\Delta A_{M/LJ}^* = 35\%$

for the study conducted by Majumdar *et al.*¹⁰⁰

9. Bibliography

- (1) Xu, B.; Tao, N. J. *Science* **2003**, *301*, 1221–1223.
- (2) Joachim, C.; Gimzewski, J. K.; Aviram, A. *Nature* **2000**, *408*, 541–548.
- (3) Nitzan, A.; Ratner, M. A. *Science* **2003**, *300*, 1384–1389.
- (4) Heath, J. R.; Ratner, M. A. *Phys. Today* **2003**, *56*, 43.
- (5) Luo, Y.; Collier, P. C.; Jeppesen, J. O.; Nielsen, K. A.; Delonno, E.; Ho, G.; Perkins, J.; Tseng, H.-R.; Yamamoto, T.; Stoddart, J. F.; Heath, J. R. *Chemphyschem* **2002**, *3*, 519–525.
- (6) Aswal, D. K.; Lenfant, S.; Guerin, D.; Yakhmi, J. V.; Vuillaume, D. *Anal. Chim. Acta* **2006**, *568*, 84–108.
- (7) Colvin, V. L.; Schlamp, M. C.; Alivisatos, A. P. *Nature* **1994**, *370*, 354–357.
- (8) Gather, M. C.; Köhnen, A.; Meerholz, K. *Adv. Mater.* **2011**, *23*, 233–248.
- (9) Tang, J.; Kemp, K. W.; Hoogland, S.; Jeong, K. S.; Liu, H.; Levina, L.; Furukawa, M.; Wang, X.; Debnath, R.; Cha, D.; Chou, K. W.; Fischer, A.; Amassian, A.; Asbury, J. B.; Sargent, E. H. *Nat. Mater.* **2011**, *10*, 765–771.
- (10) Ip, A. H.; Thon, S. M.; Hoogland, S.; Voznyy, O.; Zhitomirsky, D.; Debnath, R.; Levina, L.; Rollny, L. R.; Carey, G. H.; Fischer, A.; Kemp, K. W.; Kramer, I. J.; Ning, Z.; Labelle, A. J.; Chou, K. W.; Amassian, A.; Sargent, E. H. *Nat. Nanotechnol.* **2012**, *7*, 577–582.
- (11) Weickert, J.; Dunbar, R. B.; Hesse, H. C.; Wiedemann, W.; Schmidt-Mende, L. *Adv. Mater.* **2011**, *23*, 1810–1828.
- (12) Reddy, P.; Jang, S. Y.; Segalman, R. A.; Majumdar, A. *Science* **2007**, *315*, 1568–1571.
- (13) Baheti, K.; Malen, J. A.; Doak, P.; Reddy, P.; Jang, S. Y.; Tilley, T. D.; Majumdar, A.; Segalman, R. A. *Nano Lett.* **2008**, *8*, 715–719.

- (14) Malen, J. A.; Doak, P.; Baheti, K.; Tilley, T. D.; Majumdar, A.; Segalman, R. A. *Nano Lett.* **2009**, *9*, 3406–3412.
- (15) Malen, J. A.; Doak, P.; Baheti, K.; Tilley, T. D.; Segalman, R. A.; Majumdar, A. *Nano Lett.* **2009**, *9*, 1164–1169.
- (16) Jang, S. Y.; Reddy, P.; Majumdar, A.; Segalman, R. A. *Nano Lett.* **2006**, *6*, 2362–2367.
- (17) Lee, W.; Reddy, P. *Nanotechnology* **2011**, *22*, 1–8.
- (18) See, K. C.; Feser, J. P.; Chen, C. E.; Majumdar, A.; Urban, J. J.; Segalman, R. A. *Nano Lett.* **2010**, *10*, 4664–4667.
- (19) Reiss, P.; Couderc, E.; De Girolamo, J.; Pron, A. *Nanoscale* **2011**, *3*, 446–489.
- (20) Garimella, S. V. *Microelectronics J.* **2006**, *37*, 1165–1185.
- (21) Lee, W.; Kim, K.; Jeong, W.; Zotti, L. A.; Pauly, F.; Cuevas, J. C.; Reddy, P. *Nature* **2013**, *498*, 209–212.
- (22) Wang, Z.; Carter, J. A.; Lagutchev, A.; Koh, Y. K.; Seong, N.-H.; Cahill, D. G.; Dlott, D. D. *Science* **2007**, *317*, 787–790.
- (23) Ong, W.-L.; Rupich, S. M.; Talapin, D. V.; McGaughey, A. J. H.; Malen, J. A. *Nat. Mater.* **2013**, *12*, 410–415.
- (24) Ong, W.-L.; Majumdar, S.; Malen, J. A.; McGaughey, A. J. H. *J. Phys. Chem. C* **2014**, *118*, 7288–7295.
- (25) Linford, M. R.; Chidsey, C. E. D. *J. Am. Chem. Soc.* **1993**, *115*, 12631–12632.
- (26) Jun, Y.; Zhu, X. Y.; Hsu, J. W. P. *Langmuir* **2006**, *22*, 3627–3632.
- (27) Bain, C. D.; Troughton, E. B.; Tao, Y.-T.; Whitesides, J. E. G. M.; Nuzzo, R. G. *J. Am. Chem. Soc.* **1989**, *111*, 321–335.

- (28) Laibinis, P.; Whitesides, G. *J. Am. Chem. Soc.* **1991**, *113*, 7152–7167.
- (29) Nuzzo, R. G.; Allara, D. L. *J. Am. Chem. Soc.* **1983**, *105*, 4481–4483.
- (30) Porter, M. D.; Bright, T. B.; Allara, D. L.; Chidsey, C. E. D. *J. Am. Chem. Soc.* **1987**, *109*, 3559–3568.
- (31) Fenter, P.; Eisenberger, P.; Li, J.; Camillone III, N.; Bernasek, S.; Scoles, G.; Ramanarayanan, T. A.; Liang, K. S. *Langmuir* **1991**, *7*, 2013–2016.
- (32) Love, J. C.; Estroff, L. A.; Kriebel, J. K.; Nuzzo, R. G.; Whitesides, G. M. *Chem. Rev.* **2005**, *105*, 1103–1169.
- (33) Finklea, H. O. *Electroanal. Chem.* **1996**, *19*, 109–335.
- (34) Hautman, J.; Klein, M. L. *J. Chem. Phys.* **1989**, *91*, 4994–5001.
- (35) Dubois, L. H.; Nuzzo, R. G. *Annu. Rev. Phys. Chem.* **1992**, *43*, 437–463.
- (36) Schreiber, F. *J. Phys. Condens. Matter* **2004**, *16*, 881–900.
- (37) Vericat, C.; Vela, M. E.; Benitez, G.; Carro, P.; Salvarezza, R. C. *Chem. Soc. Rev.* **2010**, *39*, 1805–1834.
- (38) Rouhana, L. L.; Moussallem, M. D.; Schlenoff, J. B. *J. Am. Chem. Soc.* **2011**, *133*, 16080–16091.
- (39) Engelkes, V. B.; Beebe, J. M.; Frisbie, C. D. *J. Am. Chem. Soc.* **2004**, *126*, 14287–14296.
- (40) Xu, B.; Tao, N. J. *Science* **2003**, *301*, 1221–1223.
- (41) Venkataraman, L.; Klare, J. E.; Tam, I. W.; Nuckolls, C.; Hybertsen, M. S.; Steigerwald, M. L. *Nano Lett.* **2006**, *6*, 458–462.
- (42) Engelkes, V. B.; Beebe, J. M.; Frisbie, C. D. *J. Phys. Chem. B* **2005**, *109*, 16801–16810.

- (43) Loo, Y. L.; Lang, D. V.; Rogers, J. A.; Hsu, J. W. P. *Nano Lett.* **2003**, *3*, 913–917.
- (44) Holmlin, R. E.; Haag, R.; Chabinyo, M. L.; Ismagilov, R. F.; Cohen, A. E.; Terfort, A.; Rampi, M. A.; Whitesides, G. M. *J. Am. Chem. Soc.* **2001**, *123*, 5075–5085.
- (45) Chiechi, R. C.; Weiss, E. A.; Dickey, M. D.; Whitesides, G. M. *Angew. Chemie - Int. Ed.* **2008**, *47*, 142–144.
- (46) Malen, J. A.; Yee, S. K.; Majumdar, A.; Segalman, R. A. *Chem. Phys. Lett.* **2010**, *491*, 109–122.
- (47) Wold, D. J.; Haag, R.; Rampi, M. A.; Frisbie, C. D. *J. Phys. Chem. B* **2002**, *106*, 2813–2816.
- (48) Wang, R. Y.; Segalman, R. A.; Majumdar, A. *Appl. Phys. Lett.* **2006**, *89*, 173113.
- (49) Meier, T.; Menges, F.; Nirmalraj, P.; Hölscher, H.; Riel, H.; Gotsmann, B. *Phys. Rev. Lett.* **2014**, *113*, 60801.
- (50) Losego, M. D.; Grady, M. E.; Sottos, N. R.; Cahill, D. G.; Braun, P. V. *Nat. Mater.* **2012**, *11*, 502–506.
- (51) O'Brien, P. J.; Shenogin, S.; Liu, J.; Chow, P. K.; Laurencin, D.; Mutin, P. H.; Yamaguchi, M.; Keblinski, P.; Ramanath, G. *Nat. Mater.* **2012**, *12*, 118–122.
- (52) Segal, D.; Nitzan, A.; Hänggi, P. *J. Chem. Phys.* **2003**, *119*, 6840 1–16.
- (53) Hu, L.; Zhang, L.; Hu, M.; Wang, J.-S.; Li, B.; Keblinski, P. *Phys. Rev. B* **2010**, *81*, 235427.
- (54) Luo, T.; Lloyd, J. R. *J. Appl. Phys.* **2011**, *109*, 034301.
- (55) Sun, F.; Zhang, T.; Jobbins, M. M.; Guo, Z.; Zhang, X.; Zheng, Z.; Tang, D.; Ptasińska, S.; Luo, T. *Adv. Mater.* **2014**, *26*, 6093–6099.

- (56) Luo, T.; Lloyd, J. R. *Int. J. Heat Mass Transfer* **2010**, *53*, 1–11.
- (57) Carpick, R. W.; Ogletree, D. F.; Salmeron, M. *J. Colloid Interface Sci.* **1999**, *211*, 395–400.
- (58) Higgs, C. F.; Ng, S. H.; Borucki, L.; Yoon, I.; Danyluk, S. *J. Electrochem. Soc.* **2005**, *152*, G193–G198.
- (59) Krick, B. A.; Vail, J. R.; Persson, B. N. J.; Sawyer, W. G. *Tribol. Lett.* **2012**, *45*, 185–194.
- (60) Johnson, P. M.; Stafford, C. M. *ACS Appl. Mater. Interfaces* **2010**, *2*, 2108–2115.
- (61) Greiner, C.; Schäfer, M.; Popp, U.; Gumbsch, P. *ACS Appl. Mater. Interfaces* **2014**, *6*, 7986–7990.
- (62) Greenwood, J. A.; Williamson, J. B. P. *Proc. R. Soc. London. Ser. A. Math. Phys. Sci.* **1966**, *295*, 300–319.
- (63) Hertz, H. *J. für die reine und Angew. Math.* **1882**, *92*, 156–171.
- (64) Kogut, L.; Etsion, I. *J. Appl. Mech.* **2002**, *69*, 657–662.
- (65) Chang, W.-R.; Etsion, I.; Bogy, D. B. *J. Tribol.* **1988**, *110*, 50–56.
- (66) Francis, H. A. *Wear* **1977**, *45*, 221–269.
- (67) Ishigaki, H.; Kawaguchi, I.; Mizuta, S. *Wear* **1979**, *54*, 157–164.
- (68) Fuller, K. N. G.; Tabor, D. *Proc. R. Soc. A* **1975**, *345*, 327–342.
- (69) Roy Chowdhury, S. K.; Pollock, H. M. *Wear* **1981**, *66*, 307–321.
- (70) Chang, W. R.; Etsion, I.; Bogy, D. B. *J. Tribol.* **1988**, *110*, 57–63.
- (71) Chang, W. R.; Etsion, I.; Bogy, D. B. *J. Tribol.* **1987**, *109*, 257–263.

- (72) Derjaguin, B. .; Muller, V. .; Toporov, Y. . *J. Colloid Interface Sci.* **1975**, 53, 314–326.
- (73) Johnson, K. L.; Kendall, K.; Roberts, A. D. *Proc. R. Soc. A* **1971**, 324, 301–313.
- (74) Tabor, D. *J. Colloid Interface Sci.* **1977**, 58, 2–13.
- (75) Maugis, D. *J. Colloid Interface Sci.* **1992**, 150, 243–269.
- (76) Jones, J. E. *Proc. R. Soc. A* **1924**, 106, 463–477.
- (77) Muller, V. .; Yushchenko, V. .; Derjaguin, B. . *J. Colloid Interface Sci.* **1980**, 77, 91–101.
- (78) Johnson, K. L.; Greenwood, J. A. *J. Colloid Interface Sci.* **1997**, 192, 326–333.
- (79) Liu, Z.; Neville, A.; Reuben, R. L. *J. Tribol.* **2002**, 124, 27–35.
- (80) Polycarpou, A. A.; Etsion, I. *J. Tribol.* **1998**, 120, 296–303.
- (81) Kogut, L.; Etsion, I. *Tribol. Trans.* **2003**, 46, 383–390.
- (82) Kogut, L.; Etsion, I. *J. Colloid Interface Sci.* **2003**, 261, 372–378.
- (83) Kogut, L.; Etsion, I. *J. Tribol.* **2004**, 126, 34–40.
- (84) Jensen, F. *Introduction to Computational Chemistry*; John Wiley and Sons, 2007; Vol. 2.
- (85) Malen, J. A.; Baheti, K.; Tong, T.; Zhao, Y.; Hudgings, J. A.; Majumdar, A. *J. Heat Transfer* **2011**, 133, 081601.
- (86) Regner, K. T.; Majumdar, S.; Malen, J. A. *Rev. Sci. Instrum.* **2013**, 84, 064901.
- (87) Cahill, D. G. *Rev. Sci. Instrum.* **2004**, 75, 5119.
- (88) Blackstock, J. J.; Li, Z.; Freeman, M. R.; Stewart, D. R. *Surf. Sci.* **2003**, 546, 87–96.

- (89) Weiss, E. A.; Kaufman, G. K.; Kriebel, J. K.; Li, Z.; Schalek, R.; Whitesides, G. M. *Langmuir* **2007**, *23*, 9686–9694.
- (90) Meitl, M. A.; Zhu, Z.-T.; Kumar, V.; Lee, K. J.; Feng, X.; Huang, Y. Y.; Adesida, I.; Nuzzo, R. G.; Rogers, J. A. *Nat. Mater.* **2006**, *5*, 33–38.
- (91) Zhao, X.-M.; Xia, Y.; Whitesides, G. M. *J. Mater. Chem.* **1997**, *7*, 1069–1074.
- (92) Kim, J. W.; Yang, K. Y.; Hong, S. H.; Lee, H. *Appl. Surf. Sci.* **2008**, *254*, 5607–5611.
- (93) Henry, A.; Chen, G. *Phys. Rev. Lett.* **2008**, *101*, 1–4.
- (94) Jang, S. Y.; Reddy, P.; Majumdar, A.; Segalman, R. A. *Nano Lett.* **2006**, *6*, 2362–2367.
- (95) Luo, T.; Lloyd, J. *J. Heat Transfer* **2010**, *132*, 032401.
- (96) Zhang, L.; Goddard, W. A.; Jiang, S. *J. Chem. Phys.* **2002**, *117*, 7342–7349.
- (97) Sung, I. H.; Kim, D. E. *Appl. Phys. A Mater. Sci. Process.* **2005**, *81*, 109–114.
- (98) Mahaffy, R.; Bhatia, R.; Garrison, B. J. *J. Phys. Chem. B* **1997**, *101*, 771–773.
- (99) Thomas, J. A.; McGaughey, A. J. H. *Phys. Rev. Lett.* **2009**, *102*.
- (100) Majumdar, S.; Sierra-Suarez, J. A.; Schiffres, S. N.; Ong, W.-L.; Higgs III, C. F.; McGaughey, A. J. H.; Malen, J. A. *Nano Lett.* **2015**, *15*, 2985–2991.
- (101) Sierra-Suarez, J. A.; Majumdar, S.; McGaughey, A. J. H.; Malen, J. A.; Higgs III, C. F. *J. Appl. Phys.* **2016**, *119*, 145306.
- (102) Hegner, M.; Wagner, P.; Semenza, G. *Surf. Sci. Lett.* **1993**, *291*, 39–46.
- (103) Hutt, D.; Cooper, E.; Leggett, G. *J. Phys. Chem. B* **1998**, *5647*, 174–184.
- (104) Kittel, C.; McEuen, P. *Introduction to Solid State Physics*; 8th ed.; Wiley: New York, 1976; Vol. 19.

- (105) Bergman, T. L.; Lavigne, A. S.; Incropera, F. P.; Dewitt, D. P. *Fundamentals of Heat and Mass Transfer*; 2011.
- (106) Widrig, C. A.; Alves, C. A.; Porter, M. D. *J. Am. Chem. Soc.* **1991**, *113*, 2805–2810.
- (107) Lee, S.; Park, J.; Ragan, R.; Kim, S.; Lee, Z.; Lim, D. K.; Ohlberg, D. A. A.; Williams, R. S. *J. Am. Chem. Soc.* **2006**, *128*, 5745–5750.
- (108) Christopher Love, J.; Wolfe, D. B.; Haasch, R.; Chabinyc, M. L.; Paul, K. E.; Whitesides, G. M.; Nuzzo, R. G. *J. Am. Chem. Soc.* **2003**, *125*, 2597–2609.
- (109) Akkerman, H. B.; de Boer, B. *J. Phys. Condens. Matter* **2008**, *20*, 013001.
- (110) Duda, J. C.; Saltonstall, C. B.; Norris, P. M.; Hopkins, P. E. *J. Chem. Phys.* **2011**, *134*, 1–6.
- (111) Duda, J. C.; Beechem, T. E.; Smoyer, J. L.; Norris, P. M.; Hopkins, P. E. *J. Appl. Phys.* **2010**, *108*.
- (112) We note that the prediction by Luo and Lloyd is higher than our MD result. We believe this discrepancy to be primarily due to their use of a Morse potential to calculate the vibrational properties of the Au leads. We use an EAM potential that better reproduces the experimentally measured dispersion of Au than the Morse potential.
- (113) Greenwood, J. A.; Tripp, J. H. *Proc. Inst. Mech. Eng.* **1970**, *185*, 625–633.
- (114) Muller, V. M.; Derjaguin, B. V.; Toporov, Y. P. *Colloids Surf.* **1983**, *7*, 251–259.
- (115) Seong, M.; Singh, P. K.; Sinha, S. *J. Appl. Phys.* **2013**, *113*, 024321.
- (116) Prasher, R. S.; Phelan, P. E. *J. Appl. Phys.* **2006**, *100*, 063538.
- (117) Plimpton, S. *J. Comput. Phys.* **1995**, *117*, 1–19.

- (118) Adams, J. B.; Foiles, S. M.; Wolfer, W. G. *J. Mater. Res.* **1989**, *4*, 102–112.
- (119) Hautman, J.; Klein, M. L. *J. Chem. Phys.* **1989**, *91*, 4994–5001.
- (120) Ryckaert, J.-P.; Bellemans, A. *J. Chem. Society Faraday Discuss.* **1978**, *66*, 95–107.
- (121) Gale, J. D. *J. Chem. Soc. Faraday Trans.* **1997**, *93*, 629–637.
- (122) Lide, D. R. *CRC handbook of chemistry and physics*; CRC press, 2004.
- (123) Van Krevelen, D. W.; Te Nijenhuis, K. *Properties of polymers: their correlation with chemical structure; their numerical estimation and prediction from additive group contributions*; Elsevier, 2009.
- (124) Swartz, E. T.; Pohl, R. O. *Rev. Mod. Phys.* **1989**, *61*, 605–668.
- (125) Morse, P. M. *Phys. Rev.* **1929**, *34*, 57–64.
- (126) Girifalco, L. A.; Weizer, V. G. *Phys. Rev.* **1959**, *114*, 687–690.
- (127) Rappe, A. K.; Casewit, C. J.; Colwell, K. S.; Goddard III, W. A.; Skiff, W. M. *J. Am. Chem. Soc.* **1992**, *114*, 10024–10035.
- (128) Tersoff, J. *Phys. Rev. Lett.* **1986**, *56*, 632–635.
- (129) Qian, D.; Liu, W. K.; Ruoff, R. S. *J. Phys. Chem. B* **2001**, *105*, 10753–10758.
- (130) Wang, Y.; Tomnek, D.; Bertsch, G. F. *Phys. Rev. B* **1991**, *44*, 6562–6565.
- (131) Costa Filho, R. N.; Alencar, G.; Skagerstam, B.-S.; Andrade, J. S. *Europhys. Lett.* **2013**, *101*, 10009.
- (132) Fang, T. H.; Weng, C. I. *Nanotechnology* **2000**, *11*, 148–153.
- (133) Weymouth, A. J.; Hofmann, T.; Giessibl, F. J. *Science* **2014**, *343*, 1120–1122.

- (134) Samsonov, G. V. In *Handbook of the Physicochemical Properties of the Elements*; Samsonov, G. V, Ed.; Springer US: Boston, MA, 1968; pp. 387–446.
- (135) Muller, V. M.; Yushchenko, V. S.; Derjaguin, B. V. *J. Colloid Interface Sci.* **1983**, *92*, 92–101.
- (136) Johnson, K. L. *Contact mechanics*; Cambridge university press, 1987.
- (137) Webster, M. N.; Sayles, R. S. *J. Tribol.* **1986**, *108*, 314–320.
- (138) Pödra, P.; Andersson, S. *Wear* **1997**, *207*, 79–85.
- (139) Bhushan, B. *Tribol. Lett.* **1998**, *4*, 1–35.
- (140) Ai, X.; Sawamiphakdi, K. *J. Tribol.* **1999**, *121*, 639–647.
- (141) Polonsky, I.; Keer, L. *J. Tribol.* **2000**, *122*, 30–35.
- (142) Nogi, T.; Kato, T. *J. Tribol.* **1997**, *119*, 493–500.
- (143) Hu, Y. Y.-Z.; Barber, G. C.; Zhu, D. *Tribol. Trans.* **1999**, *42*, 443–452.
- (144) Delrio, F. W.; Jaye, C.; Fischer, D. A.; Cook, R. F. *Appl. Phys. Lett.* **2009**, *94*, 1–3.
- (145) Bush, A. W.; Gibson, R. D.; Keogh, G. P. *J. Lubr. Technol.* **1979**, *101*, 15–20.
- (146) Gibson, R. D. In *Rough Surfaces*; Thomas, T. R., Ed.; Longman: New York, 1982; pp. 119–143.
- (147) McCool, J. I. *Wear* **1986**, *107*, 37–60.
- (148) Nayak, P. R. *J. Lubr. Technol.* **1971**, *93*, 398–407.
- (149) Longuet-Higgins, M. S. *Philos. Trans. R. Soc., A* **1957**, *250*, 157–174.

- (150) Kotwal, C. A.; Bhushan, B. *Tribol. Trans.* **1996**, *39*, 890–898.
- (151) Bora, C. K.; Flater, E. E.; Street, M. D.; Redmond, J. M.; Starr, M. J.; Carpick, R. W.; Plesha, M. E. *Tribol. Lett.* **2005**, *19*, 37–48.
- (152) You, S.; Wan, M. P. *Langmuir* **2013**, *29*, 9104–9117.
- (153) Greenwood, J. A. *Proc. R. Soc. A* **1984**, *393*, 133–157.
- (154) Poon, C. Y.; Bhushan, B. *Wear* **1995**, *190*, 76–88.
- (155) Xia, Y.; Zhao, X.-M.; Whitesides, G. M. *Microelectron. Eng.* **1996**, *32*, 255–268.
- (156) Geissler, M.; Schmid, H.; Bietsch, A.; Michel, B.; Delamarche, E. *Langmuir* **2002**, *18*, 2374–2377.
- (157) Adams, D. M.; Brus, L.; Chidsey, C. E. D.; Creager, S.; Creutz, C.; Kagan, C. R.; Kamat, P. V.; Lieberman, M.; Lindsay, S.; Marcus, R. A.; Metzger, R. M.; Michel-Beyerle, M. E.; Miller, J. R.; Newton, M. D.; Rolison, D. R.; Sankey, O.; Schanze, K. S.; Yardley, J.; Zhu, X. *J. Phys. Chem. B* **2003**, *107*, 6668–6697.
- (158) Yee, S. K.; Malen, J. A.; Majumdar, A.; Segalman, R. A. *Nano Lett.* **2011**, *11*, 4089–4094.
- (159) Cai, L. T.; Skulason, H.; Kushmerick, J. G.; Pollack, S. K.; Naciri, J.; Shashidhar, R.; Allara, D. L.; Mallouk, T. E.; Mayer, T. S. *J. Phys. Chem. B* **2004**, *108*, 2827–2832.
- (160) This value differs from the percentage contact area reported by Majumdar *et al.* (Ref. 100) after further refinement of our model and averaging of more AFM measurements.
- (161) Inman, H. F.; Bradley, E. L. *Commun. Stat. Theor. M* **1989**, *18*, 3851–3874.
- (162) This value differs from the area-corrected junction thermal conductance reported by Majumdar *et al.* (Ref. 100) after further refinement of our model and averaging of more AFM measurements.

- (163) Cui, X. D.; Primak, A.; Zarate, X.; Tomfohr, J.; Sankey, O. F.; Moore, A. L.; Moore, T. A.; Gust, D.; Harris, G.; Lindsay, S. M. *Science* **2001**, *294*, 571–574.
- (164) Guerin, D.; Merckling, C.; Lenfant, S.; Wallart, X.; Pleutin, S.; Vuillaume, D. *J. Phys. Chem. C* **2007**, *111*, 7947–7956.
- (165) Salomon, A.; Cahen, D.; Lindsay, S.; Tomfohr, J.; Engelkes, V. B.; Frisbie, C. D. *Adv. Mater.* **2003**, *15*, 1881–1890.
- (166) Nitzan, A.; Ratner, M. A. *Science* **2003**, *300*, 1384–1389.
- (167) Yang, Q.; Liu, Y.; Pan, C.; Chen, J.; Wen, X.; Wang, Z. L. *Nano Lett.* **2013**, *13*, 607–613.
- (168) Cui, Y.; Song, T.; Yu, J.; Yang, Y.; Wang, Z.; Qian, G. *Adv. Funct. Mater.* **2015**, *25*, 4796–4802.
- (169) Widawsky, J. R.; Chen, W.; Vázquez, H.; Kim, T.; Breslow, R.; Hybertsen, M. S.; Venkataraman, L. *Nano Lett.* **2013**, *13*, 2889–2894.
- (170) Rincon-Garcia, L.; Ismael, A. K.; Evangeli, C.; Grace, I.; Rubio-Bollinger, G.; Porfyrakis, K.; Agrait, N.; Lambert, C. J. *Nat Mater* **2016**, *15*, 289–293.
- (171) Selzer, Y.; Cai, L.; Cabassi, M. A.; Yao, Y.; Tour, J. M.; Mayer, T. S.; Allara, D. L. *Nano Lett.* **2005**, *5*, 61–65.
- (172) Nerngchamnong, N.; Yuan, L.; Qi, D.-C.; Li, J.; Thompson, D.; Nijhuis, C. a. *Nat. Nanotechnol.* **2013**, *8*, 113–118.
- (173) Reuter, M. G.; Seideman, T.; Ratner, M. A. *Nano Lett.* **2011**, *11*, 4693–4696.
- (174) Dubi, Y. *J. Phys. Chem. C* **2014**, *118*, 21119–21127.
- (175) Obersteiner, V.; Egger, D. A.; Zojer, E. *J. Phys. Chem. C* **2015**, *119*, 21198–21208.
- (176) Obersteiner, V.; Egger, D. A.; Heimel, G.; Zojer, E. *J. Phys. Chem. C* **2014**, *118*, 22395–22401.

- (177) Offord, D. A.; Griffin, J. H. *Langmuir* **1993**, *9*, 3015–3025.
- (178) Offord, D. A.; John, C. M.; Linford, M. R.; Griffin, J. H. *Langmuir* **1994**, *10*, 883–889.
- (179) Gaskins, J. T.; Bulusu, A.; Giordano, A. J.; Duda, J. C.; Graham, S.; Hopkins, P. E. *J. Phys. Chem. C* **2015**, *119*, 20931–20939.
- (180) Sasikumar, K.; Koblinski, P. *J. Appl. Phys.* **2011**, *109*, 114307 1–6.
- (181) Harikrishna, H.; Ducker, W. A.; Huxtable, S. T. *Appl. Phys. Lett.* **2013**, *102*, 251606.
- (182) Chidsey, C. E. D.; Bertozzi, C. R.; Putvinski, T. M.; Mucic, M. *J. Am. Chem. Soc.* **1990**, *112*, 4301–4306.
- (183) Lu, X.; Xu, G. *J. Appl. Polym. Sci.* **1997**, *65*, 2733–2738.
- (184) Ren, S.; Chang, L.-Y.; Lim, S.-K.; Zhao, J.; Smith, M.; Zhao, N.; Bulović, V.; Bawendi, M.; Gradecak, S. *Nano Lett.* **2011**, *11*, 3998–4002.
- (185) Shen, S.; Henry, A.; Tong, J.; Zheng, R. T.; Chen, G. *Nat. Nanotechnol.* **2010**, *5*, 251–255.
- (186) Moniruzzaman, M.; Winey, K. I. *Macromolecules* **2006**, *39*, 5194–5205.
- (187) Patten, T. E.; Xia, J.; Abernathy, T.; Matyjaszewski, K. Polymers with Very Low Polydispersities from Atom Transfer Radical Polymerization. *Science*, 1996, *272*, 866–868.
- (188) Wang, J. S.; Matyjaszewski, K. *Macromolecules* **1995**, *28*, 7901–7910.
- (189) Wang, J. S.; Matyjaszewski, K. *J. Am. Chem.* **1995**, *117*, 5614–5615.
- (190) Matyjaszewski, K.; Xia, J. *Chem. Rev.* **2001**, *101*, 2921–2990.
- (191) Bruggeman, D. A. G. *Ann. Phys.* **1935**, *416*, 969–664.

- (192) Minnich, A.; Chen, G. *Appl. Phys. Lett.* **2007**, *91*.
- (193) Talapin, D. V.; Murray, C. B. *Science* **2005**, *310*, 86–89.
- (194) Sun, S.; Murray, C. B. *J. Appl. Phys.* **1999**, *85*, 4325.
- (195) McDonald, S. A.; Konstantatos, G.; Zhang, S.; Cyr, P. W.; Klem, E. J. D.; Levina, L.; Sargent, E. H. *Nat. Mater.* **2005**, *4*, 138–142.
- (196) Leatherdale, C.; Kagan, C.; Morgan, N.; Empedocles, S.; Kastner, M.; Bawendi, M. *Phys. Rev. B* **2000**, *62*, 2669–2680.
- (197) Gur, I.; Fromer, N. A.; Geier, M. L.; Alivisatos, A. P. *Science* **2005**, *310*, 462–465.
- (198) Ehrler, B.; Walker, B. J.; Böhm, M. L.; Wilson, M. W. B.; Vaynzof, Y.; Friend, R. H.; Greenham, N. C. *Nat. Commun.* **2012**, *3*, 1019.
- (199) Kovalenko, M. V.; Spokoyny, B.; Lee, J.-S.; Scheele, M.; Weber, A.; Perera, S.; Landry, D.; Talapin, D. V. *J. Am. Chem. Soc.* **2010**, *132*, 6686–6695.
- (200) Wang, R. Y.; Feser, J. P.; Lee, J.-S.; Talapin, D. V.; Segalman, R.; Majumdar, A. *Nano Lett.* **2008**, *8*, 2283–2288.
- (201) Ko, D.-K.; Murray, C. B. *ACS Nano* **2011**, *5*, 4810–4817.
- (202) Esfarjani, K.; Chen, G.; Stokes, H. T. *Phys. Rev. B* **2011**, *84*, 085204.
- (203) Minnich, A. J. *Phys. Rev. Lett.* **2012**, *109*, 205901.
- (204) Minnich, A. J.; Johnson, J. A.; Schmidt, A. J.; Esfarjani, K.; Dresselhaus, M. S.; Nelson, K. A.; Chen, G. *Phys. Rev. Lett.* **2011**, *107*, 95901.
- (205) Yang, F.; Dames, C. *Phys. Rev. B* **2013**, *87*, 035437.
- (206) Dames, C.; Chen, G. In *Thermoelectrics Handbook: Macro to Nano*; Rowe, D. M., Ed.; CRC Press, Boca Raton, 2006.

- (207) Koh, Y. K.; Cahill, D. G. *Phys. Rev. B* **2007**, *76*, 075207.
- (208) Siemens, M. E.; Li, Q.; Yang, R.; Nelson, K. a; Anderson, E. H.; Murnane, M. M.; Kapteyn, H. C. *Nat. Mater.* **2010**, *9*, 26–30.
- (209) Johnson, J. A.; Maznev, A. A.; Bulsara, M. T.; Fitzgerald, E. A.; Harman, T. C.; Calawa, S.; Vinels, C. J.; Turner, G.; Nelson, K. A. *J. Appl. Phys.* **2012**, *111*, 023503.
- (210) Inyushkin, A. V.; Taldenkov, A. N.; Gibin, A. M.; Gusev, A. V.; Pohl, H. J. *Phys. Status Solidi C* **2004**, *1*, 2995–2998.
- (211) Regner, K. T.; McGaughey, A. J. H.; Malen, J. A. *Phys. Rev. B* **2014**, *90*, 064302.
- (212) Regner, K. T.; Wei, L. C.; Malen, J. A. *J. Appl. Phys.* **2015**, *118*, 235101.
- (213) Regner, K. T.; Sellan, D. P.; Su, Z.; Amon, C. H.; McGaughey, A. J. H.; Malen, J. a. *Nat. Commun.* **2013**, *4*, 1640.
- (214) Wright, M.; Uddin, a. *Sol. Energy Mater. Sol. Cells* **2012**, *107*, 87–111.
- (215) Becke, A. D. *J. Chem. Phys.* **1993**, *98*, 1372–1377.
- (216) Stephens, P. J.; Devlin, F. J.; Chabalowski, C. F.; Frisch, M. J. *J. Phys. Chem.* **1994**, *98*, 11623–11627.